THESIS FOR THE DEGREE OF DOCTOR OF PHILOSOPHY

Quantum acoustics with superconducting circuits

GUSTAV ANDERSSON

Department of Microtechnology and Nanoscience (MC2)
Division of Quantum Technology
CHALMERS UNIVERSITY OF TECHNOLOGY

Göteborg, Sweden 2020

Cover:
Top: Microscope image of a multimode nonlinear acoustic $QUAKER$ resonator. Inset shows a scanning electron micrograph of the nonlinear Bragg reflector finger structure. Credit: Marco Scigliuzzo.
Bottom: Two-tone spectroscopy measurement of the $QUAKER$ device. Vertical and horizontal lines correspond to resonator modes.

Quantum acoustics with superconducting circuits
GUSTAV ANDERSSON
Department of Microtechnology and Nanoscience (MC2)
Division of Quantum Technology
Chalmers University of Technology

Abstract

The past 20 years has seen rapid developments in circuit quantum electrodynamics, where superconducting qubits and resonators are used to control and study quantum light-matter interaction at a fundamental level. The development of this field is strongly influenced by quantum information science and the prospect of realizing quantum computation, but also opens up opportunities for combinations of different physical systems and research areas. Superconducting circuits in the microwave domain offer a versatile platform for interfacing with other quantum systems thanks to strong nonlinearities and zero-point fluctuations, as well as flexibility in design and fabrication. Hybrid quantum systems based on circuit quantum electrodynamics could enable novel functionalities by exploiting the strengths of the individual components.

This thesis covers experiments coupling superconducting circuits to surface acoustic waves (SAWs), mechanical waves propagating along the surface of a solid. Strong coupling can be engineered using the piezoelectric properties of GaAs substrates, and our experiments exploit this to investigate phenomena in quantum field-matter interaction. A key property of surface acoustic waves is the slow propagation speed, typically five orders of magnitude slower than light in vacuum, and the associated short wavelength. This enables the *giant atom* regime where the artificial atom in the form of a superconducting circuit is large compared to the wavelength of interacting SAW radiation, a condition which is difficult to realize in other systems. Experiments described in this thesis use these properties to demonstrate electromagnetically induced transparency for a mechanical mode, as well as non-Markovian interactions between an artificial giant atom and the SAW field.

When the SAW field is confined to a resonant cavity, the short wavelength allows multimode spectra suitable for interacting with a frequency comb. We use a multimode SAW resonator to characterize the ensemble of microscopic two-level system defects with a two-tone spectroscopy approach. Finally, we introduce a hybrid superconducting-SAW resonator with applications in quantum information processing in mind. Experiments with this device demonstrate entanglement of SAW modes, and show promising results on the way to engineer cluster states for quantum computation in continuous variables.

Keywords: superconducting qubits, circuit QED, hybrid quantum systems, quantum acoustics, surface acoustic wave, SAW, giant atoms, two-level systems, cluster states, two-mode squeezing

Abbreviations

AT	Autler-Townes effect
EIT	Electromagnetically induced transparency
HEMT	High electron mobility transistor
IDT	Interdigital transducer
MBQC	Measurement-based quantum computing
QUAKER	Quantum acoustic Kerr resonator
QED	Quantum electrodynamics
SAW	Surface acoustic wave
SQUID	Superconducting quantum interference device.
STM	Standard tunneling model
TLS	Two-level system
TWPA	Travelling-wave parametric amplifier

List of appended papers

This thesis is based on the work contained in the following appended papers:

Paper A   **Non-exponential decay of a giant artificial atom**
G. Andersson, B. Suri, L. Guo, T. Aref and P. Delsing, *Nature Physics* **15**, 1123-1127 (2019)

Paper B   **Towards on-chip routing of surface acoustic wave phonons**
M. K. Ekström, T. Aref, A. Ask, G. Andersson, B. Suri, H. Sanada, G. Johansson and P. Delsing, *New Journal of Physics* **21** (2019)

Paper C   **Electromagnetically induced acoustic transparency with a superconducting circuit**
G. Andersson, M. K. Ekström and P. Delsing, *Physical Review Letters* **124**, 240402 (2020)

Paper D   **Acoustic spectral hole-burning in a two-level system ensemble**
G. Andersson, A. L. O. Bilobran, M. Scigliuzzo, M. M. de Lima, J. H. Cole and P. Delsing, *submitted manuscript, arXiv:2002.09389* (2020)

Paper E   **Squeezing and correlations of multiple modes in a parametric acoustic cavity**
G. Andersson, S. W. Jolin, M. Scigliuzzo, R. Borgani, M. Tholén, D. B. Haviland and P. Delsing, *submitted manuscript, arXiv:2007.05826* (2020)

Contents

Thesis

1

Introduction

The first computers were mechanical devices. The abacus, a precursor to computing technology, predates the use of electricity by many centuries. While this may not imply that the first practical *quantum* computers should also be mechanical, engineering quantum states of the mechanical degree of freedom may prove useful to quantum information applications.

Over the last two decades, circuit quantum electrodynamics (circuit QED) [1, 2] has emerged as one of the most promising routes towards realising practical quantum computation. Circuit QED is based on the controlled interaction between superconducting qubits and resonators operating at microwave frequencies. This field allows studying light-matter interaction at the quantum level, and scaling circuit QED systems is one of the leading approaches to quantum information processing [3]. The versatility of microwave circuits enables engineering hybrid quantum systems, where superconducting circuits interact strongly with quantum systems of a different type, including mechanical degrees of freedom. In this thesis, we investigate how surface acoustic wave (SAW) fields can be coupled to superconducting microwave circuits in hybrid quantum acoustic systems.

In this introductory chapter, we start by outlining some basics of surface acoustic waves, and attempt to provide a bit of context for the work presented in subsequent chapters. We then introduce aspects of superconductivity that are integral to the devices designed for the experiments presented in this thesis. Finally we briefly explain some of the experimental methods involved, including sample fabrication methods.

In Chapter 2, we tackle the theoretical problem of SAW-qubit interaction, providing the theoretical foundation for the results of Papers A-C. These experiments are based the interaction of transmon qubits with SAW transmission lines, and are presented in Chapter 3. Papers D and E present experiments with SAW fields confined to resonant cavities. In Chapter 4 we discuss the probing of microscopic two-level system defects

using the standing-wave modes of a SAW cavity. Finally, in chapter 5 we attempt to develop the SAW-resonator towards quantum computing applications by coupling to a nonlinear microwave circuit.

1.1   Surface acoustic waves

Surface acoustic waves are mechanical waves that travel along the surface of solids, and were first described theoretically in 1885 by Lord Rayleigh [4]. SAW occur naturally as they are generated by earthquakes, but also have a range of technological applications, mainly in signal processing electronics for telecommunication.

The development of SAW-based electronic devices took off in the 1960's with the introduction of the interdigital transducer (IDT) fabricated on piezoelectric substrates [5], which enabled efficient generation and detection of SAW in a compact geometry. SAW devices with IDTs and reflective gratings could be efficiently produced using photolithography and were developed as delay lines and filters for radar applications. Later, with the rapid development of mobile communication technologies SAW filters have found extensive use in particular in mobile phones. Today, the annual production figures number in the billions. A key aspect enabling SAW-based technology is the slow velocity of sound compared to electromagnetic signals. Compared to light, SAW beams propagate five orders of magnitude slower, and therefore have the same reduction in wavelength at a given oscillation frequency. This enables resonant structures to be engineered with a much smaller on-chip footprint, a major advantage in modern integrated circuit design.

SAWs can be effectively interfaced with electric circuits because of the piezoelectric effect. The asymmetric configuration of electric dipoles in piezoelectric crystals gives rise to a net polarization when the material is strained. Conversely, a voltage applied across a piezoelectric material will induce a mechanical deformation. This effect is present for any insulating material whose crystal structure breaks inversion symmetry. On piezoelectric substrates, SAW waves therefore give rise to oscillating electric fields as well as strain fields. A spatially-periodic electrode structure can emit SAW if an oscillating voltage is applied such that the period matches the SAW wavelength at the oscillation frequency. In a piezoelectric material, the mechanical stress tensor $\mathbf{T}$ couples not just to the strain $\mathbf{S}$ via Hooke's law, but also the electric field $\vec{E}$ via [6]

$$\mathbf{T} = \mathbf{c}\mathbf{S} - \mathbf{e}\vec{E}, \tag{1.1}$$

where $\mathbf{c}$ is the elastic stiffness tensor and $\mathbf{e}$ the *piezoelectric tensor*. The constitutive relation for the electric displacement field $\vec{D}$ is likewise modified from the non-piezoelectric case and reads

$$\vec{D} = \mathbf{c}\mathbf{S} + \varepsilon\vec{E} \tag{1.2}$$

where ε is the electric permittivity (assumed to be isotropic). For symmetry reasons, many elements of $\mathbf{c}$ and $\mathbf{e}$ turn out to be zero for most solids, and non-zero elements are determined by a small number of independent parameters. SAWs result from solutions to the elastic wave equation for the displacement $\vec{u}$

$$\nabla \cdot \mathbf{T} = \rho \frac{\partial^2 \vec{u}}{\partial t^2} \tag{1.3}$$
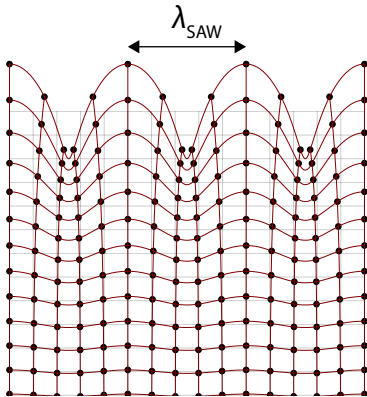
Figure 1.1: Illustration of a Rayleigh wave in the plane of propagation. The Rayleigh mode is a superposition of longitudinal and transversal modes, leading to elliptical particle trajectories with a vertical major axis. The amplitude of the excitation decays exponentially into the bulk of the material with a depth approximately corresponding to the wavelength λ_{SAW}. The displacements have been greatly exaggerated for illustration.

that satisfy Eqs. (1.1-1.2), where the displacement field $\vec{u}$ related to the strain by

$$S_{ij} = \frac{\partial u_i}{\partial x_j}. \tag{1.4}$$

SAW modes are solutions to Eqs. (1.1-1.3) in the piezoelectric half-space that decay into the bulk ($\vec{u}$ tends to zero as $z \to 0$) and satisfy the stress-free boundary condition at $z = 0$

$$T_{iz} = 0. \tag{1.5}$$

The SAW excitations coupling to superconducting circuits in the work presented in this thesis are Rayleigh modes [4], a combination of longitudinal and transverse acoustic modes leading to elliptical motion of particles in planes normal to the surface and parallel to the propagation direction. An important quantity for this interaction is the SAW electric potential ϕ, given by $\vec{E} = -\nabla \phi$, which can induce potential differences across circuit electrodes. The Rayleigh SAW mode is illustrated in Fig. 1.1. For derivation and further discussion of the Rayleigh mode solution, see for instance [7, 8, 9].

In addition to radio frequency electronic devices, SAW-based devices are increasingly used as sensors for gasses [10] and in liquid environments [11]. Another emerging application is in the microfluidic systems used in life science, where SAWs provide a way of transporting and mixing liquids in a controlled way [12]. As lab-on-a-chip systems grow increasingly complex, SAW-based acoustofluidics promises to add important capabilities to manipulate and analyse biological objects with integrated circuits [13].

In device-oriented solid state physics research, SAWs can be interfaced with a wide range of elementary excitations. This can be exploited to probe condensed-matter systems with sound, but also to provide additional means of controlling excitations for device

applications. The coupling of SAW with graphene and other 2D materials provide a means of controlling their electronic properties [14, 15] and can be used to generate acousto-electric currents as well as enhanced optical coupling to graphene plasmon excitations [16]. Magnetoelastic coupling allow surface acoustic waves to drive magnetic resonances in ferromagnetic films [17]. This effect is exploited in the emerging field of straintronics, where SAW-driven switching could be integrated in magnetic memory systems [18].

Of high relevance to the work presented in this thesis is the ability of SAW to couple with and control individual quantum systems. The SAW electric potential can interact with a two-dimensional electron gas in semiconductor heterostructures [19, 20]. Together with electrostatically defined quantum dot structures [21], this allows for the transport of single electrons confined to a SAW potential minimum, effectively creating moving quantum dots. This mechanism can be used in optoelectronics to engineer single photon sources [22], for spin transport and manipulation [23], as well as the developing field of electron quantum optics. Here, quantum optical experiments are performed with SAW-propagated single electrons [24] with the aim of realising quantum coherent effects, including proposed schemes for quantum computing [25]. Standing wave SAW potentials interfaced with a two-dimensional electron gas also have the potential to generate artificial lattices for solid-state based quantum simulation [26]. SAW can also be interfaced with optically active quantum dots [27, 28] and have been used to drive phonon-assisted Rabi oscillations in NV-centres in diamond [29] as well as Rabi oscillations in a single defect spin in SiC [30]. The versatility of SAW devices in the engineering of both confined and propagating fields and the wide range of quantum systems that can be interfaced make SAW a good platform for coupling disparate quantum systems [31]. This naturally includes superconducting quantum circuits, and could provide an important coupling element to future hybrid quantum information systems.

1.2   Quantum acoustics with superconducting circuits

Whereas SAWs can be used to probe and control a wide range of quantum systems, the coupling to superconducting circuits enables remarkable possibilities of engineering non-classical states of the SAW field itself. The comparatively large size of superconducting circuits and the ability to engineer the overlap between microwave and mechanical modes allows hybrid superconducting acoustic systems to achieve interaction strengths that exceed dissipation rates at the single excitation level, the so-called *strong coupling* regime. An important development in this direction was the cooling to the motional ground state and qubit control of a piezoelectric cantilever oscillator in 2010 [32]. Rapid development since then has seen superconducting qubits used to create non-classical phonon states in bulk acoustic resonators [33, 34] and resolve the phonon number of acoustic excitations [35]. Acoustic resonators are compact and can be designed to support multiple modes, which could enable integration in superconducting quantum processors as memories [36]. Another important prospective application for quantum acoustics is in the conversion of quantum information between the microwave and optical frequency domains, the main objective of research in optomechanics [37]. The coupling of an acoustic device with both superconducting circuits and laser light could enable communication

of quantum information between distant superconductor-based quantum processors via optical fibers. This idea is being pursued using a variety of configurations including SAW-based architectures [38, 39].

Surface acoustic waves were probed with a single-electron transistor in 2012 [40] and then made to interact with a superconducting qubit for the first time in 2014 [41]. In this experiment, propagating SAW beams were scattered and emitted by a transmon qubit fabricated on gallium arsenide. In contrast to most implementations of quantum acoustics with superconducting circuits, SAWs enable the coupling of artificial atoms to propagating modes, an acoustic analogue of what in the microwave domain is referred to as waveguide QED [42, 43]. The slow propagation velocity and associated short wavelength of sound enable exploring new parameter regimes of quantum optics, or rather quantum atom-field interaction, where the quantum emitter is large compared to the wavelength of coupled radiation. Some progress in this direction is presented in this thesis, including non-Markovian giant atoms (Paper A) and electromagnetically induced acoustic transparency (Paper C).

SAW resonators have been operated in the quantum regime [44] and coupled to superconducting qubits [45, 46]. As for propagating SAW, this has led to investigations of new parameter regimes [47, 48] not easily realized in quantum optical systems. Similarly to bulk acoustic systems, the controlled generation of non-classical phonon states has been implemented with SAW [49], and quantum state transfer has been demonstrated using a SAW resonator as an effective delay line. These experiments demonstrate the viability of using SAW to encode and transmit quantum information.

1.3 Superconductivity and the Josephson effect

Superconductivity, discovered in 1911 by Kamerlingh Onnes [50], is characterized by vanishing electrical resistance below a certain critical temperature T_c. The circuits discussed in this thesis are measured in the superconducting state of aluminium, and the absence of normal-metal resistive loss is essential to their operation. We also make use of the special properties of supercurrent tunnelling in device engineering.

In the superconducting state, electrons form pairs due to the phonon-mediated electron-electron interaction [51], and condense into a collective ground state [52]. The energy required to break one of these so-called Cooper pairs is twice the superconducting gap Δ_s, and the vanishing density of states inside the gap prevents electrons from the scattering processes that induce resistance. The collective many-particle state of the Cooper pair condesate can be described by a macroscopic wavefunction $\Psi = \sqrt{n_p}e^{i\theta}$ [53]. The superconducting phase θ plays an important role in the tunneling of Cooper pairs across *Josephson junctions*, nonlinear circuit elements that form an important building block in superconducting quantum circuits.

1.3.1 Josephson junctions

A key element to superconducting quantum circuits is the Josephson junction. It consists of two superconducting electrodes separated by a thin ($\sim 2\,\mathrm{nm}$) tunnel barrier. The tunnel

current across the junction depends on the relative superconducting phase $\varphi = \theta_1 - \theta_2$ of the two electrodes

$$I = I_c \sin \varphi. \tag{1.6}$$

The critical current I_c is the maximal supercurrent the junction can sustain and is determined by the tunnel coupling across the barrier. If a voltage is applied across the junction, the phase difference evolves according to

$$\frac{d\varphi}{dt} = \frac{2eV}{\hbar}. \tag{1.7}$$

These relations were predicted theoretically by Josephson [54] in 1962. From the Josephson relation we get the time derivative of the current as

$$\frac{dI}{dt} = I_c \cos \varphi \frac{2eV}{\hbar}. \tag{1.8}$$

The Josephson junction has the current-voltage characteristic of an inductor, and rearranging Eq. (1.8) we get

$$V = \frac{\Phi_0}{2\pi I_c \cos \varphi} \frac{dI}{dt} = \frac{L_J}{\cos \varphi} \frac{dI}{dt} \tag{1.9}$$

where we have introduced the *magnetic flux quantum* $\Phi_0 = h/(2e)$. The junction is characterized by the Josephson inductance $L_J = \Phi_0/(2\pi I_c)$, inversely proportional to the critical current. Like classical inductors can store energy in magnetic fields, energy can be stored in the Josephson junction. This energy is given by integrating the electric power to obtain the total work done on the junction as [55]

$$E = \int_0^t IV dt = \int_0^t I_c \sin \varphi \frac{\Phi_0}{2\pi} \frac{d\varphi}{dt} dt. \tag{1.10}$$

where we have inserted the relations (1.6-1.7). Changing the integration variable to φ and taking $\varphi(t = 0) = 0$, this can be written as

$$E = \frac{\Phi_0 I_c}{2\pi} \int_0^\varphi \sin \varphi d\varphi = \frac{\Phi_0 I_c}{2\pi} \left(1 - \cos \varphi\right) = E_J \left(1 - \cos \varphi\right) \tag{1.11}$$

The parameter $E_J = \Phi_0 I_c/(2\pi)$ is the characteristic energy of the junction and sets an important energy scale for the design of superconducting devices. To enable flux tuning of the Josephson energy, junctions are often integrated into devices in the form of a superconducting quantum interference device (SQUID). The SQUID consists of two junctions in parallel, effectively forming a loop. It can be shown that the critical current of the SQUID depends on the external flux threading the loop as

$$I_{c,SQ} = 2I_c \left| \cos \frac{\Phi}{\pi \Phi_0} \right| \tag{1.12}$$

where we have assumed that the two junctions are identical with critical current I_c. A magnetic flux generated by an external coil or an on-chip flux line can then be used to tune the SQUID critical current. As SAWs generally can only be excited over relatively narrow bandwidths in a given device, the ability to tune circuit parameters *in situ* greatly facilitates engineering the interaction. In addition, the SQUID enables parametric driving, where the junction inductance is modulated at microwave frequencies

1.4   Experimental methods

1.4.1   Sample fabrication

All results in this thesis were measured with devices fabricated in the Chalmers nanofabrication laboratory on gallium arsenide substrates. The IDT structures are defined by electron-beam lithography. To start the fabrication process, a clean wafer is spin-coated with two layers of resist, a polymer sensitive to electron irradiation. The desired pattern is then exposed to an electron beam. After exposure, development chemicals are used to selectively remove the resist layers in the exposed areas, where polymer chains have been disrupted by the electron irradiation. The higher sensitivity of the bottom resist layer ensures the formation of an undercut. Subsequently, an aluminium layer is deposited using an electron-beam evaporator. To minimize the mass load on the SAW which may induce unwanted scattering, the Al layer is only about $\sim 30\,\mathrm{nm}$ thick. The undercut is necessary to get a clean metal film not sticking to the resist sidewalls, but if it gets too large the IDT finger array structures cannot be resolved. The samples used for Papers A-D use a minimal finger separation of $150\,\mathrm{nm}$. An improved fabrication recipe allowed the samples measured for Paper E to use a $90\,\mathrm{nm}$ feature size. After deposition the resist is removed, leaving the wafer with the desired Al pattern.

The Josephson junctions consist of overlapping aluminium electrodes separated by an aluminium oxide tunnel barrier. They are likewise fabricated using e-beam lithography, but require two metal deposition steps from different angles with oxidation in between. By choosing the angle of deposition, the resist pattern is projected onto slightly different positions on the substrate. In the Dolan technique [56], also known as shadow evaporation, alternating between a positive and a negative angle creates an overlap between the junction electrodes. This method is used for the junctions in Papers A-C, and requires a suspended bridge in the resist to create the "shadow". In paper E, we adopt the *Manhattan* fabrication method, which involves a 90° rotation around the normal axis of the substrate between deposition steps. This method does away with the suspended bridge, improving robustness of the process, but requires an additional lithography step [57].

Remaining metal structures besides IDTs and junctions are fabricated using a direct-write maskless optical lithography process. The recipes for the fabrication steps are provided in Appendix B.

1.4.2   Measurement techniques

To be useful for quantum physics experiments, superconducting circuits operating at GHz frequencies need to be cooled down to their quantum ground state, requiring temperatures of the order $\sim 10\,\mathrm{mK}$. While this may sound like a terminal drawback, commercially available *dilution refrigerators* reach this temperature with highly automated operation. The cooling power at the base temperature stage of a dilution refrigerator is generated by the enthalpy of mixing the ^{4}He and ^{3}He isotopes of helium. Below temperatures of around $0.8\,\mathrm{K}$ the He mixture separates into two phases with different concentrations of ^{3}He. Heat is required to move ^{3}He from the concentrated phase (almost pure ^{3}He) to the dilute phase

(6.4 % ^{3}He), and in the refrigerator this heat is removed from the experimental space, cooling it below 10 mK. Modern dilution refrigerator such as the Bluefors system used for the experiments presented in this thesis have a pulse-tube cryocooler for pre-cooling the system to 4 K where the dilution cycle can be started. Traditionally this was accomplished with a liquid helium bath. With a cryocooler, the system is closed and "dry", in the sense that user does not need to handle any cryoliquids. For a detailed description of the dilution refrigerator working principle and technology, see the reference [58].

The experimental wiring consists of coaxial cables that are attenuated for input lines, and amplified with cryogenic HEMT amplifiers for the device output signals. To prevent thermal noise from reaching the device through the output line, the sample is connected to the amplifiers via microwave circulators or isolators. Isolators are non-reciprocal two-port microwave components based on ferromagnets that only allow forward-propagation of the signal. Circulators are three-port devices that work similarly and allow reflection measurement setups. The dimensions of circulators and isolators are set by the wavelength of the microwave fields in the frequency range of operation, and become bulky at low frequencies. As lower frequencies relax the demands on lithographic precision in SAW device fabrication, the experiments of Papers A-D are performed with circulators in the 2.15 GHz-2.65 GHz range. The device designed for the experiments reported in Paper D operate slightly below 4 GHz and are compatible with isolators with a 4 GHz nominal cutoff frequency. This measurement also makes use of a travelling-wave parametric amplifier (TWPA) [59] supplied by Lincoln Labs. the TWPA provides amplification near the quantum limit of added noise across a bandwidth ranging from below 4 GHz to above 8 GHz. This makes the setup slightly more complex, as operating the TWPA requires a strong pump signal via a separate input line. A schematic of the cryostat wiring diagram for this setup is shown in Fig. 1.3.
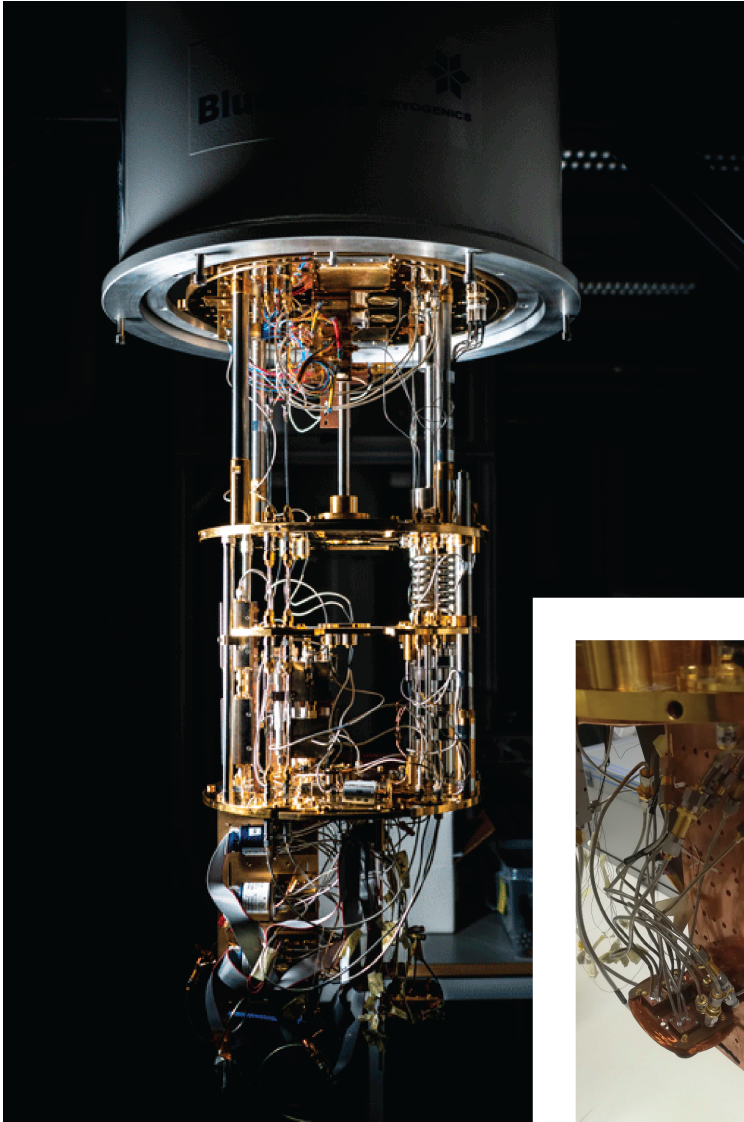
Figure 1.2: The dilution refrigerator *Wampa* where the experiments presented in this thesis were performed. Photo: WACQT. Inset shows sample boxes installed with a superconducting coil used to apply an external magnetic flux.
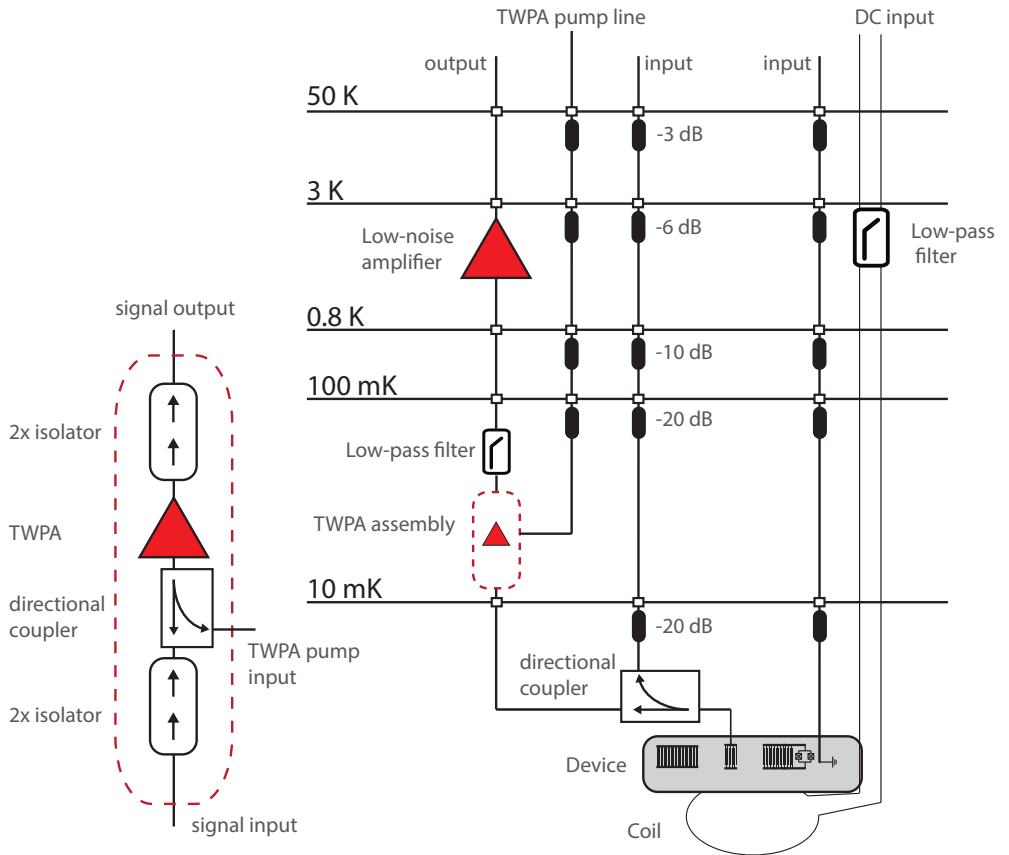
Figure 1.3: Wiring diagram for the dilution refrigerator. The QUAKER device, discussed in Ch. 5, has two coaxial cable input lines. In addition, there is an external coil with a filtered DC line. The output line is amplified with a travelling-wave parametric amplifier (TWPA). The left inset shows the TWPA assembly.

2

Coupling a superconducting qubit to surface acoustic waves

In this chapter we introduce the transmon, the type of superconducting qubit used in the experiments presented in this thesis, as well as the transducer design used to engineer the SAW-qubit coupling. We then derive expressions for the coupling strength using a semiclassical circuit model approach as well as using a quantum mechanical treatment.

2.1   The transmon qubit

Introduced in 2007 [60], the transmon is the most widely used superconducting qubit [61] and most efforts to develop superconducting quantum processors rely on this type of circuit. The transmon is an LC resonant circuit consisting of a Josephson junction or SQUID acting as an inductive element shunted by a capacitance. The Hamiltonian of the transmon is obtained by adding the charging energy of the capacitance and the Josephson energy of the junctions, giving

$$\hat{H} = 4E_C(\hat{n} - n_g)^2 - E_J \cos\hat{\varphi}. \tag{2.1}$$

The energy scale $E_C = e^2/(2C)$ where C is the total transmon capacitance, is equal to the electrostatic energy of adding one excess electron to the transmon. In addition to the shunt capacitance C_t, the transmon is connected to an external circuit for control and read-out via the gate capacitance C_g. The classical variable n_g is the offset charge due to the gate voltage $n_g = C_g V_g/(2C)$. The characteristic energy of the junction is set by the Josephson energy $E_J = \Phi_0 I_c/(2\pi)$ derived in Eq. (1.11). The number of Cooper pairs on
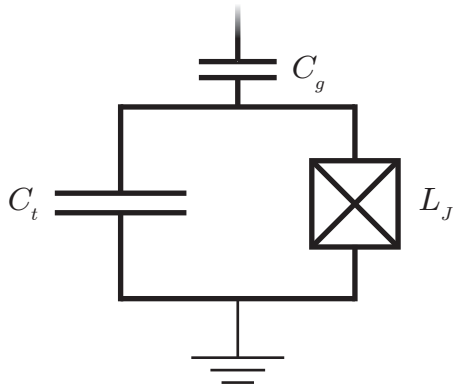
Figure 2.1: Transmon circuit diagram. The crossed square represents the Josephson junction, which may be split into two parallel junctions to form a SQUID. Such configurations allow for tuning the transmon frequency by applying a magnetic flux. The total capacitance is $C = C_t + C_g + C_J$, where C_J is the typically negligible capacitance of the junction electrodes.

the transmon $\hat{n}$ and the phase across the junction $\hat{\varphi}$ obey the commutation relation

$$[\hat{n}, \hat{\varphi}] = -i. \tag{2.2}$$

This allows for defining the associated creation and annihilation operators $\hat{a}^\dagger$, $\hat{a}$ via [62, 63]

$$\hat{\hat{\varphi}} = \left(\frac{2E_C}{E_J}\right)^{1/4} \left(\hat{a} + \hat{a}^\dagger\right), \tag{2.3}$$

$$\hat{n} = -i\left(\frac{E_J}{32E_C}\right)^{1/4} \left(\hat{a} - \hat{a}^\dagger\right). \tag{2.4}$$

The transmon is designed to operate in the regime where $E_J \gg E_C$. In this case the charge dispersion, the dependence of the resonance frequency on the gate charge n_g, is strongly suppressed, reducing the sensitivity to charge noise. The transmon Hamiltonian is similar to that of a quantum harmonic oscillator, with the parabolic potential replaced by a cosine term. This modifies the harmonic, equidistant energy spectrum into a slightly anharmonic one. Expanding up to fourth order in $\hat{\varphi}$ this gives

$$E_J \left(1 - \cos\hat{\varphi}\right) = \frac{1}{2!}E_J\hat{\varphi}^2 - \frac{1}{4!}E_J\hat{\varphi}^4 + ... \tag{2.5}$$

The leading term in eq (2.5) corresponds to the harmonic oscillator. The quartic term contributes a negative anharmonicity $\alpha = \omega_{12} - \omega_{01}$, where ω_{ij} is the transition frequency between states i and j. In terms of the ladder operators the Hamiltonian can be written as

$$\hat{H} = \hbar\omega_{01}\hat{a}^\dagger\hat{a} + \hbar\frac{\alpha}{2}\hat{a}^\dagger\hat{a}^\dagger\hat{a}\hat{a}. \tag{2.6}$$

The transmon anharmonicity is $\alpha = -E_C$, which diminishes as more capacitance is added. The trade-off between suppressing charge dispersion and maintaining sufficient anharmonicity is greatly aided by the fortunate circumstance that the dispersion is exponentially suppressed as the E_c/E_J ratio is reduced, while the anharmonicity decreases only algebraically. This different behaviour is a key reason for the widespread adoption of the transmon for superconducting qubit experiments. To operate the transmon as a qubit, we identify the ground and first excited states as the logical states $|0\rangle$ and $|1\rangle$, respectively and write the Hamiltonian conveniently as

$$\hat{H} = \hbar \frac{\omega_{01}}{2} \hat{\sigma}_z. \tag{2.7}$$

The form Eq. (2.7) assumes a quasi two-level system, i.e. that the anharmonicity is sufficient to prevent signals resonant with ω_{01} from exciting higher transitions, and that these transitions are not addressed in the system under consideration.

2.2 The interaction of a qubit with a propagating SAW field

To describe the coupling of a qubit to SAW we shall first introduce the basic theory of the interdigital transducer (IDT), and then develop a semiclassical circuit model integrating this component with the transmon described above. We will also consider a quantum mechanical model of this interaction for the simplified case of pointlike transducer fingers.

2.2.1 Interdigital transducers

The conversion of signals between electromagnetic and surface acoustic wave excitations is based on the piezoelectric effect, and the circuit element we use for this purpose is the interdigital transducer. The IDT consists of a periodic array of finger electrodes, alternately connected to a top and bottom bus bar electrode. Effective transduction occurs when the period of the IDT matches the SAW wavelength, giving rise to a strong frequency dependence in the conversion efficiency between electromagnetic signals and SAW. Assuming linear response, the IDT is characterized by the transmitter and receiver response functions μ and g_m [6]. The electric potential ϕ_{out} of a SAW wave emitted from the the IDT is given by $\phi_{\text{out}} = \mu V_t$, where V_t is the voltage applied across the transducer. The receiver response function g relates the current generated in the IDT circuit to the amplitude of an incoming SAW wave, $I = g_m \phi_{\text{in}}$. It is natural to consider a transmission line model for the SAW with a characteristic impedance Z_0. When interfacing SAW with electrical circuits we are mainly interested in the electric potential ϕ, and define the characteristic impedance in terms of ϕ and the total power P_{SAW}, giving $Z_0 = |\phi|^2/(2P_{\text{SAW}})$. For the IDT response functions, it holds that $g_m = 2\mu/Z_0$. To quantitatively describe the behaviour of the IDT and SAW transmission line, it is necessary to consider the material properties of the substrate on which the surface acoustic waves propagate. The strength of the piezoelectric interaction is characterized by the electromechanical coupling coefficient K^2. The piezoelectricity gives rise to an effective
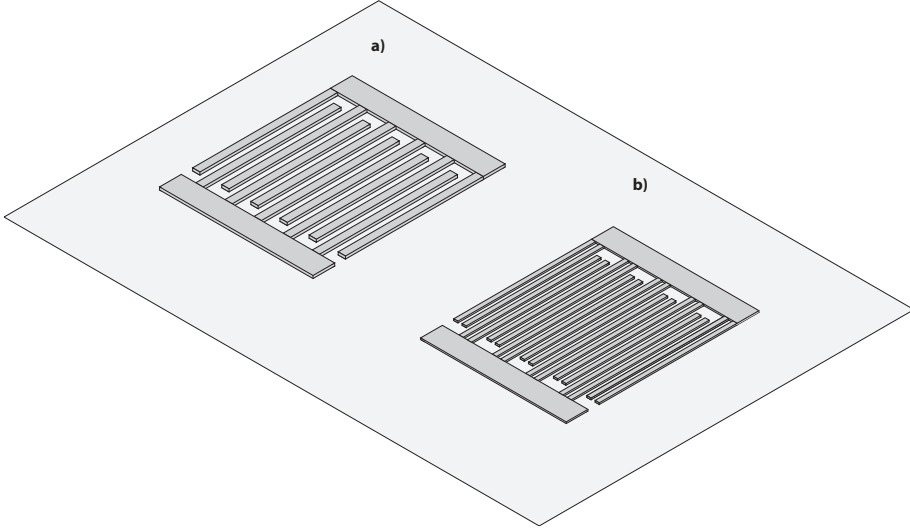
Figure 2.2: IDT designs. The simplest configuration **a)** typically gives rise to a distorted response due to internal mechanical reflections. The layout **b)** where each finger is split into two is used to suppress such reflections, but requires a finer finger pitch.

additional stiffness in the material, as the electric fields induced counteract the material strain. A conducting film covering the substrate screens the electric field, reducing this effect and thereby also reducing the SAW velocity. The coefficient K^2 can be expressed in terms of the relative magnitude of this velocity change. If SAW propagate on a free surface with velocity v_{SAW} and $\Delta v = v_{\text{SAW}} - v_m$ is the difference in velocity compared to a substrate covered with a metallic film, it is given by

$$K^2 = 2\frac{\Delta v}{v_{\text{SAW}}}. \tag{2.8}$$

The other important material parameter is the effective permittivity C_S. This is the capacitance per unit length of overlap between two fingers assuming a 50 % metallization ratio, meaning the gap is equal to the individual finger width. The characteristic impedance is now given by

$$Z_0 = \frac{K^2}{\omega_{\text{IDT}}WC_s}, \tag{2.9}$$

where W denotes the finger overlap. The frequency ω_{IDT} is defined by the condition of constructive interference of SAW emitted from all finger pairs, given by $\omega_{\text{IDT}}/2\pi = 2p/v_{\text{SAW}}$ for a transducer period of $2p$. The transmitter response function of a single IDT finger pair for the 50 % metallization case is

$$\mu_e = 1.6iK^2. \tag{2.10}$$

This *element factor* is calculated considering the charge distribution arising from biasing one finger while the others are grounded. To obtain the IDT response μ, we have to

consider the superposition of contributions from each electrode in the structure. In general, as well as for the simplest IDT design illustrated in Fig. 2.2a, internal reflections in the IDT imply the response can only be calculated numerically. If such reflections are neglected, μ may be calculated by multiplying μ_e with the *array factor* A obtained from summing over the polarity P_n and phase of all the N electrodes in the transducer, giving

$$A = \sum_{n}^{N} P_n \exp ikx_n. \tag{2.11}$$

The array factor then is the Fourier transform of the real space configuration of electrodes, which allows for tailoring the frequency response by changing the transducer layout. For a regular transducer, Eq. (2.11) is a geometric sum and can be calculated as

$$A = \sum_{n=1}^{N_p} \exp\left(2\pi in\frac{\omega}{\omega_{\mathrm{IDT}}}\right) \approx N_p\frac{\sin X}{X} \tag{2.12}$$

where N_p is the number of periods in the IDT structure and $X = N_p\pi\left(\omega - \omega_{\mathrm{IDT}}\right)/\omega_{\mathrm{IDT}}$. Here we have made the small-angle approximation $\sin\left(\omega - \omega_{\mathrm{IDT}}\right)/\omega_{\mathrm{IDT}} \approx \left(\omega - \omega_{\mathrm{IDT}}\right)/\omega_{\mathrm{IDT}}$, valid close to the IDT centre frequency ω_{IDT}. The array factor gives a sinc-like frequency dependence to the IDT response which for a non-reflective transducer with finger pitch p is centred around $\omega_{\mathrm{IDT}}/2\pi = 2p/v_{\mathrm{SAW}}$. The SAW velocity is typically around $v_{\mathrm{SAW}} \approx 3000\,\mathrm{m/s}$, resulting in wavelengths of the order $\lambda_{\mathrm{SAW}} = 2p \approx 1\,\mathrm{\mu m}$ for devices in the GHz frequency range.

To suppress internal reflections, we adopt a double-finger design shown in Fig. 2.2b, where each finger is replaced by two, separated by $p/4$. The suppression arises from destructive interference of reflections from each of the split fingers. In this configuration, μ_e, C_s and the array factor are modified and given by

$$\mu_{e,df} = 1.2iK^2 \tag{2.13}$$
$$C_{s,df} = \sqrt{2}C_{s,sf} \tag{2.14}$$
$$A_{df} = \sqrt{2}A_{sf} \tag{2.15}$$

where the subscript df (sf) indicates the double (single) finger case. With the approximation $\mu_{e,df} \approx \mu_{e,sf}/\sqrt{2}$, we get the transmitter response function valid for both single and double finger transducers

$$\mu = 0.8iK^2N_p\frac{\sin X}{X}. \tag{2.16}$$

For the purpose of device design it is useful to describe the IDT with a circuit model. The effect of SAW transduction contributes a complex admittance $Y_a = G_a + iB_a$ to the IDT circuit. The acoustic conductance G_a represents conversion of electrical current to SAW and is proportional to the squared magnitude of the transmitter response

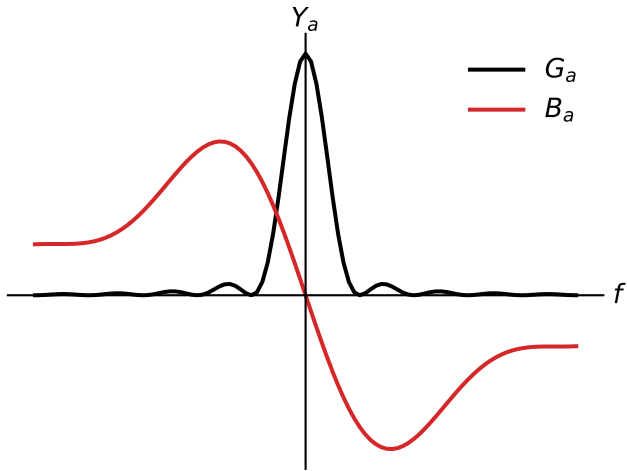$$G_a = \frac{2\left|\mu\right|^2}{Z_0}. \tag{2.17}$$

Figure 2.3: Real (G_a) and imaginary (B_a) parts of the acoustic admittance Y_a as a function of frequency. On acoustic resonance $\omega = \omega_{\mathrm{IDT}}$, G_a is maximal and $B_a = 0$. At frequencies above (below) the IDT centre frequency, B_a contributes a negative (positive) susceptance, providing a capacitance-like (inductance-like) impedance to the IDT circuit.

The imaginary impedance B_a is related to G_a via the Hilbert transform due to causality [64]. Using the result of Eq (2.16), the acoustic impedance can be written as

$$G_a = G_{a,0} \left(\frac{\sin X}{X} \right)^2, \tag{2.18}$$

$$B_a = G_{a,0} \frac{\sin (2X) - 2X}{2X^2}, \tag{2.19}$$

where the conductance on IDT resonance $X = 0$ is

$$G_{a,0} \approx 1.3 K^2 N_p^2 \omega_{\mathrm{IDT}} W C_s. \tag{2.20}$$

The frequency dependence of G_a and B_a are shown in Fig. 2.3. Together with the capacitance C_t due to the IDT fingers, G_a and B_a form the circuit of Fig. 2.4a. In principle, maximal acoustic conversion occurs when the imaginary impedance B_a balances the IDT capacitance $iB_a + 1/(i\omega C_t) = 0$. To achieve efficient conversion between electrical and acoustic signals in practice, the impedance matching to the connected electrical transmission line has to be taken into account.

2.2.2 Semiclassical circuit model for SAW-qubit coupling

The SAW-coupled transmon consists of an IDT shunted to ground by a SQUID. This gives the circuit diagram shown in the circuit Fig. 2.4b. The capacitance of the IDT
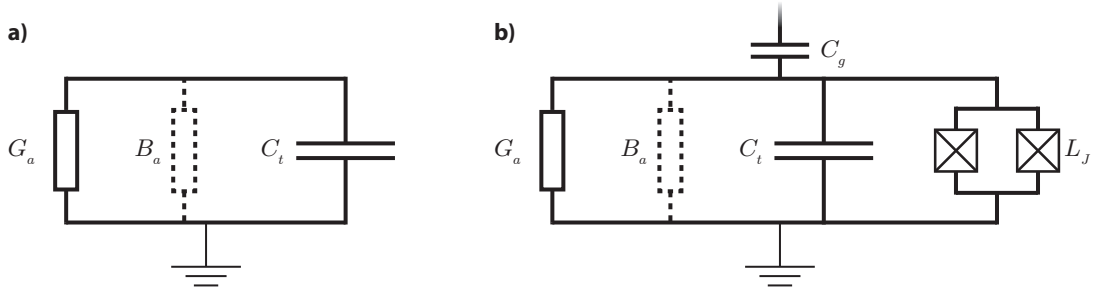
Figure 2.4: Transducer circuit diagrams. **a)** Circuit diagram for an IDT consisting of the acoustic admittance elements in parallel with the capacitance C_t of the finger structure. **b)** A SAW-coupled transmon qubit circuit diagram. The two junctions forming a SQUID enables tuning of the transmon resonance frequency ω_{01} by an external magnetic flux. As it may be difficult to align the qubit frequency with the IDT centre frequency using fixed fabrication parameters, flux tuning is essential to obtaining qubit-IDT resonance $\omega_{01} \approx \omega_{\text{IDT}}$. Whereas the IDT in **a)** is generally directly connected to an electrical transmission line, qubit excitations are controlled via the gate capacitance C_g.

acts as the shunt capacitance of the transmon, as shown in the schematic illustration of Fig. 2.5. To extend the IDT circuit model to represent the transmon, we add a tunable inductance L_J in parallel with the acoustic admittance and IDT capacitance. Neglecting other losses, the relaxation rate of the qubit by emitting SAW is given by the dissipation due to G_a, and can be written as

$$\Gamma_a = \frac{\omega_{\text{IDT}} G_a}{2} \sqrt{\frac{L_J}{C_t}} = \frac{G_a}{2C_t} \tag{2.21}$$

With our expression for G_a this yields

$$\Gamma_a = \Gamma_{a0} \left(\frac{\sin X}{X} \right)^2, \tag{2.22}$$

where $\Gamma_{a0} \approx 0.5 K^2 N_p \omega_{\text{IDT}}$ is the on-resonance decay rate. This semiclassical picture does not account for the discrete nature of qubit excitations, but remains valid for the case when the transmon is not excited above the $|1\rangle$ level.

It is interesting to note that the tunable inductance of the SQUID facilitates impedance matching. Consider the acoustic reflection of a SAW wave incident on the SAW-coupled transmon. The *S-parameter* S_{11} [65], defined as the ratio of incoming to reflected voltage amplitudes $\phi_{\text{out}}/\phi_{\text{in}}$, can be calculated using the relations $\phi_{\text{out}} = \mu V_t$, $I = g_m \phi_{\text{in}}$, giving [66]

$$S_{11} = \frac{\phi_{\text{out}}}{\phi_{\text{in}}} = -\frac{\mu g_m V_t}{I}. \tag{2.23}$$

The minus sign arises from the phase shift of the reflected signal. The current I is related
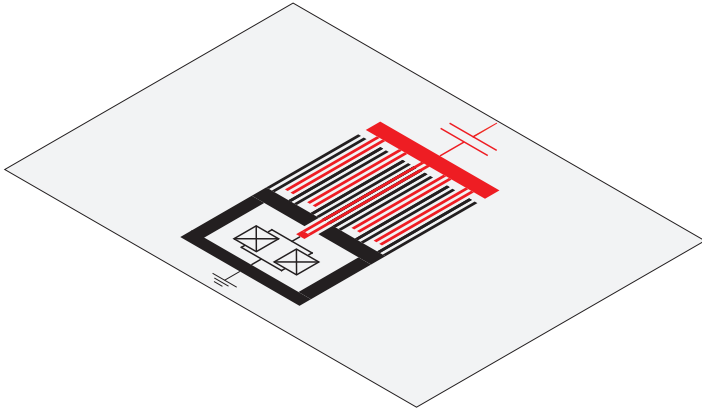
Figure 2.5: SAW-coupled transmon qubit. The bottom electrode (black) is grounded and shunted to the top electrode (red) via a SQUID. The interdigitated finger structure provides the shunt capacitance of the transmon as well as coupling to SAW. An external magnetic flux threading the SQUID loop can be used to tune the transmon resonance frequency. The top electrode is capacitively coupled to an external circuit for control and readout.

to V_t by the impedance $Y_{\text{tot}} = Y_a + i\omega C + 1/(i\omega L_J)$, which yields

$$S_{11} = \frac{G_a}{G_a + iB_a + i\omega C + 1/(i\omega L_J)}. \tag{2.24}$$

where we have used that $G_a = -\mu g_m$. We observe that when the (tunable) inductance L_J balances out B_a and the capacitve impedance such that $iB_a + i\omega C + 1/(i\omega L_J) = 0$, the incoming wave is totally reflected. This is consistent with the theoretical total reflection of coherent signals in one dimension by ideal two-level emitters [67]. Identifying the transmon resonance frequency as $\omega_{01} = 1/\sqrt{L_J C}$, the condition for total reflection becomes $\omega_{01} = \omega\sqrt{1 + B_a/(\omega C)}$. In the experimentally relevant limit $B_a/(\omega C) \ll 1$ we get the approximate resonance condition as

$$\omega_{01} = \omega + \frac{B_a}{2C}. \tag{2.25}$$

The imaginary part of the acoustic impedance gives rise to a shift in the qubit resonance frequency compared to the non-piezoelectric case. This frequency dependent renormalization can be interpreted in a quantum mechanical description as a Lamb shift [68] due to the interaction with the phononic vacuum [69].

2.2.3 Quantum mechanical derivation

Similarly to a qubit capacitively coupled to a superconducting resonator or transmission line, the transmon interacts with SAW via the offset charge induced by the electric field of the SAW wave. We obtain the Hamiltonian of a transmon coupled to a SAW transmission

line by identifying the gate charge in Eq. (2.1) with the surface charge due to SAW, giving

$$\hat{H} = 4E_C(\hat{n} - \hat{n}_s)^2 - E_J \cos \hat{\varphi} = 4E_C\hat{n}^2 - E_J \cos \hat{\varphi} - 8E_C\hat{n}\hat{n}_s + 4E_C\hat{n}_s^2. \qquad (2.26)$$

The interaction term is given by

$$\hat{H}_{\text{int}} = -8E_C\hat{n}\hat{n}_s = 4iE_C \left(\frac{E_J}{2E_C} \right)^{1/4} \hat{n}_s \left(\hat{a} - \hat{a}^\dagger \right) \qquad (2.27)$$

where $\hat{a}$ and $\hat{a}^\dagger$ denote the annihilation and creation operators for the transmon. In this description, the classical gate offset charge n_g has been replaced by the surface charge induced by SAW $\hat{n}_s$, which is related to electric potential $\hat{\phi}(x,t)$ of the SAW field. For a single IDT finger pair it is given by

$$\hat{n}_s = \frac{1}{2e}C_{\text{pair}}\hat{\phi}(x_0, t), \qquad (2.28)$$

where C_{pair} denotes the capacitance of the finger pair and x_0 its position. In analogy with quantum optics, the SAW modes in the substrate can be quantized [70]. As the qubit couples to a continuum of modes in the transmission line, the SAW electric potential has to be integrated over all wavevectors k, giving [67]

$$\hat{\phi}(x,t) = -i\sqrt{\frac{\hbar Z_0 v_{\text{SAW}}}{4\pi}} \int_{-\infty}^{\infty} dk \sqrt{\omega_k} \left(\hat{b}_k e^{-i(\omega_k t - kx)} - h.c. \right). \qquad (2.29)$$

Here we have introduced the annihilation and creation operators for the SAW field obeying $[\hat{b}_k, \hat{b}_{k'}^\dagger] = \delta(k - k')$, as well as the characteristic impedance Z_0 of the SAW transmission line. The SAW velocity v_{SAW} and angular frequency ω_k are related by the linear dispersion relation $\omega_k = v_{\text{SAW}}|k|$. The interaction Hamiltonian for a single finger pair now writes

$$\hat{H}_{\text{int}} = \frac{iE_C}{e} \left(\frac{8E_J}{E_C} \right)^{1/4} \left(\hat{a} - \hat{a}^\dagger \right) C_{\text{pair}}\hat{\phi}(x_0, t). \qquad (2.30)$$

Inserting the expression of Eq. 2.29 with the rotating wave approximation, neglecting fast-rotating terms of the form $\hat{a}\hat{b}$, $\hat{a}^\dagger\hat{b}^\dagger$, this gives

$$\hat{H}_{\text{int}} = -\int_{-\infty}^{\infty} g_0 \left(\hat{a}^\dagger\hat{b}_k e^{ikx_0} + h.c. \right) \sqrt{|k|} dk \qquad (2.31)$$

where

$$g_0 = \frac{E_C}{e} \left(\frac{8E_J}{E_C} \right)^{1/4} \sqrt{\frac{\hbar Z_0}{4\pi}} v_{\text{SAW}} C_{\text{pair}} \qquad (2.32)$$

is the coupling energy density in the wave vector space. From this we obtain the energy relaxation rate for a single finger pair [67, 69]

$$\Gamma_0 = \frac{4\pi g_0^2}{\hbar^2 v_{\text{SAW}}} |k| = \frac{1}{2}\frac{\sqrt{8E_C E_J}}{\hbar} Z_0 C_{\text{pair}}^2 C_{\Sigma}^{-1} \omega_k \qquad (2.33)$$

where C_Σ is the total capacitance of the transmon. We will consider SAW emission into modes close to the IDT frequency and take $\omega_k = \omega_{\text{IDT}}$. Also here the coupling strength can be expressed in terms of the electromechanical coupling coefficient K^2, defined as $K^2 \equiv \omega_{\text{IDT}} Z_0 C_{\text{pair}}$. With the approximation $\sqrt{8 E_J E_c} \approx \hbar \omega_{01}$ we get

$$\Gamma_0 = \frac{1}{2} \omega_{01} K^2 C_{\text{pair}} C_\Sigma^{-1}. \tag{2.34}$$

We will make the approximation that the device capacitance is dominated by the IDT fingers and take $C_\Sigma = N_p C_{\text{pair}}$. Here it is useful to note that the coupling per finger is not independent of the number of fingers N_p due to the role of the total capacitance, and neglecting to take this into account will result in incorrect scaling of the coupling rate with N_p.

To get the total relaxation rate for a device with N_p finger pairs, we have to account for the array factor which sums the contributions from all finger pairs. We again consider a structure with no internal reflections. Similarly as for the simple IDT this yields

$$\Gamma_a(\omega) = \frac{N_p K^2 \omega_{01}}{2} \left(\frac{\sin X}{X} \right)^2. \tag{2.35}$$

In this section we have considered the IDT fingers as pointlike, and do not account for the impact of the spatial extent of the electrodes on the element factor. We still obtain approximately the same expression and, importantly, a consistent scaling with design and material parameters. The expression Eq. (2.35) is valid for the case where the wavelength is much longer than the size of the coupling point.

3

Giant artificial atoms

Light-matter interaction has conventionally been studied in cavity quantum electrodynamics with atoms that are several orders of magnitude smaller than the wavelength of the electromagnetic field. In circuit quantum electrodynamics, artificial atoms in the form of superconducting qubits are of macroscopic dimension, but still interact with microwave fields of much longer wavelength than their typical size. In these cases it is generally a valid approximation to consider the atom as a pointlike dipole in the description of their interaction with light [71]. For a superconducting qubit coupled to surface acoustic waves on the other hand, the qubit IDT spans many wavelengths. As we have seen in the previous section, the interference between coupling points gives rise to a frequency dependent coupling not present in the single dipole case [69]. In principle, this frequency dependence can be designed by engineering the layout and relative interaction strength of the coupling points. This *giant atom* regime of quantum optics opens up possibilities for effects and applications that cannot be easily realized with conventional atoms. Basic examples exploiting frequency-dependent coupling include population inversion [69, 72] and electromagnetically induced transparency (EIT), demonstrated in the acoustic domain in the appended Paper C. More complex setups involving multiple giant atoms coupled to a common transmission line could enable novel applications in quantum information processing. If the coupling points are interleaved between neighbouring giant atoms, the interaction can be engineered such that the giant atoms are protected from decoherence by emitting into the waveguide, while waveguide-mediated atom-atom interactions are preserved [73]. This prediction has been confirmed in a waveguide QED experiment, where two superconducting qubits were coupled to a common waveguide at two points each in a braided layout [74].

In general, while giant atoms are large relative to the coupled field wavelength, their dynamics are still described by master equations in the Born-Markov approximation where
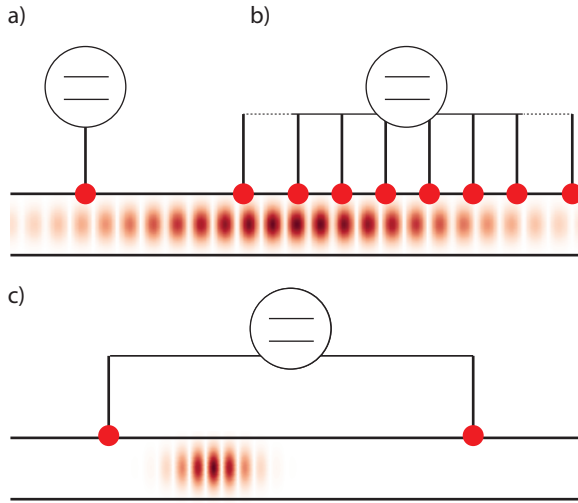
Figure 3.1: Regimes of field-atom interaction. **a)** Ordinary, small atom. **b)** Giant atom with coupling points separated by a distance comparable to the field wavelength. **c)** Non-Markovian giant atom, where the field propagation time is not small compared to the inverse atom relaxation rate.

no memory effects are present [75]. Due to the slow propagation velocity of SAW, the interaction between the SAW field and a qubit can be engineered such that the phonon time-of-flight across the qubit cannot be neglected. This gives rise to an intrinsic time delay, and represents a different parameter regime than the Markovian giant atoms. The simplest case to demonstrate this *non-Markovian* giant atom regime is a qubit coupled to a SAW transmission line at two distant points. If the separation distance takes a longer time for the SAW wave to traverse than the excited state lifetime of the qubit, an initially excited qubit will not decay exponentially, but show revivals in the excited state population due to reabsorption of previously emitted phonons.

Figure 3.1 illustrates giant atom configurations in the Markovian and non-Markovian regimes. In Sec. 3.1 we discuss electromagnetically induced transparency and how it can be observed using giant atoms. We also present results showing EIT in the acoustic domain, as well as experiments towards on-chip routing of SAW signals performed in the same setup. We then proceed to a treatment of non-Markovian giant atom regime in Sec. 3.2.

3.1 Electromagnetically induced transparency

Electromagnetically induced transparency is a quantum interference effect in a three-level medium interacting with two different electromagnetic fields [76]. Interference between excitation pathways in the medium renders it transparent to the *probe* field in the presence of the *control* field. EIT has primarily been observed in cold atomic gasses [77], where the

modified refractive properties associated with the transparent feature in the absorption spectrum has enabled slowing down the group velocity of light below $100\,\text{m/s}$ [78]. In optomechanical systems, the nonlinear radiation-pressure coupling between optical and mechanical modes enable the analogous effect of optomechanically induced transparency [79].

The role of quantum coherence in the transparency effect is somewhat subtle and some attention has been directed towards the proper definition and identification of EIT [80]. In the presence of an oscillating electromagnetic field, atomic levels coupling to the drive split into *dressed states*, separated by an amount proportional to the drive amplitude. If the control tone is strong enough to separate dressed states significantly in relation to the transition linewidth, absorption of the probe beam may be suppressed. This is the Autler-Townes (AT) effect [81] and while very similar in practice to EIT, they are distinct in that AT does not rely on atomic coherence. The two effects may be distinguished using the fact that EIT can be observed also when the control field is too weak to appreciably separate atomic energy levels.

3.1.1   Theory of EIT

We will consider the case of a single three-level artificial atom coupled to a probe and control field. The Hamiltonian for this system can be written as

$$H = \omega_{01}\hat{\sigma}_{11} + \omega_{02}\hat{\sigma}_{22} + \frac{\tilde{\Omega}_p(t)}{2}\left(\hat{\sigma}_{01} + \hat{\sigma}_{10}\right) + \frac{\tilde{\Omega}_c(t)}{2}\left(\hat{\sigma}_{12} + \hat{\sigma}_{21}\right) \qquad (3.1)$$

where the drive strength terms due to the interaction with the external fields are given by

$$\tilde{\Omega}_p = \Omega_p\left(e^{-i\omega_p t} + e^{i\omega_p t}\right), \qquad (3.2)$$

$$\tilde{\Omega}_c = \Omega_c\left(e^{-i\omega_c t} + e^{i\omega_c t}\right). \qquad (3.3)$$

The ladder operators $\hat{\sigma}_{ij} = |i\rangle\langle j|$ for the artificial atom connect the states i and j. For the probe (control) field frequency we assume that $\omega_p \approx \omega_{01}$ ($\omega_c \approx \omega_{12}$), and it holds that $\omega_{02} = \omega_{01} + \omega_{12}$. The effective drive strength of the probe is given by Ω_p and Ω_c is the typically larger drive strength of the control tone.

From input-output theory, the transmission coefficient of the probe beam across the atom is related to off-diagonal elements in the density matrix [82, 83]

$$t = 1 + i\frac{\Gamma_{10}}{\Omega_p}\langle\hat{\sigma}_{01}\rangle. \qquad (3.4)$$

To find the expectation values $\sigma_{01} = \langle\hat{\sigma}_{01}\rangle$ we solve the Heisenberg equations of motion for the ladder operators

$$i\frac{d}{dt}\langle\hat{\sigma}_{ij}\rangle = \left[\hat{\sigma}_{ij}, \hat{H}\right]. \qquad (3.5)$$

Using that $[\hat{\sigma}_{ij}, \hat{\sigma}_{kl}] = \delta_{jk}\hat{\sigma}_{il} - \delta_{il}\hat{\sigma}_{kj}$ we may write Eq. (3.5) for the operators coupling

to the ground state as

$$\frac{d}{dt}\sigma_{01} = -i\omega_{01}\sigma_{01} + i\frac{\tilde{\Omega}_p(t)}{2}\left(\sigma_{11} - \sigma_{00}\right) + i\frac{\tilde{\Omega}_c(t)}{2}\sigma_{02} - \gamma_{01}\sigma_{01}, \qquad (3.6)$$

$$\frac{d}{dt}\sigma_{02} = -i\omega_{02}\sigma_{02} + i\frac{\tilde{\Omega}_p(t)}{2}\sigma_{21} + i\frac{\tilde{\Omega}_c(t)}{2}\sigma_{01} - \gamma_{02}\sigma_{02}, \qquad (3.7)$$

where hats have been removed to indicate expectation values. The effect of decoherence has been added with the rate $\gamma_{0i} = \Gamma_i/2 + \gamma_{\varphi,i}$, where Γ_i is the total spontaneous decay rate of the level $|i\rangle$, and $\gamma_{\varphi,i}$ the pure dephasing rate. In the limit where the probe is weak, we can make the approximation that the artificial atom remains in the ground state and set $\sigma_{11} \approx \sigma_{22} \approx \sigma_{12} \approx \sigma_{21} \approx 0$, $\sigma_{00} \approx 1$. In a doubly rotating frame where

$$\sigma_{01} = S_{01}e^{-i\omega_p t}, \qquad (3.8)$$

$$\sigma_{02} = S_{02}e^{-i(\omega_p+\omega_c)t} \qquad (3.9)$$

this gives

$$\frac{d}{dt}S_{01}e^{-i\omega_p t} = -\left(i\omega_{01} + \gamma_{01}\right)S_{01}e^{-i\omega_p t} + i\frac{\Omega_p}{2}\left(e^{-i\omega_p t} + e^{i\omega_p t}\right) - $$
$$- i\frac{\Omega_c}{2}\left(e^{-i\omega_c t} + e^{i\omega_c t}\right)S_{02}e^{-i(\omega_p+\omega_c)t}, \quad (3.10)$$

$$\frac{d}{dt}S_{02}e^{-i(\omega_p+\omega_c)t} = -\left(i\omega_{02} + \gamma_{02}\right)S_{02}e^{-i(\omega_p+\omega_c)t} - i\frac{\Omega_c}{2}\left(e^{-i\omega_c t} + e^{i\omega_c t}\right)S_{01}e^{-i\omega_p t}. \qquad (3.11)$$

In the steady state we have $(dS_{ij}/dt = 0)$. Making the rotating wave approximation, where fast-rotating terms are assumed to average out to vanish, we may collect the terms in Eqs. 3.10-3.11 and get

$$S_{01}\left(i\left(\omega_p - \omega_{01}\right) - \gamma_{01}\right) = i\frac{\Omega_c}{2}S_{02} - i\frac{\Omega_p}{2}, \qquad (3.12)$$

$$S_{02}\left(i\left(\omega_p + \omega_d - \omega_{02}\right) - \gamma_{02}\right) = i\frac{\Omega_c}{2}S_{01}. \qquad (3.13)$$

Solving for S_{01} gives

$$S_{01} = i\frac{\Omega_p/2}{\gamma_{01} - i\Delta_p + \frac{\Omega_c^2/4}{\gamma_{02}-i(\Delta_p+\Delta_c)}} \qquad (3.14)$$

where $\Delta_p = \omega_p - \omega_{01}$, $\Delta_c = \omega_c - \omega_{12}$ and we have used the fact that $\omega_{02} = \omega_{01} + \omega_{12}$. Inserting into Eq. 3.4 gives for the transmission coefficient

$$t = 1 + \frac{\Gamma_{10}}{2\left(\gamma_{10} - i\Delta_p\right) + \frac{\Omega_c^2}{2(\gamma_{20}-i\Delta_p-i\Delta_c)}}. \qquad (3.15)$$

The reflection r is related to the transmission by the relation $t = 1 + r$. The expression Eq. 3.15 is valid in both the AT and EIT regimes but show some qualitative difference
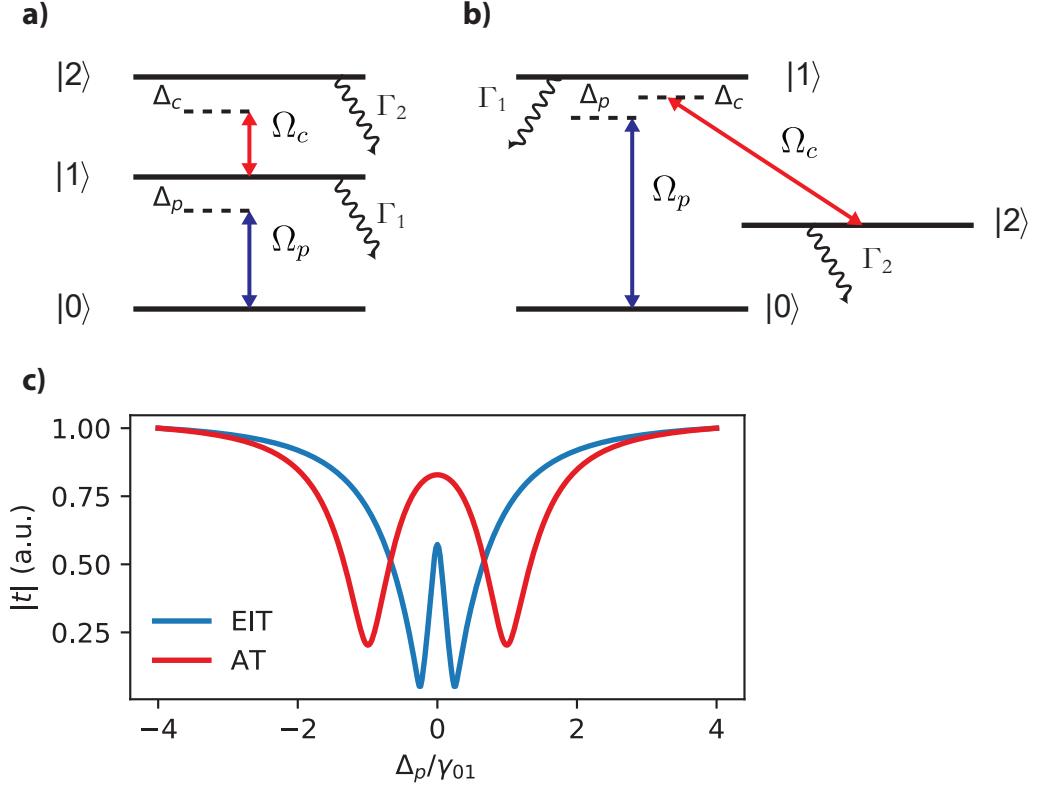
Figure 3.2: Electromagnetically induced transparency and Autler-Townes splitting. The ladder level structure used for realizing EIT with a SAW-coupled qubit is illustrated in **a)**. More common in EIT experiments is the Λ level scheme shown in **b)**. In both cases the transition $|2\rangle - |0\rangle$ is dipole forbidden. To realize EIT, it is necessary that the decoherence of the state $|2\rangle$ is smaller than for the state $|1\rangle$, and the former is sometimes referred to as the *metastable* state for this reason. **c)** Theory curves (Eq. (3.15)) illustrating the transmission as a function of probe detuning Δ_p for the EIT and AT cases. The curve showing EIT (blue) is obtained with the parameter values $\Omega_c = \gamma_{01}/2 = 10\gamma_{02}$. The corresponding values for the AT regime (red) are $\Omega_c = 2\gamma_{01} = 8\gamma_{01}$.

depending on the mechanism behind the transparency. To distinguish EIT from AT [80], we analyse the poles of Eq. 3.15 when $\Delta_p = \Delta_c = 0$. For the case $\Omega_c > \gamma_{01} - \gamma_{02}$, the absorption can be written as a sum of two Lorentzians separated in frequency by Ω_c. The dual Lorentzians are a feature of the dressed-state level splitting associated with the Autler-Townes effect. Genuine EIT is observed in the weak control limit, when $\Omega_c < \gamma_{01} - \gamma_{02}$. Now Eq. 3.15 has imaginary poles, which makes the expression equivalent to the difference between two Lorentzians [80]. Note that to reach this regime, it is a requirement that the decoherence rates satisfy $\gamma_{02} < \gamma_{01}$. This implies the state $|2\rangle$ is longer lived than the first excited state $|1\rangle$. For the ladder-type level scheme of a transmon qubit this is not generally the case, as the coupling rate to propagating modes scales with excitation number as $\Gamma_n \propto \sqrt{n}$. Observations of EIT in superconducting circuits therefore typically involves the engineering of an artificial Λ level structure using qubits interacting with microwave resonators [84]. For SAW-coupled qubits on the other hand, the frequency-dependent coupling rate described in Sec. 2.2.2 allows for satisfying the EIT condition without using the combined states formed by a qubit in a resonator. In Paper C we exploit this property to demonstrate EIT in a propagating acoustic mode. The ladder and Λ level structures are illustrated in Fig. 3.2a-b. We also show a theoretical plot of the transparency feature in the AT and EIT regimes in Fig. 3.2c. A notable qualitative difference is the sharpness of the EIT transparency feature as compared to the AT. The sharp change in absorption with frequency is what gives rise to the slow light propagation in EIT media.

3.1.2 Acoustic EIT measurements

To demonstrate electromagnetically induced acoustic transparency we use a device consisting of a SAW-coupled transmon qubit embedded in a SAW delayline. The qubit has $N_p = 25$ finger pairs and a centre frequency slightly below $2.3\,\mathrm{GHz}$. The device layout is illustrated in Fig. 3.3a. With an anharmonicity of $E_C = 150\,\mathrm{MHz}$, tuning the frequency ω_{01} to maximize the acoustic coupling rate Γ_{01} of the probe transition will place the $|1\rangle - |2\rangle$ transition frequency ω_{12} outside the coupling band of the qubit IDT, as illustrated in Fig. 3.3b. In this configuration the decoherence rate γ_{02} is dominated by other decay channels than acoustic emission, but remains considerably lower than γ_{01}, thus in principle enabling for EIT to be observed. A capacitively coupled gate electrode is used to apply the control tone, electromagnetically inducing the transparency in the acoustic domain.

The acoustic probe frequency is constrained by the limited bandwidth of the delayline IDTs. Directly mapping the transmission as a function of probe frequency to obtain experimental data similar to the theoretical curves in Fig. 3.2c is therefore difficult. We adopt instead a measurement scheme where the probe frequency remains fixed at $\Delta_p = 0$ while sweeping the control tone. This gives rise to a Lorentzian transparency feature in the probe reflection and transmission whose linewidth depends quadratically on Ω_c as

$$\gamma_{\mathrm{EIT}} = \gamma_{02} + \frac{\Omega_c^2}{4\gamma_{01}}. \tag{3.16}$$

By varying the amplitude of the control tone this relation may be exploited to determine the
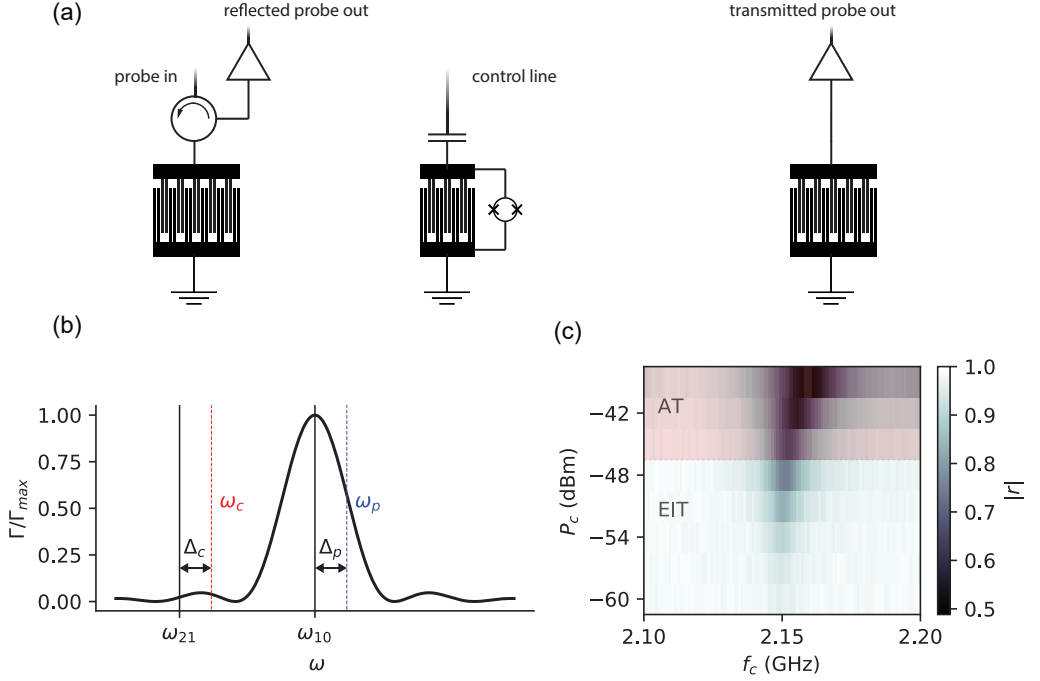
Figure 3.3: **a)** Device schematic. The delayline consists of two IDTs with 150 finger pairs separated by a distance of $400\,\mu\text{m}$. It is used to probe the SAW reflection and transmission of the transmon qubit, which has 25 finger pairs and a capacitively coupled gate electrode where the control signal is applied. **b)** Frequency dependence of the acoustic coupling strength with annotations for the probe and control tone frequencies as well as the transmon transition frequencies. **c)** Probe reflection measured as a function of control frequency and power of the signal applied at room temperature. In the red shaded region the control tone strength $\Omega_c > 16\,\text{MHz}$ and the transparency is due to the AT splitting. For weaker control tones EIT is observed.

parameters Ω_c and γ_{02} required for the unambiguous observation of EIT. The decoherence rate γ_{01} is first determined from the $|0\rangle - |1\rangle$ transition linewidth when the control tone is turned off. In this measurement the probe frequency is fixed while the transition frequency ω_{01} is swept using an external magnetic flux. Estimating this parameter independently from the EIT experiment solves the issue of calibrating the dependence of the control strength Ω_c on the power supplied from the signal generator at room temperature. As the squared amplitude may be assumed to be linear in applied power, this relation is given by $\Omega_c^2 = kP_c$, where P_c is the signal power at room temperature and k a constant which depends on the line attenuation and the coupling capacitance of the transmon to the gate electrode. inserting into Eq. 3.16 yields the linear relationship $\gamma_{\mathrm{EIT}} = \gamma_{02} + \frac{kP_c}{4\gamma_{01}}$. We now measure the EIT linewidth γ_{EIT} as a function of P_c and extract the two free parameters k and γ_{02} from a linear fit.

Using this procedure we obtain $\gamma_{02} = 4.94(14)\,\mathrm{MHz}$ and $\gamma_{01} = 21\,\mathrm{MHz}$, which implies EIT may be observed for control strength below $\Omega_c = 16\,\mathrm{MHz}$. Experimental data where probe reflection is measured as a function of control power and frequency is shown in Fig. 3.3c, with indication of the EIT and AT drive strength regimes. While the IDT delayline setup limits the ability to perform probe frequency sweeps, additional parameter sweeps and analysis still allow for EIT to be observed and distinguished from the AT effect. A different approach to observe EIT with a fixed probe frequency is to tune the transition frequency ω_{01} via an external magnetic flux. This will however tune also the upper transition frequency ω_{12}, sweeping both Δ_p and Δ_c simultaneously. For the transmon, the anharmonicity is fixed by the charging energy and we may take $\omega_{01} - \omega_{12} = E_c/\hbar$, meaning the external flux will uniformly tune the ladder structure. Keeping ω_p and ω_c fixed and setting $\Delta_c = \Delta_p + \delta$ in Eq. 3.15 gives the transmission of the probe signal in this measurement. Here, δ is the residual detuning at $\Delta_p = 0$, accounting for imperfect adjustment of the control frequency to the anharmonicity. Transmission curves showing EIT measured in this way are plotted in Fig. 3.4. Electromagnetic crosstalk and a large detuning $\delta \approx 4\,\mathrm{MHz}$ cause slight asymmetry in the curves. From fits to Eq. 3.15 we obtain $\gamma_{02} = 4.9(6)\,\mathrm{MHz}$. The large error margin reflects the lower precision in this measurement as compared to the reflection data.

3.1.3 Phonon routing

At high control powers, deep in the AT regime, the dressed-state levels are well separated and the transmission is nearly unaffected by scattering off the artificial atom. In Paper B, this is exploited for controlled routing of propagating acoustic signals on the chip. Similarly to an earlier experiment carried out in the microwave domain [85], the application of a strong control signal to the electrical gate controls whether the weak probe signal is reflected or transmitted. Because SAWs propagate slowly, this scheme could be exploited to dynamically catch-and-release SAW pulses. A measurement illustrating this principle is plotted in Fig. 3.5. A train of SAW pulses is launched from an IDT, and depending on the timing of the control pulse to the transmon gate, one of the pulses is transmitted to the IDT on the other side.

The imperfect reflection of the SAW pulses outside the transparent time window is due to pure dephasing of the transmon as well as the elevated SAW power. In the optimized
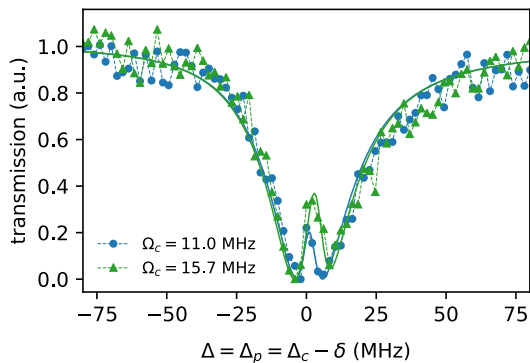
Figure 3.4: EIT measured in transmission. The probe and control frequencies are fixed while sweeping the transmon resonance frequencies ω_{01} and ω_{01} uniformly by an external magnetic flux. Solid lines indicate fits to Eq. 3.15 with $\Delta_c = \Delta_p + \delta$.
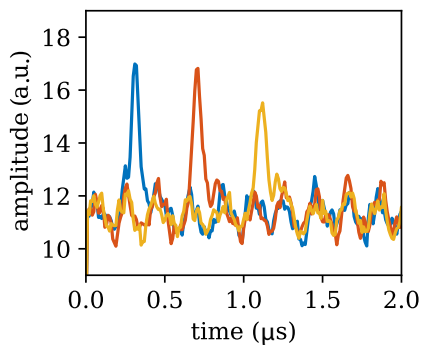

Figure 3.5: Routing of SAW pulses. A control pulse is launched to the gate, rendering the delayline temporarily transparent. The different traces correspond to a different timing of the control pulse.

measurements presented in Paper B we observe an extinction ratio of 80 % in transmission.

3.2 Time delays and non-Markovianity

In most realistic settings, quantum systems under investigation cannot be completely isolated from the outside environment, and the decoherence induced by this coupling has to be accounted for in any description of the system dynamics. In the quantum optical description of quantum systems of interest, such as qubits, coupled to the environment, it is generally assumed that there is no back-flow of information emitted as the qubit undergoes relaxation. This assumption is valid if the environment has many strongly interacting degrees of freedom, and its state remains to a good approximation unaffected by the interaction with the emitter. Well-established methods for this kind of system-environment interaction has been successfully applied in many experimental situations.

A growing body of literature is directed towards the study of the quantum non-Markovian effects arising when this situation does not hold, and the bath coupling to a quantum system has some structure causing the transfer of information back to the dissipative quantum system. Understanding such memory effects may eventually be important to the development of low-noise quantum information processors. Another important scenario where non-Markovian effects cannot be neglected, is when deterministic time-delayed feedback is present in the system. This may be the case in a quantum network where nodes are separated by long distances such that the propagation time of signals between them is large compared to the dynamics of individual emitters.

Predicting the behaviour of quantum systems with time-delayed feedback becomes computationally difficult at long time scales [86]. The state of the system's past gives rise to an extra effective dimension in the problem, leading to the adoption of methods from many-body physics such as matrix product state (MPS) representations in numerical calculations [87]. The effective extra dimension created by time-delayed feedback may also be exploited in other ways to create resource states for quantum computation [88].

3.2.1 Quantum non-Markovianity

While in classical stochastic modelling the definitions of Markovianity are unambiguous, the concepts of probability they are based on do not transfer to a quantum-mechanical picture in a natural way. Defining non-Markovianity for a quantum process requires taking non-classical aspects of the dynamics into account, and a variety of definitions and measures have been introduced. A widely adopted measure of non-Markovianity is based on the evolution of the trace distance. The trace distance between two quantum states described by their respective density matrices ρ_1 and ρ_2 is a measure of their distinguishability given by [89]

$$D\left(\rho_1, \rho_2\right) = \mathrm{Tr} \frac{|\rho_1 - \rho_2|}{2} \tag{3.17}$$

where $|A| = \sqrt{A^\dagger A}$ for any square matrix A. For the special case of a quantum two-level system, D is equal to half the Euclidean norm of the difference vector separating the

two states on the Bloch sphere. The trace distance is a relevant metric to quantum information, as it provides an upper bound on the ability to distinguish the state ρ_1 from ρ_2 by measurement. The success probability that a measurement will correctly discriminate between states prepared in either ρ_1 or ρ_2 is bounded by [90]

$$P_{\text{max}} = \frac{1 + D\left(\rho_1, \rho_2\right)}{2}. \tag{3.18}$$

Under Markovian decoherence the trace distance between any two initial states is monotonically reduced in time, and at times $t > 0$ it holds that $D\left(\rho_1(0), \rho_2(0)\right) \geq D\left(\rho_1(t), \rho_2(t)\right)$ [91, 92]. We define as non-Markovian any process where for some pair of initial states $\rho_1(0), \rho_2(0)$ and time t it holds that

$$\sigma(t) = \frac{d}{dt} D\left(\rho_1(t), \rho_2(t)\right) > 0. \tag{3.19}$$

This implies that the decrease in trace distance is non-monotonic, and at some time $t > 0$ it starts to increase. An increase in distinguishability represents flow of information back into the system, signifying memory effects in the dynamics. The degree of non-Markovianity can be quantified as the total increase in trace distance that the quantum process can generate. This measure is obtained by integrating $\sigma(t)$ over all time subintervals where it is positive, given by [93]

$$\mathcal{N} = \max \int_{\sigma > 0} dt \sigma(t, \rho_1(0), \rho_2(0)). \tag{3.20}$$

The maximum is taken over all possible pairs of initial states. This measure gives the total increase in trace distance for the entire process, corresponding to a total amount of information recovery.

3.2.2 The non-Markovian giant atom

Arguably the simplest form of a non-Markovian quantum system is a single quantum emitter with an intrinsic, deterministic time delay. This setting can be realized with a *giant artificial atom*, a superconducting qubit coupled to a transmission line at two points separated by a distance L. If L is sufficiently large that the time for the emitted radiation to propagate across the giant atom is significant, the relaxation dynamics of the giant atom will be non-Markovian. This regime is difficult to reach with electromagnetic fields, as the high speed of light and achievable coupling rates make devices very large and therefore hard to design and fabricate. Surface acoustic waves propagate with a velocity of $\sim 3000 \, \text{m/s}$, five orders of magnitude slower than the speed of light in vacuum, which enables non-Markovian giant atoms to be engineered based on SAW-coupled transmon qubits. In paper A, we design giant atoms by effectively splitting the IDT of a SAW-coupled qubit into two electrically connected IDTs, as shown schematically in Fig. 3.6. An intially excited atom may emit a phonon from either coupling point. A left-propagating (right-propagating) phonon emitted from the right (left) coupling point, interacts with the atom again after a time $T = d/v_{\text{SAW}}$ given by the separation distance and SAW velocity.
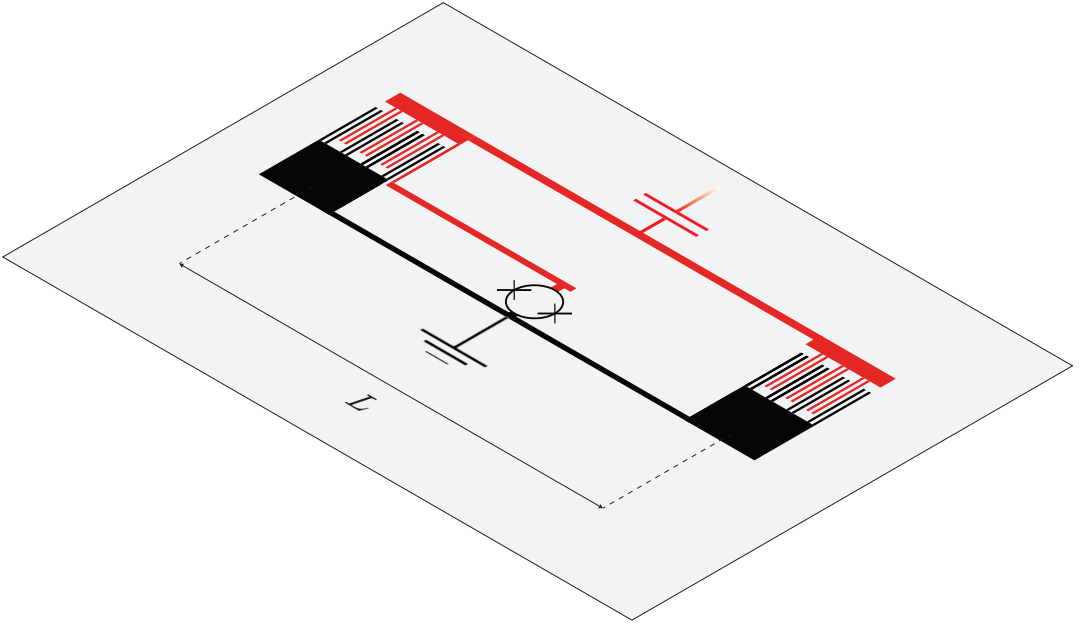
Figure 3.6: Schematic of a SAW-coupled non-Markovian giant atom. The bottom electrode (black) is grounded, and connected to the top electrode (red) via a SQUID. The top electrode is capacitively coupled to an external circuit, which may be either an electromagnetic gate or a readout resonator. Each coupling point consists of a double-finger IDT that is electrically connected via the electrodes. The length L of the giant atom refers to the distance between their respective centres. An external magnetic flux is applied through the SQUID to tune the giant atom frequency ω_{01} into resonance with the coupling point IDT frequency.

Prior theory work by Lingzhen Guo et al. [94] predicted many of the properties of this system. For detailed derivations of the theory laid out in this section we refer the reader to this work as well as the supplementary material to Paper A.

The time evolution of the excited state amplitude a_e of a giant atom with two coupling points in the absence of external driving is given by [94]

$$\frac{\partial a_e(t)}{\partial t} = -i\omega_{01} a_e(t) - \gamma \left(a_e(t) + a_e(t - T) \right). \tag{3.21}$$

Here ω_{01} is the transition frequency of the giant atom and γ denotes the interaction strength of each coupling point. In the limit $T = 0$ there is no time delay and the atom excited state will decay with the rate 2γ. We define the non-Markovian giant atom regime by the criterion $\gamma T > 1$. In this regime the time delay cannot be neglected, and the atom state will undergo significantly non-Markovian time evolution. The time-delayed atom-field interaction gives rise to revivals in the excited state population as the giant atom undergoes relaxation. Assuming the atom is initially in the excited state ($|a_e(0)| = 1$), the solution to Eq. (3.21) is

$$a_e(t) = \sum_{n=0}^{\infty} \Theta(t - nT) \frac{(-\gamma(t - nT))^n}{n!} e^{-i(\omega_{01} - i\gamma - i\gamma_{\mathrm{res}})(t - nT)}, \tag{3.22}$$

where $\Theta(t)$ denotes the Heaviside step function. Here, we have added the effect of residual dissipation γ_{res} corresponding to relaxation through other channels besides SAW emission. The expression Eq. (3.22) shows periodic revivals in the excited state population with period T, as illustrated in Fig. 3.7a.

These revivals correspond to increases in the trace distance of the giant atom state from the ground state, and the dynamics of the giant atom are described by a non-Markovian quantum process. For an arbitrary pair of pure initial states $|\psi_1\rangle$ and $|\psi_2\rangle$ defined on the Bloch sphere [89] as

$$|\psi_i\rangle = \cos \frac{\theta_i}{2} |0\rangle + e^{i\varphi_i} \sin \frac{\theta_i}{2} |1\rangle \tag{3.23}$$

the trace distance can be expressed in terms of the initial state Bloch vector angles and the relaxation of the fully excited initial state $a_e(t)$ as

$$D\left(|\psi_1\rangle, |\psi_2\rangle\right) = \frac{1}{2} |a_e(t)| \sqrt{\left(\cos\theta_1 - \cos\theta_2 \right)^2 |a_e(t)|^2 + \left| \sin\theta_1 - \sin\theta_2 e^{i(\varphi_1 - \varphi_2)} \right|^2}. \tag{3.24}$$

Because of the revivals in $a_e(t)$, $D\left(|\psi_1\rangle, |\psi_2\rangle\right)$ decreases non-monotonically. Evaluating the degree of non-Markovianity according to Eq. (3.20) for the initial pair of the fully excited and ground states gives

$$\mathcal{N}_{01} = \sum_m \left(|a_e(t_m^{\mathrm{max}})|^2 - |a_e(t_m^{\mathrm{min}})|^2 \right) \tag{3.25}$$

with t_m^{max} and t_m^{min} denoting local maxima and minima of $|a_e(t)|$, respectively. The measure of non-Markovianity of the giant atom decay process is given by the pair of initial states for which N is maximal. This occurs for diametrically opposed states on

35

the equator of the Bloch sphere, where $\theta_1 = \theta_2 = \pi/2$ and $\varphi_1 = \varphi_2 + \pi$. Inserting this condition into Eqs. (3.24) and (3.20) yields

$$\mathcal{N} = \sum_m \left(|a_e(t_m^{\max})| - |a_e(t_m^{\min})| \right).\tag{3.26}$$

The amplitude of the revival peaks and hence the degree of non-Markovianity achievable in the giant atom is limited by the efficiency with which the giant atom reabsorbs its own emitted phonons. Larger changes in the trace distance have been observed in processes where the memory effect is caused by the environment rather than an intrinsic time delay [95].

The amplitude of the revivals decays in time and each reach a lower excited state population than the preceding peak. A surprising property of the giant atom is the non-exponential envelope of this decay. Naively one may expect that in each period of the excitation traversing the atom, a fixed proportion of the excitation leaks out, leading to an overall exponential decay. Instead, interference between propagating SAW and emission gives rise to a *polynomial* decay envelope. On long time scales $T \gg 1/\gamma$, this results in a maximal excited state population in each revival peak $P_m = \max |a_e(mT < t < (m+1)T)|^2$ approximately given by

$$P_m \approx \left(1 + \frac{1}{\gamma T} \right) \frac{T}{2\pi t_m^{\max}}.\tag{3.27}$$

Individual revival peaks also exhibit non-exponential relaxation, with later peaks decaying more slowly. The relative positions of local minima and maxima shift with each revival, with the latter given by $t_m^{\max}/T = m + m/(\gamma T)$.

The non-exponential character of the decay is also revealed in the absorption spectrum of the giant atom. A Markovian quantum emitter will have an emission and absorption spectrum that is Lorentzian, with a linewidth corresponding to the decay rate. For the non-Markovian giant atom, interference between coupling points gives rise to a multi-peak spectral structure. For a giant atom excited via an external electromagnetic drive, the absorption spectrum is related to the excited state time evolution via the Wiener-Khinchin theorem [96], assuming the atom is initially in the excited state. The spectrum is calculated in [94] to be given by

$$S_0(\omega) = \frac{\omega_{01}}{|\omega - \omega_{01} + i\gamma(1 + e^{i\omega T}) + i\gamma_{\text{res}}|^2}.\tag{3.28}$$

In the non-Markovian regime this lineshape deviates considerably from the Lorentzian case. An example spectrum for a strongly non-Markovian giant atom with $\gamma T = 8$ is shown in Fig. 3.7b. The spectrum of emitted SAW radiation has an additional factor $(1 + \gamma \cos \omega T)$, due to the filtering by the two coupling points. Experimentally, the spectrum S_0 of Eq. (3.28) is more straightforward to measure using techniques from circuit QED.

3.2.3 Readout of the giant atom

The absorption spectrum and relaxation dynamics of the giant atom can be measured using readout techniques in circuit QED [97] which are implemented in Paper A. There,
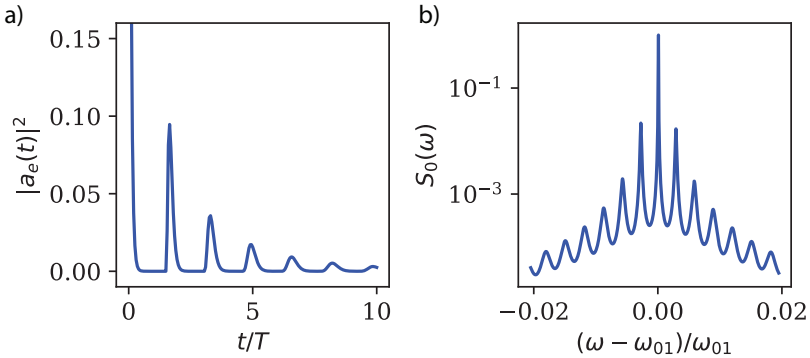
Figure 3.7: **a)** Example of the time evolution of the excited state population for a giant atom given by Eq. (3.22). The parameters are deep in the non-Markovian regime with $\gamma T = 8$ and $\gamma/\gamma_{\mathrm{res}} = 80$. The amplitude of revivals are small compared to the initial state. **b)** Spectrum S_0 a giant atom with the same parameters given by Eq. (3.28) plotted on a logarithmic scale.

a giant atom is capacitively coupled to a coplanar waveguide resonator with a coupling strength g. Figure 3.8a shows an image of such a device. The qubit-resonator system is in the dispersive regime [98, 99, 100], meaning $g \ll \Delta$, where $\Delta = \omega_r - \omega_{01}$ is the qubit-resonator detuning. In this regime the resonator acquires a resonance frequency shift $\Delta\omega_r = \chi \langle \hat{\sigma}_z \rangle$ dependent on the qubit state. Here, $\hat{\sigma}_z$ acts on the qubit state and χ denotes the so-called dispersive shift. For an ideal two-level system this shift amounts to $\chi = g^2/\Delta$ (Appendix A). To account for the limited anharmonicity α of the transmon, this expression has to be modified to lowest order and reads [60, 101]

$$\chi = -\frac{g^2}{\Delta}\frac{\alpha}{\Delta - \alpha}. \tag{3.29}$$

Probing the reflection phase of a signal applied to the resonator therefore allows to readout the excited state population $|a_e|^2 = (1 + \langle \hat{\sigma}_z \rangle)/2$ of the giant atom. For a more complete discussion of dispersive read-out in circuit QED the reader is referred to [62].

Compared to standard, purely microwave-based quantum circuits, the hybrid SAW-qubit platform introduces some limitations to the readout performance. The main constraint on read-out is the short excited state lifetime of the giant atom. The relaxation rate per coupling point amounts to $\gamma \approx 5\,\mathrm{MHz}$, faster than the leak-out rate of signal photons from the resonator of $\kappa \approx 1\,\mathrm{MHz}$. This makes the fast dynamics of the giant atom hard to resolve.

In addition, the microwave circuits suffer from additional loss not present in common circuit QED configuration. The IDT finger structure imposes demands on lithographic precision that are more easily met in a lift-off fabrication process compared to the etching techniques used for high-coherence qubits [102]. Our fabrication process leaves chemical residues inducing loss due to the presence of microscopic two-level systems [103, 104], a topic investigated by acoustic spectroscopy in Ch. 4 of this thesis. In addition, the

piezoelectric substrate necessary for the SAW coupling introduces a loss channel for the microwave circuits, impacting mainly the read-out resonator [105].

To measure the time evolution of the excited state population, a pulse exciting the giant atom is applied via the resonator, and the resonator state is then monitored with a continuous probe signal. While the limited read-out performance causes a smear to the measured relaxation dynamics, the revivals are clearly distinguishable, as shown in Fig. 3.8b.

The spectrum is obtained from a two-tone spectroscopy measurement of the same device. A fixed read-out tone is applied to the resonator, while a pump tone is swept across the giant atom resonance frequency ω_{01}. Absorption of the pump tone by the giant atom will shift the resonance frequency of the resonator ω_r and therefore the amplitude and phase of the readout signal. As this scheme is a measurement of the steady-state it is less susceptible to the slow leak-out rate of photons from the resonator. A giant atom spectrum measured in this way is shown in Fig. 3.8c. We are able to obtain a fit to Eq. (3.28), where the extracted parameters give $L = 550\,\mu\text{m}$ corresponding to the design, and $\gamma = 4.75\,\text{MHz}$.

3.2.4 SAW emission and scattering properties of the giant atom

A SAW-coupled qubit driven by an external electromagnetic signal will continuously emit SAW into the acoustic transmission line. The SAW emission properties of the giant atom will show signs of the non-Markovianity, which can be observed by measuring the reflection of the electromagnetic drive signal. Efficient conversion to SAW will result in a dip in the reflected drive signal amplitude, whose reflectivity is derived in Paper A to be

$$\mathcal{R}_{\text{gate}}(\omega) = \frac{[\omega - \omega_{01} - \gamma\sin(\omega T)]^2 + [\gamma + \gamma\cos(\omega T) - \gamma_{\text{gate}} + \gamma_{\text{res}}]^2}{[\omega - \omega_{01} - \gamma\sin(\omega T)]^2 + [\gamma + \gamma\cos(\omega T) + \gamma_{\text{gate}} + \gamma_{\text{res}}]^2}. \tag{3.30}$$

The coupling strength between the giant atom and the electrical gate is given by γ_{gate}, and it holds that $\gamma \gg \gamma_{\text{gate}}, \gamma_{\text{res}}$. An interesting property of the SAW emission is that is in general not maximal at $\omega = \omega_{01}$, but is subject to additional periodic modulation. The drive frequency ω that yields the maximal transduction of an electromagnetic drive to SAW is given by

$$\omega = \omega_{01} + \gamma\sin\omega T. \tag{3.31}$$

The maximal transduction frequency is offset from the giant atom resonance ω_{01} by a sine modulation whose amplitude is given by the coupling strength and the period determined by the propagation time T. A similar relation holds for the effective total coupling rate, which varies as $\gamma_{\text{tot}} = \gamma\,(1 + \cos\omega T)$. When the emission from each coupling point interferes constructively, the total coupling rate is 2γ, and the coupling is effectively turned off ($\gamma_{\text{tot}} = 0$) for destructive interference. Destructive interference between the emission from each coupling point also enables in theory a form of *dark state*, where the giant atom does not completely decay into the transmission line.

The interference between coupling points is evident in the scattering properties of the giant atom when probed with a coherent SAW beam. The reflection coefficent of SAW is
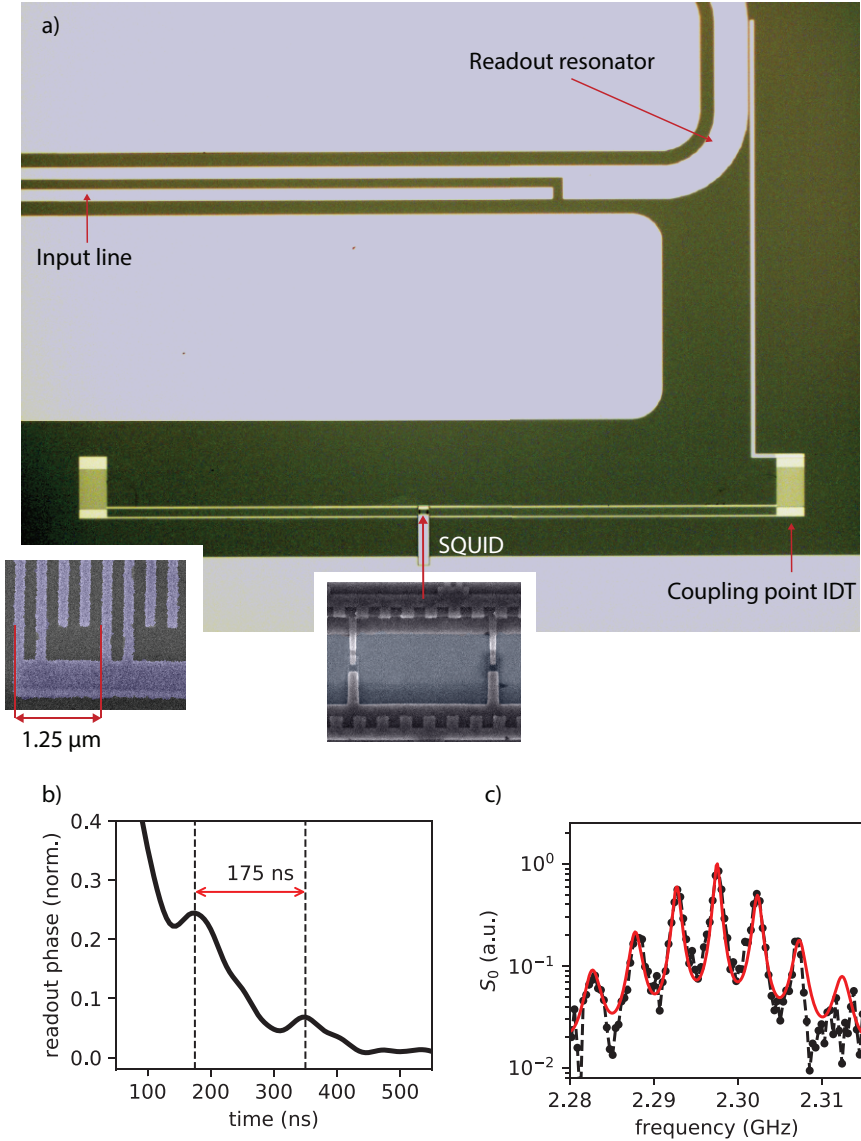
Figure 3.8: **a)** Microscope image of a giant atom device of length $L = 450\,\mu$m with a capacitively coupled readout resonator. Insets show false-colour scanning electron microscope images of the SQUID as well as the IDT finger structure of the coupling point IDTs. Signals to excited the giant and readout are applied to the resonator via the input line. **b)** Time domain trace of the giant atom readout during relaxation. Two revival peaks are visible whose maxima are spaced by 175 ns, consistent with $T = L/v_{\text{SAW}} \approx 160\,$ns. **c)** Spectrum S_0 of a giant atom of length $L = 550\,\mu$m measured in two-tone spectroscopy. The red line shows a fit to Eq. (3.28).
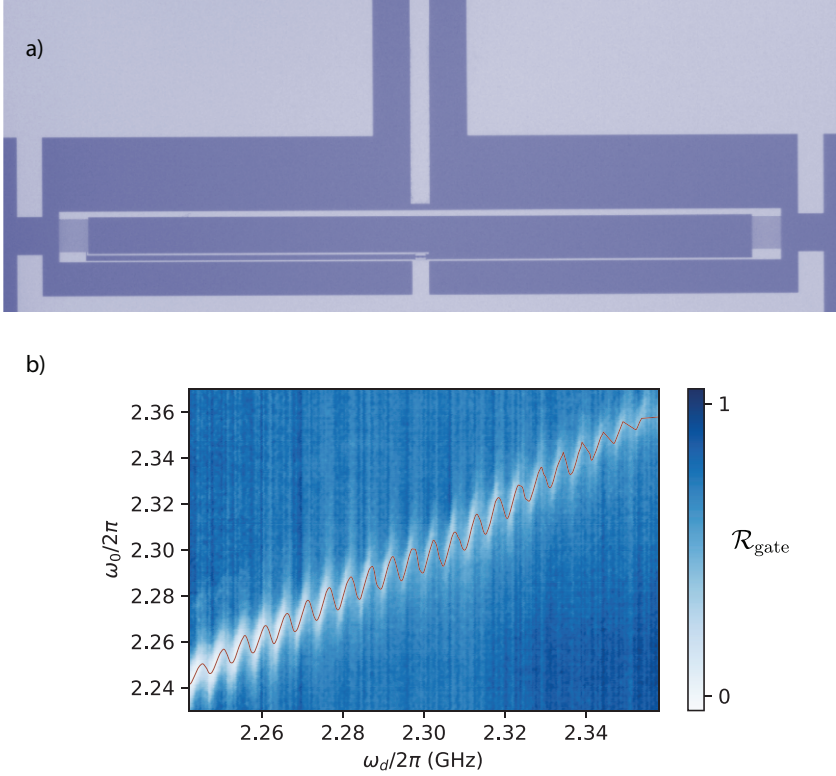
Figure 3.9: **a)** Microscope image of a giant atom device of length $L = 550\,\mu\text{m}$ with an electrical gate. **b)** Gate reflection (normalized) measured with a vector network analyser for a giant atom of the design depicted in **a)**. The modulation of the effective maximal transduction frequency is highlighted by the red line. Towards the edges of the frequency range, the modulation amplitude starts to diminish due to the limited bandwidth of the local coupling point IDTs.

given by [94]

$$\mathcal{R}_{\text{SAW}} = \frac{\gamma^2 \left(1 + \cos \omega T\right)^2}{[\omega - \omega_{01} - \gamma \sin(\omega T)]^2 + [\gamma + \gamma \cos(\omega T) + \gamma_{\text{res}}]^2}. \tag{3.32}$$

A measurement of the gate reflection is more straightforward to implement experimentally than the SAW scattering, as it is not limited in bandwidth by the IDTs of the delayline required for a measurement of the latter.

To measure the SAW emission via $\mathcal{R}_{\text{gate}}$, we design giant atoms with separation distance L ranging from $55\,\mu\text{m}$ to $550\,\mu\text{m}$, and a capacitively coupled electrical gate. The separation distance refers to the distance between the centres of the local IDTs forming the coupling points, each having 16-18 finger pairs. Figure 3.9a shows an image of a device with separation $L = 550\,\mu\text{m}$. In Paper A, we measure the reflection off the electromagnetic gate for three devices with values of the γT parameter spanning an order magnitude, covering the range 0.8-7. To map the giant atom features in the gate reflection, we use an external coil to flux tune the resonance frequency ω_{01} while also sweeping the probe frequency ω. As shown for the $L = 550\,\mu\text{m}$ ($\gamma T = 7$) giant atom in Fig.3.9b, we observe modulation in both the frequency and linewidth.

In the theoretical considerations above, we have neglected the frequency dependence of the interaction with SAW inherent in the local IDTs that form the coupling points. The coupling points themselves span multiple wavelengths, leading to a kind of nesting of giant atom properties! Naturally the description from Ch. 2 of the interaction of qubits with SAW applies to the individual coupling points of the giant atom, whose coupling strength varies with frequency as the square of a sinc-function (Eq. (2.22)). This causes the amplitude of the modulation of maximal emission frequency and coupling strength to diminish as ω and ω_{01} are tuned away from the centre frequency of the coupling point IDTs. This effect can be observed in the gate reflection shown in Fig.3.9b, where the modulation is stronger near the centre of the frequency span.

Summarizing the most important features of the non-Markovian giant atom, we find

- Revivals in the excited state amplitude and associated increase in trace distance,

- non-exponential decay of revival peaks,

- polynomial decay of the envelope of revival peaks,

- non-Lorentzian absorption and emission spectrum with multiple peaks,

- periodic modulation of the effective resonance frequency and interaction strength due to interference.

It is clear that even the simplest case of delayed quantum feedback introduces striking effects to the spectrum and dynamics of excitations.

3.3   Conclusions and outlook

We have exploited the frequency-dependent coupling inherent in giant atoms to demonstrate EIT for an acoustic probe signal. A possible future direction using engineered

frequency-dependent relaxation is suppressing the $|0\rangle - |1\rangle$ coupling and enhancing the $|1\rangle - |2\rangle$ transition, the opposite of the EIT case. This would enable population inversion and possibly single-atom acoustic lasing. Complex setups involving multiple giant atoms with interleaved coupling points may not be straightforward to implement with a SAW platform, but are more readily implemented using a microwave circuit approach.

Taking advantage of the slow propagation speed of SAW, we have realized the non-Markovian giant atom regime with two coupling points. The minimal extension of adding a third coupling point has been shown theoretically to introduce novel kinds of bound states [106]. As engineered quantum systems grow in complexity, understanding the impact of time delays may prove critical to successful design and operation. This would further open the possibility to leverage time-delayed feedback for quantum information processing tasks. A natural next step in this direction is to go beyond the regime of a single excitation discussed here, and investigate the dynamics of the giant atom with multiple phonons emitted within the propagation time.

4

Probing two-level system defects with sound

The problem of decoherence, effectively the loss of quantum information, is central to the development of practical quantum information processing devices. In superconducting circuits, one of the main causes of decoherence is two-level system (TLS) defects residing at surfaces and interfaces. For this reason, the properties of TLSs and their influence on the performance of superconducting qubits and resonators are an intensely studied subject [107]. As TLSs couple to strain as well as electromagnetic fields, surface acoustic waves provide an alternative means of probing and possibly mitigating the loss induced by the TLS ensemble. While using sound waves to probe TLS dynamics is a novel approach to superconducting quantum devices, acoustic experimental methods have a rich history in glass physics [108, 109]. The influence of TLS on the ultrasonic properties of amorphous materials was an active field of research in low-temperature condensed matter physics in the 1960s and 1970s. In fact much of the theory relied on to describe the effect of TLS loss in superconducting circuits was developed in this context. In this chapter we show how SAW resonators at low temperatures can be used to study TLS properties.

4.1   SAW resonators

SAW resonators are defined by a pair of Bragg mirrors, periodic gratings of metal fingers spaced by half the wavelength $\lambda/2$. If the SAW wavelength matches the period of the finger structure, the reflection from each finger will interfere constructively. The arrays therefore act as mirrors, confining the SAW field between them. The resonator is excited via an IDT, and the configuration we will consider in this thesis has a single IDT located in the center of the resonator. A schematic illustration of a SAW resonator is shown in Fig. 4.1. The slow velocity of sound means the SAW wavelength is of the order of $\sim 1\,\mu\text{m}$ at GHz frequencies, which is short compared to the mm-scale of superconducting circuits.

This makes SAW resonator designs relatively compact, which has led to their widespread use as band-pass filters in telecommunications applications. For the same reason it is straightforward to design SAW resonators to support multiple (> 10) modes inside the bandwidth of the IDT and Bragg mirrors that define the cavity. Such a multimode resonator enables two-tone spectroscopy of the TLS ensemble with a frequency resolution corresponding to the free spectral range and a measurement bandwidth constrained by the IDT and mirrors.

4.1.1   Bragg reflectors

An important parameter for mirror design is the complex reflection coefficient of a single finger r_S [8]. The magnitude is typically of the order $|r_S| \sim 0.01$ and depends mainly on substrate material properties. At the center of the stop band where the wavelength matches the pitch such that $p = \lambda/2$, the reflectivity of a mirror with N fingers is given by [8]

$$|R| = \tanh N \, |r_S|. \tag{4.1}$$

The distributed nature of the mirrors means the acoustic field penetrates a finite distance into the mirror structure, making the effective length of the resonator longer than the distance L_e between the leading edge of each mirror. Inside the mirror, the field decays exponentially with a decay length L_m, and the total length of the cavity is given by $L_{\text{tot}} = L_e + 2L_m$. A larger reflectivity per finger $|r_S|$ gives a shorter decay length, which In the highly-reflective limit $N \, |r_S| \gg 1$ is given by

$$L_m = \frac{\lambda_{\text{IDT}}}{4 \, |r_S|}. \tag{4.2}$$

The free spectral range (FSR), the frequency spacing between modes, depends on the total length and SAW velocity as $FSR = v_{\text{SAW}}/(2L_{\text{tot}})$. For symmetry reasons, an IDT that is centered with respect to the mirrors can only excite even modes, meaning the modes accessible to measurement in practice show twice the theoretical FSR of the resonator.

Because of the wavelength-matching condition, Bragg reflectors have a limited bandwidth. In the limit $N \, |r_S| \gg 1$ the bandwidth is given to a good approximation by [8]

$$\frac{\Delta \omega}{\omega_{\text{IDT}}} = \frac{2 \, |r_S|}{\pi}. \tag{4.3}$$

The bandwidth is thus limited by the single-finger reflectivity $|r_S|$. Though it has some dependence on the film properties [110], increasing $|r_S|$ generally involves changing the material to a stronger piezoelectric (greater K^2).

4.1.2   Loss channels for SAW resonators

As we are interested in using a SAW resonator to probe TLS-induced loss, we need to design sufficiently high-quality resonators to be limited by this loss channel. Resonator loss is commonly expressed in terms of the dimensionless *quality factor*, or Q-factor. The

Q-factor is defined as the ratio of the stored energy in the resonator to the energy lost during a radian of oscillation, and can be written as

$$Q = \frac{\omega_r}{\kappa} \tag{4.4}$$

where ω_r is the resonance frequency. The damping rate κ corresponds to the linewidth (full width at half maximum) of the resonance lineshape.

Different loss mechanisms contribute to the Q-factor in a reciprocal way, and we can separate the contributions from internal losses and external coupling as

$$\frac{1}{Q} = \frac{1}{Q_{\text{int}}} + \frac{1}{Q_{\text{ext}}}. \tag{4.5}$$

The internal loss characterized by Q_{int} in turn has contributions from different loss channels, represented by their individual Q-factors. The Q-factor due to the finite grating reflectivity given by Eq. (4.1) is

$$Q_m = \frac{\pi L_{\text{tot}}}{\lambda_{\text{IDT}} \tanh\left(N\left|r_S\right|\right)}. \tag{4.6}$$

While Q_m increases with the number of fingers, in practice it saturates at a value limited by imperfections causing scattering and conversion to bulk waves.

Another contribution to loss arises due to SAW beam diffraction. To suppress diffraction loss, the IDT aperture W must be large compared to the wavelength. In the opposite limit the IDT will act as a point-like source, emitting SAW in all directions. The associated Q-value is given by [111]

$$Q_{\text{diff}} = \frac{5\pi}{\left|1 + \gamma_{bs}\right|} \left(\frac{W}{\lambda}\right)^2. \tag{4.7}$$

The term γ_{bs} represents the effect of beam-steering induced by the anisotropy of the substrate material. For an isotropic material we have $\gamma_{bs} = 1$ while for the 110-direction of GaAs it holds that $\gamma_{bs} = -0.54$ [112]. Fabricating our devices on GaAs thus reduces diffraction losses compared to the isotropic case, provided the alignment is accurate. Other propagation losses typically include viscous damping due to the air (or other gasses or liquids) surrounding the resonator. This loss mechanism allows for using SAW resonators as gas sensors [113], but play little role in the vacuum associated with low temperatures. Instead, the dominant source of propagation loss is due to TLS, which enables using SAW resonators to investigate TLS properties.

4.2 Theory of two-level systems

While the exact microscopic nature of TLSs is not well known, a framework for understanding their interaction with electromagnetic and strain fields is provided by the *standard tunnelling model* (STM). Introduced by Phillips [114, 115] in 1972, this model has had considerable success explaining the low-temperature properties of amorphous solids. The STM models the TLS as a particle in a double-well potential, with two minima
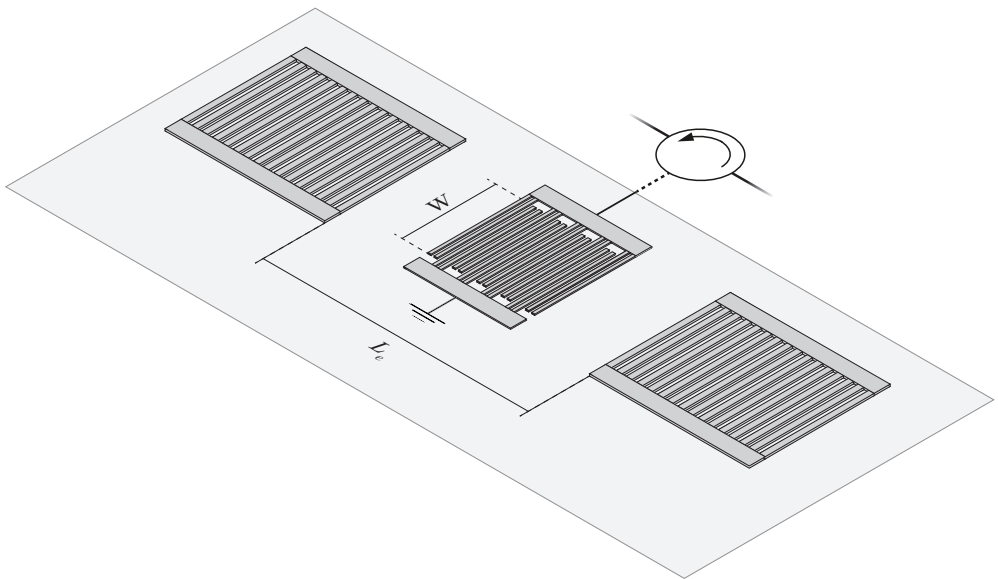
Figure 4.1: Schematic illustration of a SAW resonator. In realistic devices, the Bragg reflectors typically have on the order of $N = 100 - 1000$ fingers each. The IDT in the centre provides a single input and output port, and the resonator is measured in reflection via a circulator.
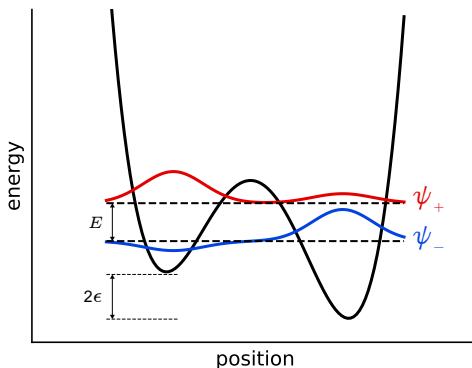
Figure 4.2: Double-well potential for the standard tunnelling model (STM) of TLS. Due to the inter-well tunnelling the eigenstates are given by superpositions of left and right localized states, represented by ψ_+ and ψ_-.

separated by an energy barrier. In the local basis of the potential, the TLS Hamiltonian may be written as

$$H = \frac{\hbar}{2} \begin{pmatrix} \epsilon & \Delta_0 \\ \Delta_0 & -\epsilon. \end{pmatrix} \tag{4.8}$$

Here, ϵ is the asymmetry energy, the energy difference between the two potential wells, and Δ_0 is the tunnelling matrix element. The former is often denoted Δ in the TLS literature, a symbol we will reserve in this chapter for the pump-probe detuning in two-tone experiments. In a diagonal representation the Hamiltonian Eq. 4.8 is given by

$$\hat{H} = \frac{\hbar}{2} E \hat{\sigma}_z \tag{4.9}$$

with the eigenstate energy difference $E = \sqrt{\epsilon^2 + \Delta_0^2}$. The STM potential and associated eigenstates are illustrated in Fig. 4.2. External electric fields and strains may deform the potential, inducing transitions between the two states. The Hamiltonian coupling a single TLS to the strain field is given by

$$\hat{H} = \left(\frac{\epsilon}{E} \hat{\sigma}_z + \frac{\Delta_0}{E} \hat{\sigma}_x \right) \hbar \boldsymbol{\gamma} \mathbf{S} \tag{4.10}$$

where $\boldsymbol{\gamma}$ is a tensor describing the deformation potential interaction of the TLS with the strain field $\mathbf{S}$. This expression neglects variations in the off-diagonal matrix elements [108, 116]. The coupling to the strain field means an excited TLS may undergo relaxation by emitting a phonon, and this mechanism typically limits the excited lifetime T_1 of the TLS. Excitations may also be induced by acoustic signals, such as the surface acoustic waves we will consider here. To account for the SAW-TLS coupling we note that the effective Rabi frequency Ω of the SAW drive is given by

$$\hbar\Omega = 2\boldsymbol{\gamma} \mathbf{S}_{\text{SAW}} \tag{4.11}$$

where $\mathbf{S}_{\text{SAW}}$ is the strain amplitude of the SAW wave. TLSs also couple to electric fields via their electric dipole moment in an analogous manner. While there are experiments investigating the coupling of superconducting qubits to individual TLSs [117], most experimental situations are sensitive to the properties of ensembles of TLSs with a distribution of parameters. An assumption of the STM is that ϵ and Δ_0 are independent and uniformly distributed. This gives a logarithmic density of states, which is usually taken to be constant across the frequencies of interest to a particular experiment.

4.2.1   Two-level systems and loss

One of the most important aspects of the interaction of TLSs with electric and strain field is their contribution to loss in low-temperature quantum devices. The single-excitation limit inherent to TLSs mean that their absorption is saturable. When the Rabi frequency of a driving field exceeds the TLS loss rate such that $\Omega > 1/\sqrt{T_1 T_2}$, the TLS absorption starts to saturate. Here, T_1 and T_2 denote the average longitudinal and transverse relaxation times [109]. The STM predicts the dependence of the internal Q-factor Q_{int} of a resonator on the circulating power as

$$\frac{1}{Q_{\text{int}}(n)} = \frac{1}{Q_{\text{TLS}}(0)} \frac{\tanh \frac{\hbar \omega_r}{2 k_B T}}{\sqrt{1 + \left(\frac{n}{n_C}\right)^{\beta}}} + \frac{1}{Q_{\text{res}}}, \tag{4.12}$$

where power is expressed as the average number of photons or phonons n in the resonator. The Q-factor corresponding to TLS loss is given by Q_{TLS} and Q_{res} represents residual internal losses not due to TLS. At the critical phonon number n_C, the Rabi frequency of the drive equals the TLS dissipation rate (on average) and we have [118]

$$n/n_C = \Omega^2 T_1 T_2. \tag{4.13}$$

The exponent β is a phenomenological parameter introduced to provide a better fit to experimental data. While the STM predicts $\beta = 1$, in practice it is often found that the saturation of TLS loss occurs more slowly as the power is increased, leading to values of $\beta < 1$. An explanation that has been put forward to account for this observation is that TLS-TLS interactions, neglected in the STM, cause TLSs to move in frequency in and out of resonance with the resonator mode [119]. The temperature-dependent factor $1/Q_{\text{int}} \propto \tanh \hbar \omega_r / (2 k_B T)$ accounts for the reduction in loss due to thermal saturation of TLSs. This behaviour may be difficult to explore in superconducting resonators where quasiparticle dissipation becomes an issue at temperatures approaching the superconducting critical temperature T_C. SAW resonators on the other hand are less sensitive to increases in temperature, which may expand the range of temperatures accessible in measurement.

4.2.2 Frequency shifts due to two-level systems

In addition to loss, the interaction of a resonator with TLSs also contributes a frequency shift. An individual TLS will shift the resonator frequency by

$$\Delta\omega_r = \frac{g_{\text{TLS}}^2}{\omega_r - \omega_{\text{TLS}}}\hat{\sigma}_z \tag{4.14}$$

where $g_{\text{TLS}} = \boldsymbol{\gamma}\mathbf{S}_{\text{zpf}}$ is the vacuum coupling strength, defined via the zero-point fluctuations of the SAW field $\mathbf{S}_{\text{zpf}}$. This expression holds in the dispersive regime, where $g \ll \omega_r - \omega_{\text{TLS}}$. The direction of the frequency shift depends on the sign of the detuning, so in order to observe a frequency shift in the resonator from saturating TLSs, this saturation must occur preferentially at either higher or lower frequencies than ω_r. Increasing the circulating power has no effect on the resonance frequency, but varying the temperature does. TLSs at lower frequencies are more readily thermally excited, so changes in TLS saturation with temperature are not symmetric with respect to the resonance frequency. The temperature dependence of the resonance frequency is related to the behaviour of the SAW velocity [109], and according to the STM is given by [120]

$$\frac{\omega_r(T) - \omega_r(0)}{\omega_r(0)} = \frac{1}{\pi Q_{\text{TLS}}}\left[\text{Re }\Psi\left(\frac{1}{2} + \frac{\hbar\omega_r}{2\pi i k_B T}\right) - \ln\frac{\hbar\omega_r}{k_B T}\right]. \tag{4.15}$$

The term containing the digamma function Ψ describes the frequency shift at temperatures where $k_B T \sim \hbar\omega$, and the logarithmic behaviour dominates at higher temperature.

By similar logic, saturation of TLSs due to a driving field may induce a frequency shift provided it is off-resonant with the resonance being probed. In Paper D, we observe this effect in a two-tone experiment pumping and probing different modes in a SAW resonator.

4.3 Two-tone spectroscopy of the two-level system ensemble

As the TLS ensemble effectively acts as a nonlinear dielectric medium, two-tone experiments provide a way to investigate its properties, where the effect of a strong pump tone is detected by a weaker probe tone at a different frequency. The effect of the pump tone is to saturate TLSs with a nearby resonance frequency, similar to the phenomenon of spectral hole-burning in saturable optical media [121, 122]. The shape of this spectral hole depends on the pump power as well as properties of the TLS ensemble. Spectral hole burning may distort the optical gain profile of laser gain media and therefore reduce performance, but can also be exploited in spectroscopy of molecular compounds in solids.

Most studies of TLS interaction with superconducting circuits involve a single mode of a resonator or qubit [103, 117] and microwave circuits such as coplanar waveguide resonators typically have a large mode spacing, comparable to the fundamental resonance frequency. Large mode spacings limit the frequency resolution of two-tone experiments, and previous implementations use the harmonic modes of a superconducting coplanar waveguide resonator [120], or more recently the two normal modes of a system of coupled resonators [123]. In contrast, SAW resonators operating at microwave frequencies can
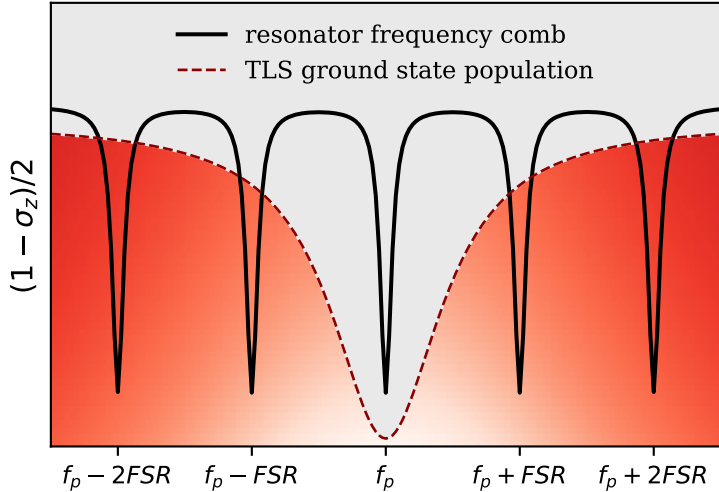
Figure 4.3: Illustration of TLS spectral hole burning in a multimode SAW resonator. The black line shows the comb structure of the SAW modes, spaced by the free spectral range. The ground state population of the TLS ensemble is plotted as a function of detuning from the pump mode (red dashed line and colourscale). A higher unsaturated TLS density within the linewidth of a mode implies more loss, and the effect of the pump is to burn a "hole" in the absorption spectrum of the TLS distribution. Increasing the power of the pump tone will saturate more TLSs cause the width of the spectral hole to widen.

be designed to support multiple modes within the mirror bandwidth, enabling two-tone spectroscopy where the shifts in frequency and loss due to a pump tone are measured in a different probe mode. This scheme is illustrated in Fig. 4.3, where the density of unsaturated TLSs is shown as a function of detuning from the pump mode.

Some efforts have been made to develop a theory for how the TLS-induced damping and frequency shift are affected by an off-resonant pump, that can be used to extract properties of the TLS ensemble from measurements [123, 124]. The model introduced by Kirsh et al [123] is based on the STM and gives the frequency shift of the probe mode as

$$
\frac{\delta\omega_r}{\omega_r \tanh\frac{\hbar\omega_r}{2k_B T}} = -\frac{3\sqrt{2}\tan\delta}{8}\frac{\Delta}{\Omega}\frac{\sqrt{1+\frac{\Omega^2}{2\Delta^2}}-1}{\sqrt{1+\frac{\Omega^2}{2\Delta^2}}+1}.
\tag{4.16}
$$

where Δ is the detuning between the pump and probe modes. The same model predicts the probe mode damping change as

$$
\delta\left(\frac{1}{Q_{\text{TLS}}}\right)\frac{Q_{\text{TLS}}}{\tanh\frac{\hbar\omega_r}{2k_B T}} = -1 - \left(\frac{\Delta}{\Omega}\right)^2\left[6 + 3X\ln\left(1+\left(\frac{\Omega}{\Delta}\right)^2(1-X)\right)\right],
\tag{4.17}
$$

50

where

$$X = \sqrt{1 + 2 \left(\frac{\Delta}{\Omega} \right)^2}. \tag{4.18}$$

The expression Eq. (4.17) is more complicated than a simple Lorentzian spectral hole lineshape, as put forward by Capelle et al [124]. This is because it accounts for some inhomogeneous broadening due to the non-uniform values of g_{TLS} for different individual TLSs, giving rise to the logarithmic term. In principle, measuring the spectral hole lineshape yields an estimate for Ω, which together with a single mode power sweep measurement can be used to extract the average lifetime product $T_1 T_2$ characterizing the TLS ensemble. In addition, by measuring Ω as a function of the pump power, one can obtain an estimate for the mean vacuum coupling rate g_{TLS}. Thus, two-tone spectroscopy is useful for accessing properties of the TLS ensemble that cannot be readily obtained in single mode measurements only.

4.3.1 Spectral hole-burning measurements

In Paper D, we perform two-tone spectroscopy in a SAW resonator with a leading edge separation between the Bragg mirrors of $L_e = 1440 \, \mu\text{m}$. An image of the device is shown in Fig. 4.4. As the wavelength defined by the pitch of the 50-period, double-finger IDT is $\lambda_{\text{SAW}} \sim 4p = 1.2 \, \mu\text{m}$ ($f_r = \omega_r/(2\pi) \approx 2.4 \, \text{GHz}$), the mode numbers of resonances inside the IDT and mirror bandwidth are of the order of 1000. For comparison, coplanar waveguide resonators are commonly designed with a length corresponding to half or a quarter of the wavelength. This gives rise to a narrow FSR of 1.97 MHz, providing good frequency resolution to probe the spectral hole burning. In addition, the high mode numbers mean that each mode has a nearly identical spatial field distribution, with wavelength variations of less than 2 % across the mirror bandwidth. The small variations in the SAW field implies the coupling rate to individual TLSs will be similar for each mode. A frequency sweep of the resonator modes is shown in Fig. 4.5a. The mode used as the pump mode is shown with a fit in Fig. 4.5b.

Since the internal and external quality factors vary slightly between the resonator modes, we fix the pump frequency to a single mode at the center of the comb and measure each remaining resonance lineshape at varying pump powers. The shift in frequency and loss in the probe modes are extracted using standard fitting procedures for high-quality resonators [125]. The result, along with fits to Eqs. (4.16)-(4.17), is shown in Fig. 4.6. Each trace is fit independently, and yields a value for the drive strength Ω. We observe that the scaling of Ω with the number of pump phonons n is not given by $\Omega^2 \propto n$ as predicted by Eq. (4.13), but rather $\Omega^2 \propto n^{\beta_{SH}}$ with $\beta_{SH} \approx 0.6$. This scaling is plotted for the loss and frequency shift in Fig. 4.6c.

Thus to account for the spectral hole burning shape it is necessary to introduce a phenomenological parameter in the same way as the β exponent is introduced to describe the single mode loss saturation in Eq. (4.12). This is in itself not surprising as slower-than-expected scaling is commonly observed in single mode experiments. However, the single mode saturation of the pump mode, shown in Fig. 4.7, yields a value of $\beta = 1.05$ from a fit to Eq. (4.12). The disparity in scaling suggests the presence of additional sources of broadening in the two-tone experiment. This may be due to the effect of the pump tone
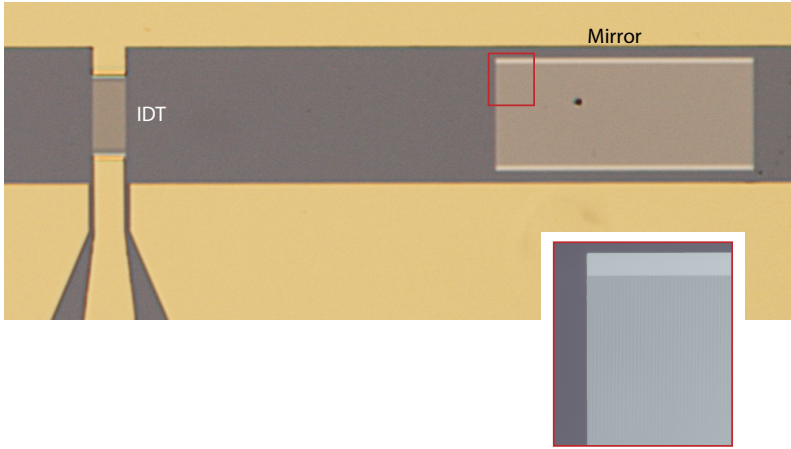
Figure 4.4: Microscope image of the SAW resonator, showing the IDT and right hand Bragg mirror. The left (not shown) and right mirrors are located at an equal distance from the IDT. The IDT and mirrors are fabricated from aluminium on a gallium arsenide substrate, and the ground planes are made of gold.
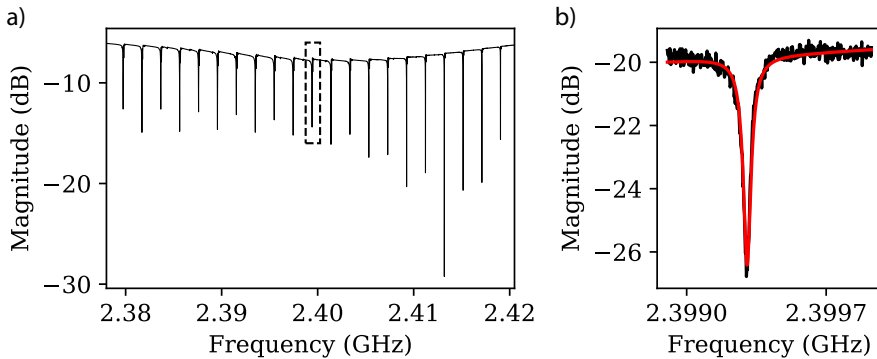

Figure 4.5: Resonator characterisation. **a)** Magnitude of the reflection coefficient of the SAW resonator measured with a vector network analyser at high power ($n \approx 4 \cdot 10^5$). The dashed outline indicates the pump mode at 2.399 GHz. **b)** Zoomed-in reflection measurement of the pump mode resonance at low power ($n < 1$) with a fit to extract the resonance frequency and Q-factor. The different microwave attenuation installed in the respective measurements accounts for the difference in the baseline magnitude.
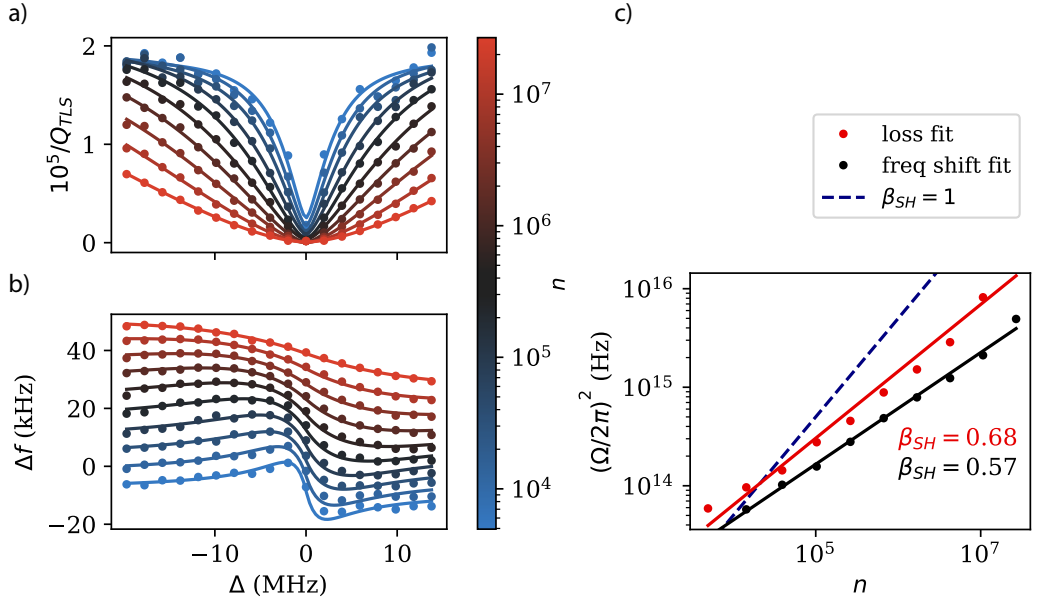
Figure 4.6: Two-tone spectroscopy of the TLS ensemble. A drive tone is applied at the pump mode and the response in the other modes is measured as a function of detuning Δ and the number of pump phonons n. The TLS loss $1/Q_{\mathrm{TLS}}$ is shown in **a)**, with fits (solid lines) to Eq. 4.17. The colour scale indicates the pump phonon number. Applying a detuned pump also induces a frequency shift in the probe mode, plotted in **b)**, with fits to Eq. 4.16. The frequency shift is shown with a $5\,\mathrm{kHz}$ offset between traces. The frequency resolution in the detuning Δ is given by the free spectral range of the resonator. **c)** scaling of the effective Rabi frequency Ω with average phonon number in the pump mode. The data points are extracted from the fits to loss (black) and frequency shift (red) shown in **a)-b)**. Solid lines are fits indicating the scaling with β_{SH}.
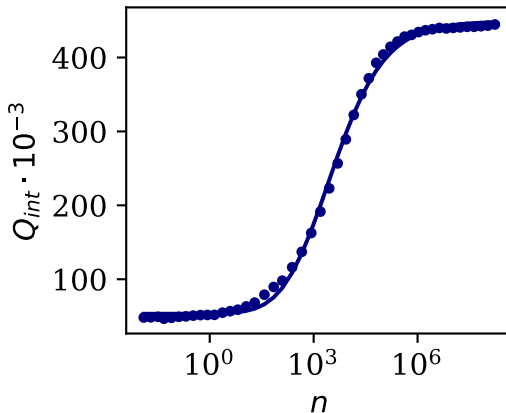
Figure 4.7: Internal Q-factor of the pump mode as a function of phonon number. The solid line is a fit to Eq. 4.12 and gives $\beta = 1.05$.

on TLSs outside the spectral hole linewidth, but more research is required to determine the physical origin of the β_{SH} parameter.

4.4 Conclusions and outlook

We have introduced SAW resonators as an alternative to superconducting circuits as a probe of TLS properties. In particular, we perform two-tone spectroscopy using more than 10 different modes in a multimode SAW resonator. While we find good agreement with theory for measurements at each individual pump power level, further investigation is needed to explain the overall scaling of the saturation with power.

The multimode character of SAW resonators can be exploited for other TLS spectroscopy methods besides spectral hole-burning. Spectral diffusion of TLSs is known to cause frequency noise in resonators [126, 127]. In a SAW resonator, frequency fluctuations can be measured simultaneously in multiple modes. If the noise is caused by dispersively coupled TLSs moving in frequency, this should give rise to correlations in the noise between modes. We measure the frequency fluctuations $\Delta f_i(t)$ in 14 modes of the resonator simultaneously over more than 4 hours, and compute the correlations

$$C_{ij} = \frac{\langle \Delta f_i \Delta f_j \rangle}{\sqrt{\langle \Delta f_i^2 \rangle \langle \Delta f_j^2 \rangle}} \tag{4.19}$$

of the frequency noise between modes i and j. The resulting matrix is shown in Fig. 4.8 and reveals a striking degree of correlation [128]. While this suggests TLSs are involved, it is not clear what process causes far-detuned modes to show anti-correlated frequency fluctuations. Further investigations of this behaviour could provide new insight into the noise induced in superconducting devices by coupling to the TLS ensemble.
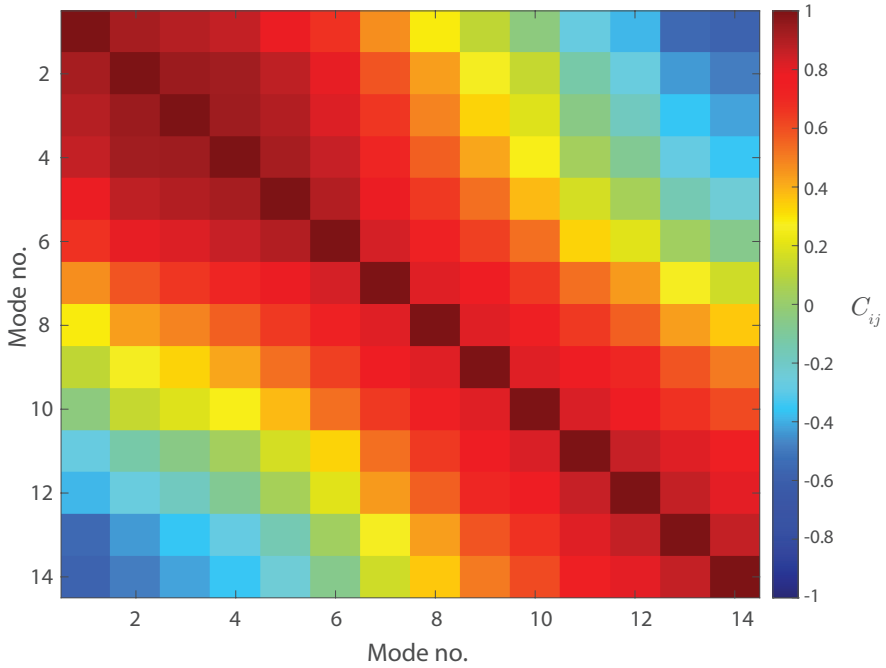
Figure 4.8: Frequency noise correlation matrix. Each index correspond to a mode in the resonator, which implies the correlation matrix is symmetric. The modes are ordered in frequency, and correlations diminish with detuning, although the origin of anti-correlations is not understood at this point.

Besides their multimode character, potential advantages acoustic systems could provide over superconducting resonators is their relative resilience to temperature increases and magnetic fields, which could enable probing the TLS ensemble under different conditions.

5

Multimode nonlinear acoustic resonators

In the previous chapter we have seen how the multimode character of SAW resonators enables frequency-resolved TLS spectroscopy methods. We now turn to the question whether this property can also be an advantage to quantum information processing applications. While individual quantum systems such as transmon qubits can be controlled with high precision, scaling the number of physical qubits in a processor to the extent required for useful quantum computation remains a challenging problem. The increasing complexity of quantum hardware as well as the control electronics required to operate it makes it attractive to explore approaches to quantum computing that encode and process information in compact systems. Measurement-based quantum computation with continuous variables [129] is such a paradigm, which could be explored in multimode hybrid superconducting acoustic quantum systems.

5.1 Measurement-based quantum computing

Gate-based approaches to quantum computing are based on one of many types of physical qubits, in the case of superconducting circuits generally the transmon. Developing a functional quantum computer is then a matter of increasing the number of physical qubits in the processor, along with sufficient connectivity as well as readout and control capability. The current state-of-the-art is at the scale where demonstrations of *quantum supremacy* are possible [3], meaning computations can be carried out that are not useful, but also cannot be performed on any classical computer in a reasonable amount of time. It is not clear whether such noisy intermediate scale quantum (NISQ, [130]) processors will eventually find use in applications, and universal, fault-tolerant quantum computation is expected to require thousands of qubits [131, 132].

An alternative approach is one-way, or measurement-based, quantum computing

(MBQC), where the computation is not carried out by the unitary evolution of a quantum circuit. Instead, the computation starts from a highly entangled *cluster state*, which is then manipulated through measurements rather than unitary two-qubit gates [133, 134, 135]. This makes MBQC a suitable paradigm for systems where large entangled states can be created with the prescribed structure, but multi-qubit unitary operations are not necessarily straightforward to implement. For an explanation of the MBQC model of quantum computing see refs. [136, 137].

Most of the progress towards MBQC implementations has been achieved in the domain of quantum optics. Optical parametric oscillators based on nonlinear crystals have been used to create large scale cluster states [138, 139]. In superconducting circuits, SQUIDs enable the same type of nonlinear processes (with enhanced strength). This has been widely used for parametric amplification, but cluster state generation has received relatively little attention in favour of discrete-variable gate-based approaches. Part of the reason is that time- or frequency-domain multiplexing is difficult to implement in superconducting quantum circuits. The short wavelength and slow velocity of surface acoustic waves may help overcome this limitation and make continuous-variable quantum computing relevant to superconducting circuits operating at microwave frequencies.

5.2   Squeezed states

Quantum mechanical operators obey the Heisenberg uncertainty relation. For two operators A and B it reads

$$\Delta A \Delta B \geq \frac{1}{2} \left| \left\langle \left[\hat{A}, \hat{B} \right] \right\rangle \right| \tag{5.1}$$

where

$$(\Delta A)^2 = \left\langle \left(\hat{A} - \left\langle \hat{A} \right\rangle \right)^2 \right\rangle. \tag{5.2}$$

For the two quadratures of an electromagnetic field mode defined via $\hat{a} = \hat{I} + i\hat{Q}$, $\hat{a}^\dagger = \hat{I} - i\hat{Q}$, we get $\Delta I \Delta Q \geq 1/2$. States where $\Delta I \neq \Delta Q$ are referred to as squeezed states, because the (vacuum) fluctuations depend on the angle in phase space where they are measured. Squeezed states are non-classical when either quadrature variance is below the vacuum limit $(\Delta I)^2 \leq 1/2$ (or $(\Delta Q)^2 \leq 1/2$). For the uncertainty principle to hold the variance of the opposite quadrature is amplified.

The ability to generate squeezed states is an important tool in continuous-variable quantum computing, as well as other quantum information protocols [140, 141]. As squeezing is also associated with noise reduction in one of the quadratures, there are possible applications in sensing, a well-known example being gravitational wave detection [142, 143]. The two-mode squeezed vacuum shows bipartite entanglement, and is one of the most extensively studied examples of entangled states in quantum optics [144]. This state shows squeezing in linear combinations of the two mode quadratures, and is obtained by acting on the vacuum with the two-mode squeezing operator

$$|\xi_{12}\rangle = e^{\xi \hat{a}_1 \hat{a}_2 + \xi^* \hat{a}_1^\dagger \hat{a}_2^\dagger} |0\rangle_1 |0\rangle_2. \tag{5.3}$$

The amount of squeezing is determined by the squeezing parameter $\xi = r \exp(i\varphi)$. This operation can be implemented in a non-degenerate downconversion process, where a photon of frequency $\omega_p = \omega_1 + \omega_2$ is converted into two photons at frequencies ω_1 and ω_2, respectively. In the Fock basis this results in [145]

$$|\xi_{12}\rangle = \frac{1}{\cosh r} \sum_{n=0}^{\infty} e^{in\varphi} (\tanh r)^n |n\rangle_1 |n\rangle_2 . \tag{5.4}$$

The two-mode squeezed vacuum is a superposition of Fock states with the same number of photons in each mode. This is a consequence of the simultaneous two-photon generation, and indicates the states of the modes are highly correlated. The combined state of the squeezed mode pair is characterized by the covariance of the quadrature components $\left\{ \hat{I}_1, \hat{Q}_1, \hat{I}_2, \hat{Q}_2 \right\}$. While measuring the modes separately yields thermal states, the quantum correlations are apparent in the quadrature combinations $\hat{I}_1 - \hat{I}_2$ and $\hat{Q}_1 + \hat{Q}_2$. These variables are squeezed below the standard vacuum limit and give $\left\langle \left(\hat{I}_1 - \hat{I}_2 \right)^2 \right\rangle = e^{-2r}/2$. While commonly associated with electromagnetic modes, the physics of squeezing applies to phononic modes in the same way as discussed here.

5.2.1 Cluster states

A cluster state is multimode entangled state where the entanglement structure can be represented by a graph. A convenient description for the graph is provided by the *adjacency matrix* V_{jk}, whose entries are given by $V_{jk} = 1$ if there is an edge connecting the modes j and k, and $V_{jk} = 0$ otherwise [136]. An ideal continuous variable cluster state satisfies the relation [135]

$$\left(\hat{Q}_j^C - \sum_k V_{jk} \hat{I}_k^C \right) |\psi_V\rangle = 0 \tag{5.5}$$

for the quadrature operators $\hat{Q}_j^C$ and $\hat{I}_j^C$. The superscript C indicates the cluster state basis, which is not in general the physical modes of the system [146]. Universal quantum computation requires the graph represented by V_{jk} to be at least two-dimensional [147], and a square lattice is a common choice. The condition Eq. (5.5) requires infinite squeezing, which is not physically realizable, and the errors associated with the finite squeezing achievable in experiments are an important question to error correction and fault-tolerance [136, 137]. To evaluate cluster-state correlations obtained experimentally, the variance of the operation defined by Eq. (5.5) is compared to the vacuum fluctuations [146].

Cluster states can be created by multimode squeezing processes $\exp(i\hat{H}_G t/\hbar)$ generated by the Hamiltonian [136]

$$\hat{H}_G = i\hbar\kappa \sum_{j,k} G_{jk} \left(\hat{a}_j^\dagger \hat{a}_k^\dagger - \hat{a}_j \hat{a}_k \right) . \tag{5.6}$$

The matrix G_{jk} defines a graph describing pairwise two-mode squeezing among the modes j and k. The amount of squeezing is set by the interaction strength κ, assumed here to be uniform, equivalent to the squeezing parameter per unit time.
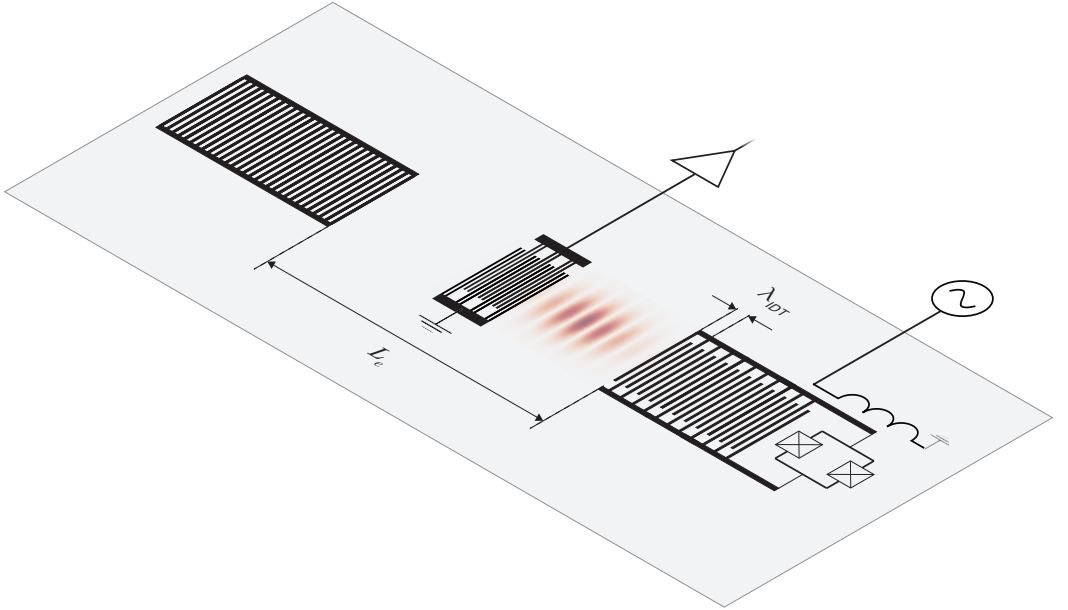
Figure 5.1: Schematic illustration of the QUAKER. The mirror on the right hand side has an interdigitated structure shunted by a SQUID. An on-chip fluxline is used to apply a parametric pump that generates interaction between the SAW modes. An IDT in the center is used for measuring the state of the resonator modes.

5.3 The QUAKER

Our concept for an implementation of MBQC with superconducting circuits is based on a multimode hybrid superconducting-surface acoustic wave resonator. The resonator modes define a frequency comb, and entanglement between modes is generated by a suitable parametric pump. The parametric acoustic resonator, dubbed the *QUantum Acoustic KErr Resonator (QUAKER)*, integrates a SQUID into one of the Bragg reflectors of a SAW resonator. The SQUID mirror is designed similar to a single-finger IDT, with an interdigitated structure where each finger is connected to either the top or bottom electrode. A SQUID shunts the electrodes together. The opposite mirror and IDT are of the same type as for the standard SAW resonator described in Sec. 4.1. In addition to the IDT, there is also an on-chip fluxline to apply a time-varying magnetic flux through the SQUID. Figure 5.1 shows a schematic illustration of the QUAKER layout.

The SQUID mirror consists of an interdigitated structure with N fingers with overlap length W, giving rise to a capacitance $C = NWC_S$ between the top and bottom electrodes. As the electrodes are shunted with the inductance L_J of the SQUID, the mirror functions as a lumped-element, nonlinear electromagnetic resonator with resonance frequency $\omega_{LC} = 1/\sqrt{L_J C}$. The nonlinear SQUID inductance gives this resonance a Kerr-type nonlinearity where the resonance frequency shifts by an amount proportional to the stored

photon number. We will not make use of this effect here other than to note that it accounts for the "KE" in QUAKER.

The piezoelectric coupling to SAW of the reflector finger structure means the lumped-element mirror resonance is weakly coupled to each SAW mode ω_i in the acoustic resonator. The Hamiltonian for this system is given by

$$\hat{H}/\hbar = \frac{\omega_{LC}\hat{a}^\dagger\hat{a}}{2} + \sum_i \omega_i \hat{b}_i^\dagger \hat{b}_i + \sum_i g\left(\hat{a} + \hat{a}^\dagger\right)\left(\hat{b}_i + \hat{b}_i^\dagger\right) \tag{5.7}$$

where we have assumed a uniform coupling strength g. The annihilation (creation) operator for the mirror LC mode is given by $\hat{a}$ ($\hat{a}^\dagger$). The corresponding operators for the SAW modes $\hat{b}_i$ and $\hat{b}_i^\dagger$ satisfy the commutation relation $\left[\hat{b}_i, \hat{b}_j^\dagger\right] = \delta_{ij}$. To suppress excitation of the lossy mirror LC mode, the QUAKER is operated in the regime where $g \ll \omega_i - \omega_{LC}$. The desired mode of operation is where the LC mode remains in the ground state, but is parametrically modulated in a way that induces coupling between different SAW modes. A similar approach is common in superconducting processors, where tunable coupler resonators are used to perform two-qubit gates between otherwise uncoupled transmons [148]. Transforming Eq. (5.7) into the dispersive regime and assuming the LC mode remains approximately in the ground state ($\langle \hat{a}^\dagger \hat{a} \rangle \approx 0$), we get (appendix A)

$$\hat{H}/\hbar = \sum_i \left[\omega_i \hat{b}_i^\dagger \hat{b}_i + \frac{\bar{g}_i}{2}\left((\hat{a}^\dagger)^2 + \hat{a}^2\right)\right] + \frac{1}{2}\sum_{i,j} \tilde{g}_i \left(\hat{b}_i + \hat{b}_i^\dagger\right)\left(\hat{b}_j + \hat{b}_j^\dagger\right). \tag{5.8}$$

The effective coupling between two SAW modes i and j is $\tilde{g}_{ij} = \tilde{g}_i + \tilde{g}_j$ where

$$\tilde{g}_i = g^2 \left(\frac{1}{\omega_i - \omega_{LC}} + \frac{1}{\omega_i + \omega_{LC}}\right) \tag{5.9}$$

The term $(\bar{g}_i/2)\left((\hat{a}^\dagger)^2 + \hat{a}^2\right)$ generates single mode squeezing in the LC mode, with

$$\bar{g}_i = g^2 \left(\frac{1}{\omega_i - \omega_{LC}} - \frac{1}{\omega_i + \omega_{LC}}\right). \tag{5.10}$$

In the absence of a parametric flux pump, the frequency mismatch will prevent the exchange of excitations between SAW modes. Applying a flux pump of frequency ω_p to the on-chip fluxline will modulate ω_{LC} and hence $\tilde{g}_i$. The approximately parabolic dependence of the frequency on flux implies the effective coupling rates are modulated at twice the pump frequency as $\tilde{g}_i = \tilde{g}_{i,0} + \tilde{g}_{i,1}\cos\left(2\omega_p t + \theta_p\right)$. If the modulation frequency is close to the free spectral range, the pump will induce frequency conversion between neighbouring modes, effectively implementing a beam-splitting operation. This form of nearest-neighbour interaction could be relevant to quantum simulation, where the comb in the frequency domain is used as a synthetic lattice [149, 150]. In the case where the modulation frequency is resonant with the sum frequency of two modes, pairs of photons from the pump will be downconverted into the SAW modes, i.e. a two-mode squeezing operation. This downconversion process can generate entanglement between the phonon states of the SAW modes, and the correlations can be revealed from measurements of the acoustic field via the IDT.
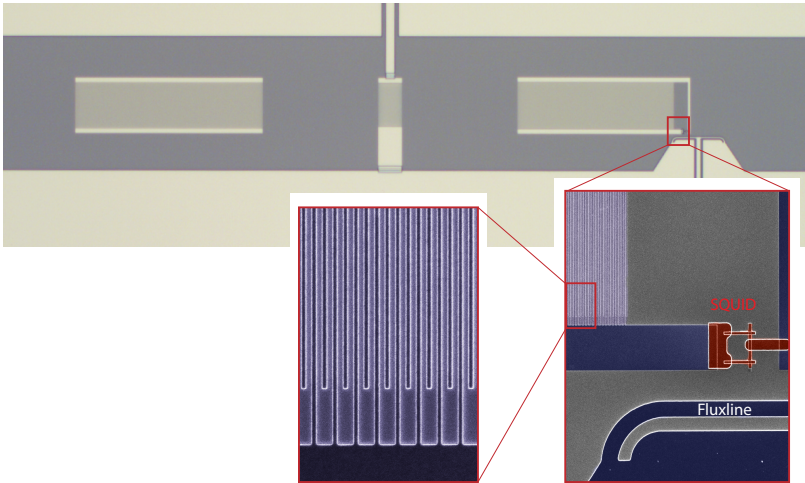
Figure 5.2: Microscope image of the QUAKER device used in experiments. The edges of the Bragg mirrors are separated by $L_e = 600\,\mu\mathrm{m}$. The SQUID mirror on the right hand side has 500 periods (1000) fingers. The sample is fabricated from aluminium on a gallium arsenide substrate. Insets show false-colour scanning electron micrographs of the SQUID, fluxline, and finger structure.

The QUAKER device we use in the experiments presented in Paper E is shown in Fig. 5.2. The leading edge separation is $L_e = 600\,\mu\mathrm{m}$ and due to the SQUID mirror breaking left-right symmetry, the IDT actually couples efficiently to both even and odd modes, giving an effective free spectral range of 2.3 MHz and a frequency comb of more than 25 modes inside the IDT bandwidth.

5.4 Two-mode squeezing measurements

If a pump tone is applied at the frequency of a SAW mode ω_p, the second term in the Hamiltonian Eq. (5.8) will be dominated by terms of the form $\hat{H}_{\mathrm{int}} = (\tilde{g}_{ij}/2)\left(\hat{b}_{i+}\hat{b}_{i-} + \hat{b}_{i+}^\dagger \hat{b}_{i-}^\dagger\right)$, where the probe modes $\omega_{i\pm}$ are placed symmetrically around the pump such that $2\omega_p = \omega_{i+} + \omega_{i-}$. The subscript $+$ $(-)$ indicates a mode above (below) the pump frequency. The time evolution operator associated with this interaction $\exp(i\hat{H}_{\mathrm{int}}t/\hbar)$ has the form of the two-mode squeezing operator in Eq. (5.3). The effect can be understood as a downconversion process where two photons from the pump are converted into one *phonon* in the mode $i+$ and one in the mode $i-$. This is illustrated in Fig. 5.3a, showing the QUAKER spectrum with the pump mode as well as the two nearest probe mode pairs.

Assuming the probe modes are initially in the vacuum state, this results in a multimode
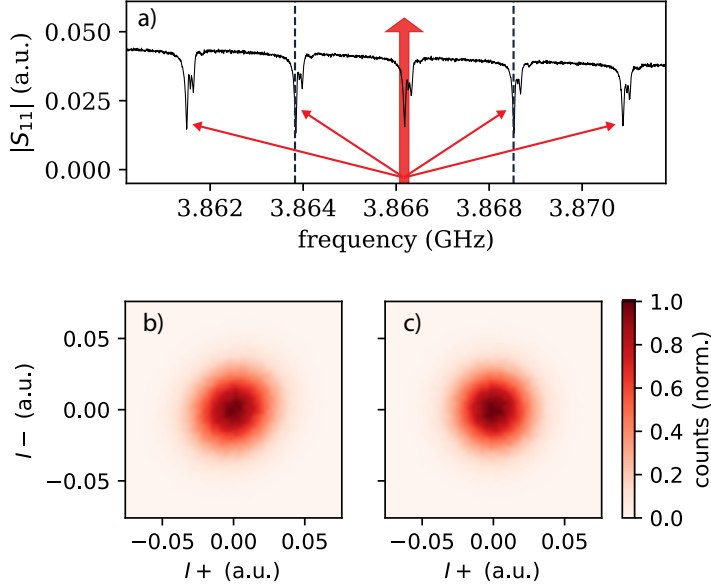
Figure 5.3: Two-mode squeezing measurement. **a)** Spectrum of the QUAKER with the pump frequency indicated by the vertical red arrow. Side arrows illustrate phonon downconversion paths. The small dip immediately above the main resonances in frequency are due to resonant modes with non-zero transversal wavenumber. **b)-c)** Histograms for the I quadratures measured in the mode pair indicated by dashed lines in **a)**. Squeezing appears in the I_+, I_- histogram obtained with the pump on shown in **b)**, but is absent in the pump-off reference histogram plotted in **c)**.

squeezed vacuum, where all mode pairs $\omega_{i\pm}$ are two-mode squeezed. Histograms for the I quadratures measured in the nearest-neighbour (to the pump) modes are shown in Fig. 5.3b. While the I quadratures show squeezing in the axis defined by $I_- - I_+$, plotting the I vs. Q histograms gives a fuzzy circle. To compare the squeezed states to the vacuum level, we also collect reference histograms when the pump is turned off (Fig. 5.3c). As the squeezing is difficult to discern from simple quadrature histograms, subtracting the reference histograms from the squeezed data provides a clearer signature of the features. Subtracted histograms for all four quadrature components of the nearest-neighbour mode pair are shown in Fig. 5.4. The unavoidable presence of thermal noise means the reference histograms do not give the vacuum fluctuations directly, but in Paper E we provide an analysis showing that the squeezing is most likely below this level. The ability to generate entangled states between different phonon modes is a step towards creating larger scale entangled states that are a resource for measurement-based quantum computing.
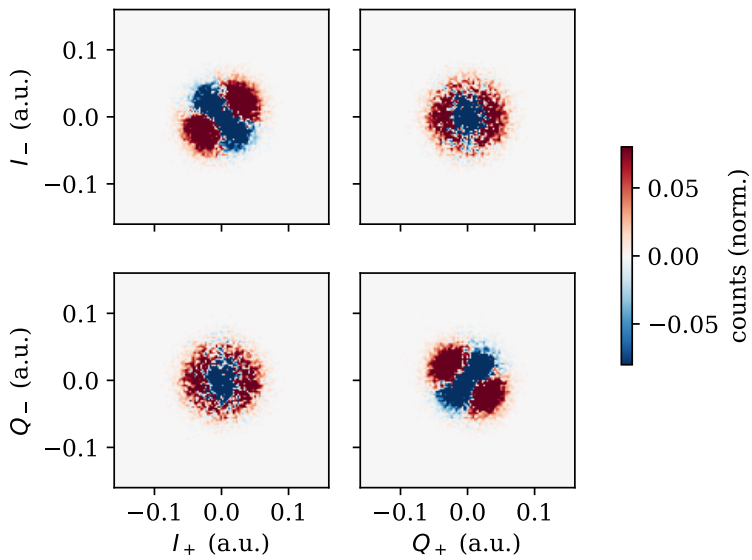
Figure 5.4: Difference between quadrature histograms with the pump turned on and off, for all four quadratures of the mode pair nearest to the pump. Two-mode squeezing is clearly visible in the upper left and bottom right subplots, corresponding to the $\langle I_- I_+ \rangle$ and $\langle I_- I_+ \rangle$ correlations.

5.4.1 Prospects for cluster-state generation

To generate two-mode squeezing between mode pairs we apply a single pump tone. To investigate the possibilities for generating cluster states, this scheme can be extended to add a second pump tone at another SAW frequency. The effective interaction Hamiltonian for this case corresponds to Eq. (5.6), except for a non-uniform coupling strength. The correlations will now not be limited to pairs of modes placed symmetrically around the pump. Figure 5.5a shows the configuration of the two pumps as well as the probe modes labelled f_k. In this scheme, all probe modes will show mutual correlations because of the many possible photon downconversion paths. Because we only probe a limited set of modes, we cannot fully capture the correlations in the comb, and only get qualitative evidence for the presence of entanglement. We define separate correlation matrices for the I and Q quadratures of the five probe modes as

$$C_{jk}^A = \frac{\langle A_j A_k \rangle - \langle A_{j,off} A_{k,off} \rangle}{\sqrt{\langle A_j \rangle^2 \langle A_k \rangle^2}} \tag{5.11}$$

where $A = \{I, Q\}$. The I quadrature correlation matrix is shown in Fig. 5.5b.

The high degree of correlations present in the multimode system is a promising sign for the goal of generating cluster states. Another asset to this research line is the digital microwave electronics platform *Vivace*, which is capable of digitally synthesizing and measuring frequency combs multiplexed to a single measurement channel in the second Nyqvist zone [151]. One implication is that measurements can be performed without analog frequency conversion, simplifying the experimental setup while improving the stability and distortion properties. Compared to optical setups, our approach provides a greater degree of programmable control of the pump spectrum, which may be advantageous for creating particular entanglement structures.

5.5 Conclusions and outlook

We have introduced a new experimental platform, the QUAKER, for quantum computing with continuous variables based on a hybrid superconducting SAW resonator circuit. We show two-mode squeezing of SAW modes and demonstrate important steps towards the generation of cluster states. An important next step is the generation and verification of cluster states of a size approaching the number of modes in the resonator.

The states generated with the QUAKER in the experiments presented here are Gaussian, meaning the associated phase space distributions such as the Wigner function [129, 70] are Gaussian functions. A condition for quantum advantage in computation is the presence of Wigner-negativity in the computational states (or measurements) [152, 153]. A negative Wigner function is associated with quantum effects, and an important class of Wigner-negative states are number states $|n\rangle$ other than the vacuum, which is Gaussian. Squeezing is a Gaussian operation, meaning it preserves the Gaussian nature of the input state. A way to implement non-Gaussian operations and introduce Wigner-negativity in circuit QED is by the interaction with a superconducting qubit. This method has been used to create Wigner-negative states in superconducting microwave cavities [154, 155] as
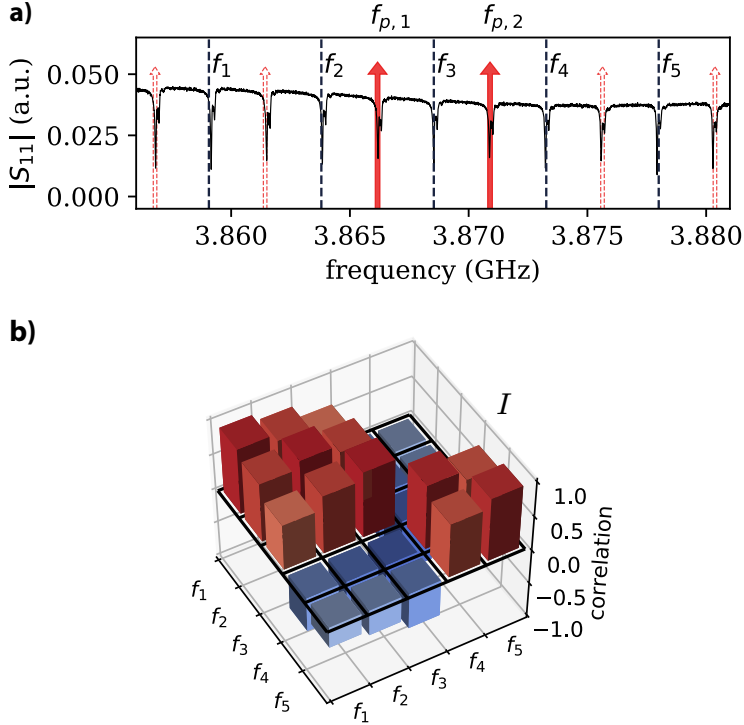
Figure 5.5: Two-pump measurement. **a)** Measurement configuration where the solid red arrows indicate the pump frequencies. Dashed lines indicate probe frequencies for collecting quadrature noise data. The nonlinearity of the device gives rise to intermodulation products at frequencies $f_{IMP} = n_1 f_{p,1} + n_2 f_{p,2}$ which also contribute to pumping. These modes are not measured and are indicated by the red outline arrows. **b)** Correlation matrix for the I quadrature. A mode-selective rotation has been applied to the measured data to separate the I and Q quadratures. The magnitude of the correlations decreases with increased pump-probe detuning. Figure adapted from Paper E.
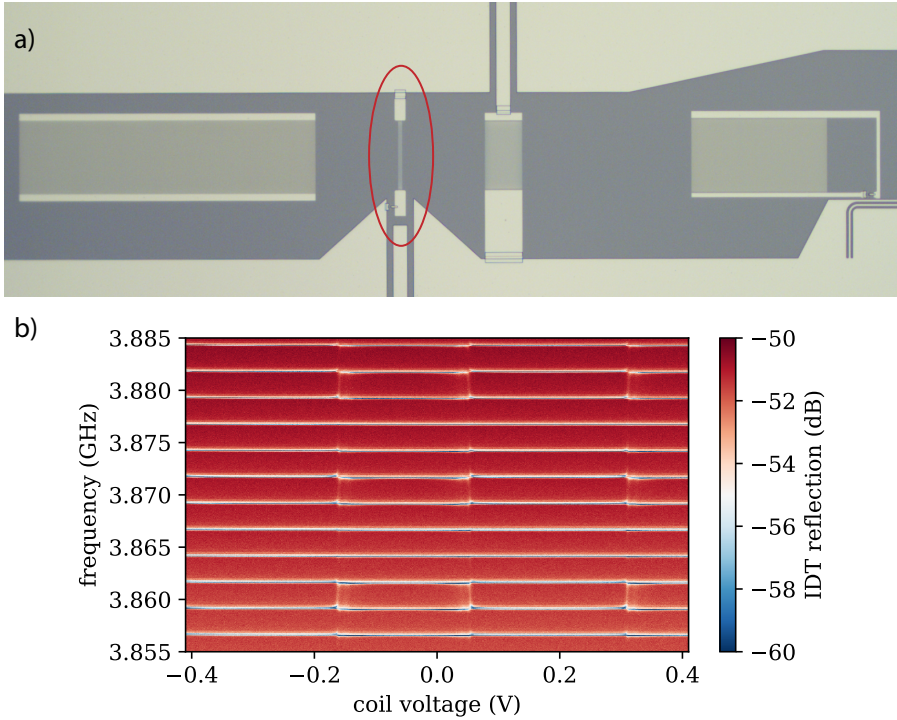
Figure 5.6: QUAKER with an integrated transmon qubit. **a)** Microscope image of the device with the qubit highlighted. **b)** Reflection off the IDT measured with a vector network analyser as a function of frequency and voltage used to drive a coil for flux-tuning the qubit. The SAW resonances appear as horizontal lines, and the SAW-qubit interaction is apparent in the flux-periodic anti-crossings of the qubit and SAW resonances. Due to the differing spatial overlap with the qubit IDT, different SAW modes couple to the qubit with different strength.

well as acoustic resonators [49, 34]. A QUAKER device with an integrated SAW-coupled transmon qubit is shown in Fig. 5.6. The purpose of this device is to generate a cluster state by a suitable pump applied to the SQUID mirror, and then use the transmon qubit to perform non-Gaussian operations such as the subtraction or addition of a single phonon. The next step for this research is to produce genuine cluster states, with the ultimate goal of creating a resource state for measurement-based quantum computation.

A

Dispersive transformations

In the QUAKER, coupling between SAW modes is induced by the common interaction with the LC resonance of the mirror under parametric modulation. The desired regime of operation is where the mirror mode remains in the ground state. We will assume that this is the case and model it as a qubit with raising and lowering operators $\hat{\sigma}_{\pm}$. The total Hamiltonian is a sum of three terms, $\hat{H} = \hat{H}_q + \hat{H}_{\text{SAW}} + \hat{H}_{\text{int}}$ given by

$$\hat{H}_q = \frac{\omega_q \hat{\sigma}_z}{2}, \tag{A.1}$$

$$\hat{H}_{\text{SAW}} = \sum_i \omega_i \hat{b}_i^\dagger \hat{b}_i, \tag{A.2}$$

$$\hat{H}_{\text{int}} = \sum_i g \left(\hat{\sigma}_- + \hat{\sigma}_+ \right) \left(\hat{b}_i + \hat{b}_i^\dagger \right). \tag{A.3}$$

where we have set $\hbar = 1$ for convenience. We transform the Hamiltonian to the dispersive regime by applying the unitary transformation $e^{\hat{S}} \hat{H} e^{-\hat{S}}$ with

$$\hat{S} = \sum_i \left[\lambda_i \left(\hat{\sigma}_+ \hat{b}_i - \hat{\sigma}_- \hat{b}_i^\dagger \right) + \eta_i \left(\hat{\sigma}_- \hat{b}_i - \hat{\sigma}_+ \hat{b}_i^\dagger \right) \right]. \tag{A.4}$$

Evaluating the commutators for the SAW and mirror modes we obtain

$$\left[\hat{S}, \hat{H}_q\right] = \left[\lambda_i \left(\hat{\sigma}_+ \hat{b}_i - \hat{\sigma}_- \hat{b}_i^\dagger\right), \frac{\omega_q \hat{\sigma}_z}{2}\right] + \left[\eta_i \left(\hat{\sigma}_- \hat{b}_i - \hat{\sigma}_+ \hat{b}_i^\dagger\right), \frac{\omega_q \hat{\sigma}_z}{2}\right] \tag{A.5}$$

$$= \sum_i \lambda_i \omega_q \left(\hat{\sigma}_+ \hat{b}_i + \hat{\sigma}_- \hat{b}_i^\dagger\right) + \sum_i \eta_i \omega_q \left(\hat{\sigma}_+ \hat{b}_i^\dagger + \hat{\sigma}_- \hat{b}_i\right), \tag{A.6}$$

$$\left[\hat{S}, \hat{H}_{\text{SAW}}\right] = \left[\lambda_i \left(\hat{\sigma}_+ \hat{b}_i - \hat{\sigma}_- \hat{b}_i^\dagger\right), \sum_i \omega_i \hat{b}_i^\dagger \hat{b}_i\right] + \left[\eta_i \left(\hat{\sigma}_- \hat{b}_i - \hat{\sigma}_+ \hat{b}_i^\dagger\right), \sum_i \omega_i \hat{b}_i^\dagger \hat{b}_i\right] \tag{A.7}$$

$$= -\sum_i \lambda_i \omega_i \left(\hat{\sigma}_+ \hat{b}_i + \hat{\sigma}_- \hat{b}_i^\dagger\right) + \sum_i \eta_i \omega_i \left(\hat{\sigma}_+ \hat{b}_i^\dagger + \hat{\sigma}_- \hat{b}_i\right). \tag{A.8}$$

For the interaction term we use the relation $[A, BC] = [A, B]C + B[A, C]$ and get

$$\left[\hat{S}, \hat{H}_{\text{int}}\right] = \left[\lambda_i \left(\hat{\sigma}_+ \hat{b}_i - \hat{\sigma}_- \hat{b}_i^\dagger\right), \sum_i g \left(\hat{\sigma}_- + \hat{\sigma}_+\right) \left(\hat{b}_i + \hat{b}_i^\dagger\right)\right] +$$
$$\left[\eta_i \left(\hat{\sigma}_- \hat{b}_i - \hat{\sigma}_+ \hat{b}_i^\dagger\right), \sum_i g \left(\hat{\sigma}_- + \hat{\sigma}_+\right) \left(\hat{b}_i + \hat{b}_i^\dagger\right)\right] \tag{A.9}$$

$$= \sum_{i,j} \lambda_i g \hat{\sigma}_z \left(\hat{b}_i + \hat{b}_i^\dagger\right) \left(\hat{b}_j + \hat{b}_j^\dagger\right) + \sum_i \lambda_i g \left(\hat{\sigma}_+ + \hat{\sigma}_-\right)^2 + \tag{A.10}$$

$$- \sum_{i,j} \eta_i g \hat{\sigma}_z \left(\hat{b}_i + \hat{b}_i^\dagger\right) \left(\hat{b}_j + \hat{b}_j^\dagger\right) + \sum_i \eta_i g \left(\hat{\sigma}_+ + \hat{\sigma}_-\right)^2 \tag{A.11}$$

$$= \sum_{i,j} g \hat{\sigma}_z \left(\lambda_i - \eta_i\right) \left(\hat{b}_i + \hat{b}_i^\dagger\right) \left(\hat{b}_j + \hat{b}_j^\dagger\right) + \sum_i g \left(\lambda_i + \eta_i\right) \left(\hat{\sigma}_+ + \hat{\sigma}_-\right)^2. \tag{A.12}$$

If we choose $\lambda_i = g/\left(\omega_q - \omega_i\right)$ and $\eta_i = g/\left(\omega_q + \omega_i\right)$, we obtain

$$\left[\hat{S}, \hat{H}_q + \hat{H}_{\text{SAW}}\right] = -\hat{H}_{\text{int}}. \tag{A.13}$$

From the Baker-Hausdorff formula we have

$$e^{\hat{S}} H e^{-\hat{S}} = H + \left[\hat{S}, H\right] + \frac{1}{2!} \left[\hat{S}, [S, H]\right] + \dots \tag{A.14}$$

$$= \hat{H}_q + \hat{H}_{\text{SAW}} + \hat{H}_{\text{int}} + \left[S, \hat{H}_{\text{int}}\right] - \hat{H}_{\text{int}} + \frac{1}{2!} \left[\hat{S}, -\hat{H}_{\text{int}} + \left[\hat{S}, \hat{H}_{\text{int}}\right]\right] + \dots \tag{A.15}$$

$$= \hat{H}_q + \hat{H}_{\text{SAW}} + \frac{1}{2} \left[S, \hat{H}_{\text{int}}\right] + \dots \tag{A.16}$$

Assuming the mirror remains in the ground state implies ($\hat{\sigma}_z = -1, \hat{\sigma}_+ \hat{\sigma}_- = 0$). Eliminating these operators we end up with the dispersive Hamiltonian

$$H = \sum_i \left[\omega_i \hat{b}_i^\dagger \hat{b}_i + \frac{g^2}{2} \left(\frac{1}{\omega_q - \omega_i} + \frac{1}{\omega_q + \omega_i}\right) \left(\hat{\sigma}_+^2 + \hat{\sigma}_-^2\right)\right] -$$
$$- \frac{g^2}{2} \sum_{i,j} \left(\frac{1}{\omega_q - \omega_i} - \frac{1}{\omega_q + \omega_i}\right) \left(\hat{b}_i + \hat{b}_i^\dagger\right) \left(\hat{b}_j + \hat{b}_j^\dagger\right). \tag{A.17}$$

Defining $\tilde{g}_i = g^2 \left(1/(\omega_q - \omega_i) - 1/(\omega_q + \omega_i) \right)$ and $\bar{g}_i = g^2 \left(1/(\omega_q - \omega_i) + 1/(\omega_q + \omega_i) \right)$ turns the Hamiltonian into

$$H = \sum_i \left[\omega_i \hat{b}_i^\dagger \hat{b}_i + \frac{\bar{g}_i}{2} \left(\hat{\sigma}_+^2 + \hat{\sigma}_-^2 \right) \right] - \frac{1}{2} \sum_{i,j} \tilde{g}_i \left(\hat{b}_i + \hat{b}_i^\dagger \right) \left(b_j + b_j^\dagger \right) \tag{A.18}$$

which retains single and two-mode squeezing terms.

A similar analysis can be applied to the case of a qubit coupled to a readout resonator. Considering only one resonator mode of frequency ω_r with associated ladder operators $\hat{b}$, $\hat{b}^\dagger$. and making the *rotating wave approximation*, we get the well-known Jaynes-Cummings Hamiltonian

$$\hat{H}_{JC} = \omega_r \hat{b}^\dagger \hat{b} + \frac{\omega_q \hat{\sigma}_z}{2} + g \left(\hat{\sigma}_- \hat{b}^\dagger + \hat{\sigma}_+ \hat{b} \right). \tag{A.19}$$

Compared to Eq. (A.3) this corresponds to discarding rapidly rotating interaction terms, retaining only $\hat{\sigma}_- \hat{b}^\dagger$ and $\hat{\sigma}_- \hat{b}^\dagger$. The corresponding dispersive transformation is defined by

$$\hat{S}_{JC} = \lambda \left(\hat{\sigma}_+ \hat{b} - \hat{\sigma}_- \hat{b}^\dagger \right). \tag{A.20}$$

The dispersive Hamiltonian is given by the surviving terms of Eq. (A.12) giving

$$H_{\text{disp}} = \left(\omega_r + \chi \hat{\sigma}_z \right) \hat{b}^\dagger \hat{b} + \frac{\omega_q + \chi}{2} \hat{\sigma}_z \tag{A.21}$$

with the dispersive shift $\chi = g^2/(\omega_q - \omega_r)$. To reproduce the dispersive shift given in Eq. (3.29) one has to account also for the effect of the second excited state in the transmon. Our result is valid however for the frequency shift induced by resonator coupling to a TLS (Eq. (4.14)).

B
Device fabrication recipes

The samples measured in this thesis were fabricated in the Nanofabrication Laboratory at the Department of Microtechnology and Nanoscience, Chalmers. The fabrication steps are outlined below.

E-beam lithography for IDT structures

1. Spin-coat resist MMA EL4 at 6000 rpm for 60 seconds (thickness $\sim 60\,\mathrm{nm}$), bake for 5 minutes at 180°C.

2. Spin-coat resist PMMA A3 at 6000 rpm for 60 seconds (thickness $\sim 100\,\mathrm{nm}$), bake for 5 minutes at 180°C.

3. Expose with e-beam (100 keV) with a dose of $250\,\mu\mathrm{C/cm^2}$

4. Develop under light agitation in MIBK:IPA 1:1 for 60 seconds.

5. Ash with oxygen plasma at 50 W for 10 seconds.

6. Deposit aluminium in an e-beam evaporator (Plassys or Lesker PVD225).

7. Lift-off with Remover 1165. Heat the remover (~ 60°C) before inserting the wafer and leave for 12+ hours. Finish the liftoff with light ultrasonication.

Direct-write photolithography

Maskless photolithography is used for large device features such as ground planes and coplanar waveguide feedlines and resonators.

1. Spin-coat resist LOR3A at 6000 rpm for 60 seconds (thickness $\sim 60\,\mathrm{nm}$), bake for 5 minutes at 180°C.

2. Spin-coat resist S1805 at 3000 rpm for 60 seconds (thickness $\sim 100\,\mathrm{nm}$), bake for 5 minutes at 110°C.

3. Expose with direct-write laser using the settings focus +50, intensity 90 % and transmission 100 %.

4. Develop under light agitation in MF319 for 60 seconds.

5. Ash with oxygen plasma at 50 W for 20 seconds.

6. Deposit metal in an e-beam evaporator (Plassys or Lesker PVD225).

7. Lift-off with Remover 1165.

E-beam lithography and angle evaporation for Josephson junctions

Here we describe the process used to fabricate junctions with the *Manhattan* technique. This method requires a second lithography steps to connect the finished junctions to the device.

Junctions

1. Spin-coat resist MMA EL12 at 3000 rpm for 60 seconds, bake for 5 minutes at 160°C.

2. Spin-coat resist PMMA 950k A6 at 6000 rpm for 60 seconds (total bilayer thickness $\sim 950\,\mathrm{nm}$), bake for 5 minutes at 160°C.

3. Expose with e-beam (100 keV) with a dose of $950\,\mu\mathrm{C/cm}^2$

4. Develop under light agitation in MIBK:IPA 1:1 for 60 seconds, followed by IPA for 30 seconds.

5. Ash with oxygen plasma at 25 W for 20 seconds.

6. Deposit aluminium in the Plassys evaporator.

    - Deposit 50 nm of aluminium at 45° tilt angle.
    - Oxidize at 2 mBar pressure for 20 minutes
    - Deposit 110 nm of aluminium at 45° tilt angle and 90° planetary rotation.
    - Oxidize at 10 mBar pressure for 10 minutes

7. Lift-off with Remover 1165.

Patches

1. Spin-coat resist MMA EL10 at 3000 rpm for 60 seconds, bake for 5 minutes at 160°C.

2. Spin-coat resist PMMA 950k A6 at 6000 rpm for 60 seconds (total bilayer thickness $\sim 750\,\mathrm{nm}$), bake for 5 minutes at 160°C.

3. Expose with e-beam ($100\,\mathrm{keV}$) with a dose of $950\,\mathrm{\mu C/cm^2}$

4. Develop under light agitation in MIBK:IPA 1:1 for 60 seconds, followed by IPA for 30 seconds.

5. Ash with oxygen plasma at $25\,\mathrm{W}$ for 20 seconds.

6. Deposit aluminium in the Plassys evaporator.

   - Ion milling wiht beam at $400\,\mathrm{V}$, $20\,\mathrm{mA}$, acceleration voltage $60\,\mathrm{V}$ for three and a half minutes.
   - Deposit $200\,\mathrm{nm}$ of aluminium at no tilt.
   - Oxidize at $10\,\mathrm{mBar}$ pressure for 10 minutes.

7. Lift-off with Remover 1165.

Acknowledgements

Bibliography

[1] A. Wallraff, D. I. Schuster, A. Blais, L. Frunzio, R. S. Huang, J. Majer, S. Kumar, S. M. Girvin, and R. J. Schoelkopf. Strong coupling of a single photon to a superconducting qubit using circuit quantum electrodynamics. *Nature* **431**.7005 (2004), 162–167.

[2] R. J. Schoelkopf and S. M. Girvin. Wiring up quantum systems. *Nature* **451**.7179 (2008), 664–669.

[3] F. Arute et al. Quantum supremacy using a programmable superconducting processor. *Nature* **574**.7779 (2019), 505–510.

[4] L. Rayleigh. On Waves Propagated along the Plane Surface of an Elastic Solid. *Proceedings of the London Mathematical Society* **s1-17**.1 (1885), 4–11.

[5] R. M. White and F. W. Voltmer. Direct Piezoelectric Coupling to Surface Elastic Waves. *Applied Physics Letters* **7**.12 (1965), 314–316.

[6] S. Datta. *Surface Acoustic Wave Devices*. Prentice Hall, 1986.

[7] S. H. Simon. Coupling of surface acoustic waves to a two-dimensional electron gas. *Physical Review B* **54** (1996), 13878–13884.

[8] D. Morgan. *Surface Acoustic Wave Filters: With Applications to Electronic Communications and Signal Processing*. Elsevier Science, 2010.

[9] M. Scigliuzzo. *Optimization of SAW filters and resonators*. Master's thesis. University of Salento, 2016.

[10] C. Caliendo, P. Verardi, E. Verona, A. D'Amico, C. D. Natale, G. Saggio, M. Serafini, R. Paolesse, and S. E. Huq. Advances in SAW-based gas sensors. *Smart Materials and Structures* **6**.6 (1997), 689–699.

[11] C. Caliendo and M. Hamidullah. Guided acoustic wave sensors for liquid environments. *Journal of Physics D: Applied Physics* **52**.15 (2019), 153001.

[12] A. Wixforth, C. Strobl, C. Gauer, A. Toegl, J. Scriba, and Z. v. Guttenberg. Acoustic manipulation of small droplets. *Analytical and Bioanalytical Chemistry* **379**.7 (2004), 982–991.

[13] T. Franke, S. Braunmüller, L. Schmid, A. Wixforth, and D. A. Weitz. Surface acoustic wave actuated cell sorting (SAWACS). *Lab on a Chip* **10** (2010), 789–794.

[14] A. Hernández-Mínguez, Y.-T. Liou, and P. V. Santos. Interaction of surface acoustic waves with electronic excitations in graphene. *Journal of Physics D: Applied Physics* **51**.38 (2018), 383001.

[15] R. Fandan, J. Pedrós, A. Hernández-Mínguez, F. Iikawa, P. V. Santos, A. Boscá, and F. Calle. Dynamic Local Strain in Graphene Generated by Surface Acoustic Waves. *Nano Letters* **20**.1 (2020), 402–409.

[16] R. Fandan, J. Pedrós, J. Schiefele, A. Boscá, J. Martínez, and F. Calle. Acoustically-driven surface and hyperbolic plasmon-phonon polaritons in graphene/h-BN heterostructures on piezoelectric substrates. *Journal of Physics D: Applied Physics* **51**.20 (2018), 204004.

[17] L. Dreher, M. Weiler, M. Pernpeintner, H. Huebl, R. Gross, M. S. Brandt, and S. T. B. Goennenwein. Surface acoustic wave driven ferromagnetic resonance in nickel thin films: Theory and experiment. *Physical Review B* **86** (2012), 134415.

[18] P. Kuszewski, I. S. Camara, N. Biarrotte, L. Becerra, J. von Bardeleben, W. S. Torres, A. Lemaítre, C. Gourdon, J.-Y. Duquesne, and L. Thevenard. Resonant magneto-acoustic switching: influence of Rayleigh wave frequency and wavevector. *Journal of Physics: Condensed Matter* **30**.24 (2018), 244003.

[19] A. Wixforth, J. P. Kotthaus, and G. Weimann. Quantum Oscillations in the Surface-Acoustic-Wave Attenuation Caused by a Two-Dimensional Electron System. *Physical Review Letters* **56** (1986), 2104–2106.

[20] A. O. Govorov, A. V. Kalameitsev, V. M. Kovalev, H.-J. Kutschera, and A. Wixforth. Self-Induced Acoustic Transparency in Semiconductor Quantum Films. *Physical Review Letters* **87** (2001), 226803.

[21] R. Hanson, L. P. Kouwenhoven, J. R. Petta, S. Tarucha, and L. M. K. Vandersypen. Spins in few-electron quantum dots. *Reviews of Modern Physics* **79** (2007), 1217–1265.

[22] T.-K. Hsiao, A. Rubino, Y. Chung, S.-K. Son, H. Hou, J. Pedrós, A. Nasir, G. Éthier-Majcher, M. J. Stanley, R. T. Phillips, T. A. Mitchell, J. P. Griffiths, I. Farrer, D. A. Ritchie, and C. J. B. Ford. Single-photon emission from single-electron transport in a SAW-driven lateral light-emitting diode. *Nature Communications* **11**.1 (2020), 917.

[23] H. Sanada, Y. Kunihashi, H. Gotoh, K. Onomitsu, M. Kohda, J. Nitta, P. V. Santos, and T. Sogawa. Manipulation of mobile spin coherence using magnetic-field-free electron spin resonance. *Nature Physics* **9**.5 (2013), 280–283.

[24] S. Takada, H. Edlbauer, H. V. Lepage, J. Wang, P.-A. Mortemousque, G. Georgiou, C. H. W. Barnes, C. J. B. Ford, M. Yuan, P. V. Santos, X. Waintal, A. Ludwig, A. D. Wieck, M. Urdampilleta, T. Meunier, and C. Bäuerle. Sound-driven single-electron transfer in a circuit of coupled quantum rails. *Nature Communications* **10**.1 (2019), 4557.

[25] C. H. W. Barnes, J. M. Shilton, and A. M. Robinson. Quantum computation using electrons trapped by surface acoustic waves. *Physical Review B* **62** (2000), 8410–8419.

[26] M. J. A. Schuetz, J. Knörzer, G. Giedke, L. M. K. Vandersypen, M. D. Lukin, and J. I. Cirac. Acoustic Traps and Lattices for Electrons in Semiconductors. *Physical Review X* **7** (2017), 041019.

[27] B. Villa, A. J. Bennett, D. J. P. Ellis, J. P. Lee, J. Skiba-Szymanska, T. A. Mitchell, J. P. Griffiths, I. Farrer, D. A. Ritchie, C. J. B. Ford, and A. J. Shields. Surface acoustic wave modulation of a coherently driven quantum dot in a pillar microcavity. *Applied Physics Letters* **111**.1 (2017), 011103.

[28] M. Weiß and H. J. Krenner. Interfacing quantum emitters with propagating surface acoustic waves. *Journal of Physics D: Applied Physics* **51**.37 (2018), 373001.

[29] D. A. Golter, T. Oo, M. Amezcua, K. A. Stewart, and H. Wang. Optomechanical Quantum Control of a Nitrogen-Vacancy Center in Diamond. *Physical Review Letters* **116** (2016), 143602.

[30] S. J. Whiteley, G. Wolfowicz, C. P. Anderson, A. Bourassa, H. Ma, M. Ye, G. Koolstra, K. J. Satzinger, M. V. Holt, F. J. Heremans, A. N. Cleland, D. I. Schuster, G. Galli, and D. D. Awschalom. Spin-phonon interactions in silicon carbide addressed by Gaussian acoustics. *Nature Physics* **15**.5 (2019), 490–495.

[31] M. J. A. Schuetz, E. M. Kessler, G. Giedke, L. M. K. Vandersypen, M. D. Lukin, and J. I. Cirac. Universal quantum transducers based on surface acoustic waves. *Physical Review X* **5**.3 (2015), 031031.

[32] A. D. O'Connell, M. Hofheinz, M. Ansmann, R. C. Bialczak, M. Lenander, E. Lucero, M. Neeley, D. Sank, H. Wang, M. Weides, J. Wenner, J. M. Martinis, and A. N. Cleland. Quantum ground state and single-phonon control of a mechanical resonator. *Nature* **464**.7289 (2010), 697–703.

[33] Y. Chu, P. Kharel, W. H. Renninger, L. D. Burkhart, L. Frunzio, P. T. Rakich, and R. J. Schoelkopf. Quantum acoustics with superconducting qubits. *Science* **358**.6360 (2017), 199–202.

[34] Y. Chu, P. Kharel, T. Yoon, L. Frunzio, P. T. Rakich, and R. J. Schoelkopf. Creation and control of multi-phonon Fock states in a bulk acoustic-wave resonator. *Nature* **563**.7733 (2018), 666–670.

[35] P. Arrangoiz-Arriola, E. A. Wollack, Z. Wang, M. Pechal, W. Jiang, T. P. McKenna, J. D. Witmer, R. Van Laer, and A. H. Safavi-Naeini. Resolving the energy levels of a nanomechanical oscillator. *Nature* **571**.7766 (2019), 537–540.

[36] C. T. Hann, C.-l. Zou, Y. Zhang, Y. Chu, R. J. Schoelkopf, S. M. Girvin, and L. Jiang. Hardware-Efficient Quantum Random Access Memory with Hybrid Quantum Acoustic Systems. *Physical Review Letters* **123**.25 (2019), 250501.

[37] M. Aspelmeyer, T. J. Kippenberg, and F. Marquardt. Cavity optomechanics. *Reviews of Modern Physics* **86** (2014), 1391–1452.

[38] K. C. Balram, M. Davanco, J. D. Song, and K. Srinivasan. Coherent coupling between radio frequency, optical, and acoustic waves in piezo-optomechanical circuits. *Nature Photonics* **10**.5 (2016), 346–352.

[39] M. Forsch, R. Stockill, A. Wallucks, I. Marinković, C. Gärtner, R. A. Norte, F. van Otten, A. Fiore, K. Srinivasan, and S. Gröblacher. Microwave-to-optics conversion using a mechanical oscillator in its quantum ground state. *Nature Physics* **16**.1 (2020), 69–74.

[40] M. V. Gustafsson, P. V. Santos, G. Johansson, and P. Delsing. Local probing of propagating acoustic waves in a gigahertz echo chamber. *Nature Physics* **8**.4 (2012), 338–343.

[41] M. V. Gustafsson, T. Aref, A. F. Kockum, M. K. Ekström, G. Johansson, and P. Delsing. Propagating phonons coupled to an artificial atom. *Science* **346**.6206 (2014), 207–211.

[42] D. Roy, C. M. Wilson, and O. Firstenberg. Colloquium: Strongly interacting photons in one-dimensional continuum. *Reviews of Modern Physics* **89** (2017), 021001.

[43] X. Gu, A. Kockum, A. Miranowicz, Y. Liu, and F. Nori. Microwave photonics with superconducting quantum circuits. *Physics Reports* **718** (2017), 1–102.

[44] R. Manenti, M. J. Peterer, A. Nersisyan, E. B. Magnusson, A. Patterson, and P. J. Leek. Surface acoustic wave resonators in the quantum regime. *Physical Review B* **93** (2016), 041411.

[45] R. Manenti, A. F. Kockum, A. Patterson, T. Behrle, J. Rahamim, G. Tancredi, F. Nori, and P. J. Leek. Circuit quantum acoustodynamics with surface acoustic waves. *Nature Communications* **8** (2017), 975.

[46] A. Noguchi, R. Yamazaki, Y. Tabuchi, and Y. Nakamura. Qubit-Assisted Transduction for a Detection of Surface Acoustic Waves near the Quantum Limit. *Physical Review Letters* **119** (2017), 180505.

[47] B. A. Moores, L. R. Sletten, J. J. Viennot, and K. W. Lehnert. Cavity Quantum Acoustic Device in the Multimode Strong Coupling Regime. *Physical Review Letters* **120** (2018), 227701.

[48] A. Noguchi, R. Yamazaki, Y. Tabuchi, and Y. Nakamura. Single-photon quantum regime of artificial radiation pressure on a surface acoustic wave resonator. *Nature Communications* **11**.1 (2020), 1183.

[49] K. J. Satzinger, Y. P. Zhong, H. .-.-S. Chang, G. A. Peairs, A. Bienfait, M.-H. Chou, A. Y. Cleland, C. R. Conner, E. Dumur, J. Grebel, I. Gutierrez, B. H. November, R. G. Povey, S. J. Whiteley, D. D. Awschalom, D. I. Schuster, and A. N. Cleland. Quantum control of surface acoustic wave phonons. *Nature* **563** (2018), 661–665.

[50] H. Kamerlingh Onnes. *Leiden Communications* 120b, 112b, 124c (1911).

[51] L. N. Cooper. Bound Electron Pairs in a Degenerate Fermi Gas. *Physical Review* **104** (1956), 1189–1190.

[52] M. Tinkham. *Introduction to Superconductivity*. 2nd edition. Mineola, New York: Dover Publications, 2004.

[53] R. Gross and A. Marx. *Festkörperphysik*. Berlin, Boston: De Gruyter, 2012.

[54] B. Josephson. Possible new effects in superconductive tunnelling. *Physics Letters* **1**.7 (1962), 251–253.

[55] R. Gross and A. Marx. *Applied Superconductivity: Josephson Effect and Superconducting Electronics*. 2005.

[56] G. J. Dolan. Offset masks for lift-off photoprocessing. *Applied Physics Letters* **31**.5 (1977), 337–339.

[57] A. Potts, G. J. Parker, J. J. Baumberg, and P. A. J. de Groot. CMOS compatible fabrication methods for submicron Josephson junction qubits. *IEE Proceedings - Science, Measurement and Technology* **148**.5 (2001), 225–228.

[58] G. Ventura and L. Risegari. Dilution Refrigerators. *The Art of Cryogenics*. Edited by G. Ventura and L. Risegari. Oxford: Elsevier, 2008, 143–161.

[59] C. Macklin, K. O'Brien, D. Hover, M. E. Schwartz, V. Bolkhovsky, X. Zhang, W. D. Oliver, and I. Siddiqi. A near–quantum-limited Josephson traveling-wave parametric amplifier. *Science* **350**.6258 (2015), 307–310.

[60] J. Koch, T. M. Yu, J. M. Gambetta, A. A. Houck, D. I. Schuster, J. Majer, A. Blais, M. H. Devoret, S. M. Girvin, and R. J. Schoelkopf. Charge-insensitive qubit design derived from the Cooper pair box. *Physical Review A* **76**.4 (2007), 042319.

[61] J. Clarke and F. K. Wilhelm. Superconducting quantum bits. *Nature* **453**.7198 (2008), 1031–1042.

[62] A. Blais, A. L. Grimsmo, S. M. Girvin, and A. Wallraff. *Circuit Quantum Electrodynamics.* arXiv 2005.12667. 2020.

[63] J. J. Sakurai and J. Napolitano. *Modern Quantum Mechanics.* 2nd edition. Cambridge University Press, 2017.

[64] T. Aref, P. Delsing, M. K. Ekström, A. F. Kockum, M. V. Gustafsson, G. Johansson, P. J. Leek, E. Magnusson, and R. Manenti. Quantum Acoustics with Surface Acoustic Waves. *Superconducting Devices in Quantum Optics.* Edited by R. H. Hadfield and G. Johansson. Cham: Springer International Publishing, 2016, 217–244.

[65] D. Pozar. *Microwave Engineering, 4th Edition.* Wiley, 2011.

[66] M. Gustafsson. *Studies of acoustic waves, noise and charge pumping using single-electron devices.* PhD thesis. Chalmers University of Technology, 2012.

[67] B. Peropadre, J. Lindkvist, I.-C. Hoi, C. M. Wilson, J. J. Garcia-Ripoll, P. Delsing, and G. Johansson. Scattering of coherent states on a single artificial atom. *New Journal of Physics* **15**.3 (2013), 035009.

[68] J. Sakurai. *Advanced Quantum Mechanics.* Pearson Education, Incorporated, 1967.

[69] A. F. Kockum, P. Delsing, and G. Johansson. Designing frequency-dependent relaxation rates and Lamb shifts for a giant artificial atom. *Physical Review A* **90**.1 (2014), 013837.

[70] J. Garrison and R. Chiao. *Quantum Optics.* Oxford University Press, 2014.

[71] R. Loudon. *The Quantum Theory of Light.* Oxford University Press, 2000.

[72] A. F. Kockum. *Quantum optics with giant atoms – the first five years.* arXiv:1912.13012. 2019.

[73] A. F. Kockum, G. Johansson, and F. Nori. Decoherence-Free Interaction between Giant Atoms in Waveguide Quantum Electrodynamics. *Physical Review Letters* **120**.14 (2018), 140404.

[74] B. Kannan, M. J. Ruckriegel, D. L. Campbell, A. Frisk Kockum, J. Braumüller, D. K. Kim, M. Kjaergaard, P. Krantz, A. Melville, B. M. Niedzielski, A. Vepsäläinen, R. Winik, J. L. Yoder, F. Nori, T. P. Orlando, S. Gustavsson, and W. D. Oliver. Waveguide quantum electrodynamics with superconducting artificial giant atoms. *Nature* **583**.7818 (2020), 775–779.

[75] G. Lindblad. On the generators of quantum dynamical semigroups. *Communications in Mathematical Physics* **48**.2 (1976), 119–130.

[76] M. Fleischhauer and J. P. Marangos. Electromagnetically induced transparency: Optics in coherent media. *Reviews of Modern Physics* **77**.2 (2005), 633–673.

[77] J. P. Marangos. Topical review Electromagnetically induced transparency. *Journal of Modern Physics* **45**.3 (1998), 471–503.

[78] L. V. Hau, S. E. Harris, Z. Dutton, and C. H. Behroozi. Light speed reduction to 17 meters per second in ultracold atomic gases. *Nature* **397**.February (1999), 594–598.

[79] S. Weis, R. Riviere, S. Deleglise, E. Gavartin, O. Arcizet, A. Schliesser, and T. J. Kippenberg. Optomechanically Induced Transparency som. *Science* **330**.6010 (2010), 1520–1523.

[80] P. M. Anisimov, J. P. Dowling, and B. C. Sanders. Objectively Discerning Autler-Townes Splitting from Electromagnetically Induced Transparency. *Physical Review Letters* **107**.16 (2011), 163604.

[81] S. H. Autler and C. H. Townes. Stark Effect in Rapidly Varying Fields. *Physical Review* **100** (1955), 703–722.

[82] O. Astafiev, A. M. Zagoskin, A. A. Abdumalikov, Y. A. Pashkin, T. Yamamoto, K. Inomata, Y. Nakamura, and J. S. Tsai. Resonance fluorescence of a single artificial atom. *Science* **327**.5967 (2010), 840–843.

[83] C. W. Gardiner and M. J. Collett. Input and output in damped quantum systems: Quantum stochastic differential equations and the master equation. *Physical Review A* **31** (1985), 3761–3774.

[84] S. Novikov, T. Sweeney, J. E. Robinson, S. P. Premaratne, B. Suri, F. C. Wellstood, and B. S. Palmer. Raman coherence in a circuit quantum electrodynamics lambda system. *Nature Physics* **12**.1 (2015), 75–79.

[85] I.-C. Hoi, C. M. Wilson, G. Johansson, T. Palomaki, B. Peropadre, and P. Delsing. Demonstration of a Single-Photon Router in the Microwave Regime. *Physical Review Letters* **107**.7 (2011), 073601.

[86] A. L. Grimsmo. Time-Delayed Quantum Feedback Control. *Physical review letters* **115**.6 (2015), 060402.

[87] H. Pichler and P. Zoller. Photonic Circuits with Time Delays and Quantum Feedback. *Physical Review Letters* **116**.9 (2016), 093601.

[88] H. Pichler, S. Choi, P. Zoller, and M. D. Lukin. Universal photonic quantum computation via time-delayed feedback. *Proceedings of the National Academy of Sciences* **114**.43 (2017), 11362–11367.

[89] M. Nielsen and I. Chuang. *Quantum Computation and Quantum Information*. Cambridge University Press, 2000.

[90] C. A. Fuchs and J. V. D. Graaf. Cryptographic Distinguishability Measures. *IEEE Transactions on Information Theory* **45**.4 (1999), 1216–1227.

[91] H.-P. Breuer, E.-M. Laine, J. Piilo, and B. Vacchini. Colloquium: Non-Markovian dynamics in open quantum systems. *Reviews of Modern Physics* **88** (2016), 021002.

[92] C.-F. Li, G.-C. Guo, and J. Piilo. Non-Markovian quantum dynamics: What does it mean? *EPL (Europhysics Letters)* **127**.5 (2019), 50001.

[93] H.-P. Breuer, E.-M. Laine, and J. Piilo. Measure for the degree of non-Markovian behavior of quantum processes in open systems. *Physical Review Letters* **103** (2009), 210401.

[94] L. Guo, A. L. Grimsmo, A. F. Kockum, M. Pletyukhov, and G. Johansson. Giant acoustic atom: A single quantum system with a deterministic time delay. *Physical Review A* **95**.5 (2017), 053821.

[95] B.-H. Liu, L. Li, Y.-F. Huang, C.-F. Li, G.-C. Guo, E.-M. Laine, H.-P. Breuer, and J. Piilo. Experimental control of the transition from Markovian to non-Markovian dynamics of open quantum systems. *Nature Physics* **7**.12 (2011), 931–934.

[96] N. Wiener. Generalized harmonic analysis. *Acta Mathematica* **55** (1930), 117–258.

[97] A. Blais, R.-S. Huang, A. Wallraff, S. M. Girvin, and R. J. Schoelkopf. Cavity quantum electrodynamics for superconducting electrical circuits: An architecture for quantum computation. *Physical Review A* **69** (2004), 062320.

[98]   D. I. Schuster, A. Wallraff, A. Blais, L. Frunzio, R. S. Huang, J. Majer, S. M. Girvin, and R. J. Schoelkopf. Ac Stark shift and dephasing of a superconducting qubit strongly coupled to a cavity field. *Physical Review Letters* **94**.12 (2005), 1–4.

[99]   J. Gambetta, A. Blais, D. I. Schuster, A. Wallraff, L. Frunzio, J. Majer, M. H. Devoret, S. M. Girvin, and R. J. Schoelkopf. Qubit-photon interactions in a cavity: Measurement-induced dephasing and number splitting. *Physical Review A* **74** (2006), 042318.

[100] M. Boissonneault, J. M. Gambetta, and A. Blais. Dispersive regime of circuit QED: Photon-dependent qubit dephasing and relaxation rates. *Physical Review A* **79** (2009), 013819.

[101] P. Krantz, M. Kjaergaard, F. Yan, T. P. Orlando, S. Gustavsson, and W. D. Oliver. A quantum engineer's guide to superconducting qubits. *Applied Physics Reviews* **6**.2 (2019), 021318.

[102] J. J. Burnett, A. Bengtsson, M. Scigliuzzo, D. Niepce, M. Kudra, P. Delsing, and J. Bylander. Decoherence benchmarking of superconducting qubits. *npj Quantum Information* **5**.54 (2019).

[103] J. M. Martinis, K. B. Cooper, R. McDermott, M. Steffen, M. Ansmann, K. D. Osborn, K. Cicak, S. Oh, D. P. Pappas, R. W. Simmonds, and C. C. Yu. Decoherence in Josephson qubits from dielectric Loss. *Physical Review Letters* **95**.21 (2005), 210503.

[104] J. Gao, M. Daal, A. Vayonakis, S. Kumar, J. Zmuidzinas, B. Sadoulet, B. A. Mazin, P. K. Day, and H. G. Leduc. Experimental evidence for a surface distribution of two-level systems in superconducting lithographed microwave resonators. *Applied Physics Letters* **92**.152505 (2008).

[105] M. Scigliuzzo, L. E. Bruhat, A. Bengtsson, J. J. Burnett, A. F. Roudsari, and P. Delsing. Phononic loss in superconducting resonators on piezoelectric substrates. *New Journal of Physics* **22**.5 (2020), 053027.

[106] L. Guo, A. F. Kockum, F. Marquardt, and G. Johansson. *Oscillating bound states for a giant atom*. arXiv:1911.13028. 2019.

[107] C. Müller, J. H. Cole, and J. Lisenfeld. Towards understanding two-level-systems in amorphous solids - insights from quantum circuits. *Reports on Progress in Physics* (2019).

[108] J. Jäckle. On the ultrasonic attenuation in glasses at low temperatures. *Zeitschrift für Physik* **257**.3 (1972), 212–223.

[109] S. Hunklinger and W. Arnold. Ultrasonic Properties of Glasses at Low Temperatures. Edited by W. P. Mason and R. Thurston. Volume 12. Academic Press, 1976, 155–215.

[110] S. Datta and B. J. Hunsinger. First-order reflection coefficient of surface acoustic waves from thin-strip overlays. *Journal of Applied Physics* **50**.9 (1979), 5661–5665.

[111] R. Manenti. *Circuit quantum acoustodynamics with surface acoustic waves*. PhD thesis. University of Oxford, 2017.

[112] A. J. Slobodnik. GaAs acoustic-surface-wave propagation losses at 1 GHz. *Electronics Letters* **8**.12 (1972), 307–309.

[113] J. Devkota, P. R. Ohodnicki, and D. W. Greve. SAW Sensors for Chemical Vapors and Gases. *Sensors* **17**.4 (2017).

[114] W. A. Phillips. Tunneling states in amorphous solids. *Journal of Low Temperature Physics* **7**.3 (1972), 351–360.

[115] W. A. Phillips. Two-level states in glasses. *Reports on Progress in Physics* **50**.12 (1987), 1657–1708.

[116] G. J. Grabovskij, T. Peichl, J. Lisenfeld, G. Weiss, and A. V. Ustinov. Strain tuning of individual atomic tunneling systems detected by a superconducting qubit. *Science* **338**.6104 (2012), 232–234.

[117] J. Lisenfeld, G. J. Grabovskij, C. Müller, J. H. Cole, G. Weiss, and A. V. Ustinov. Observation of directly interacting coherent two-level systems in an amorphous material. *Nature Communications* **6** (2015).

[118] J. Gao. *The Physics of Superconducting Microwave Resonators*. PhD thesis. California Institute of Technology, 2008.

[119] L. Faoro and L. B. Ioffe. Internal loss of superconducting resonators induced by interacting two-level systems. *Physical Review Letters* **109**.15 (2012), 157005.

[120] J. M. Sage, V. Bolkhovsky, W. D. Oliver, B. Turek, and P. B. Welander. Study of loss in superconducting coplanar waveguide resonators. *Journal of Applied Physics* **109**.6 (2011), 063915.

[121] R. Jankowiak, J. M. Hayes, and G. J. Small. Spectral Hole-Burning Spectroscopy in Amorphous Molecular Solids and Proteins. *Chemical Reviews* **93**.4 (1993), 1471–1502.

[122] N. R. S. Reddy and G. J. Small. Spectral Hole Burning: Methods and Applications to Photosynthesis. *Biophysical Techniques in Photosynthesis* (2006), 123–136.

[123] N. Kirsh, E. Svetitsky, A. L. Burin, M. Schechter, and N. Katz. Revealing the nonlinear response of a tunneling two-level system ensemble using coupled modes. *Physical Review Materials* **1**.1 (2017), 012601.

[124] T. Capelle, E. Flurin, E. Ivanov, J. Palomo, M. Rosticher, S. Chua, T. Briant, P.-F. Cohadon, A. Heidmann, T. Jacqmin, and S. Deléglise. Probing a Two-Level System Bath via the Frequency Shift of an Off-Resonantly Driven Cavity. *Physical Review Applied* **13** (2020), 034022.

[125] S. Probst, F. B. Song, P. A. Bushev, A. V. Ustinov, and M. Weides. Efficient and robust analysis of complex scattering data under noise in microwave resonators. *Review of Scientific Instruments* **86**.2 (2015), 024706.

[126] J. Burnett, L. Faoro, I. Wisby, V. L. Gurtovoi, A. V. Chernykh, G. M. Mikhailov, V. A. Tulin, R. Shaikhaidarov, V. Antonov, P. J. Meeson, A. Y. Tzalenchuk, and T. Lindström. Evidence for interacting two-level systems from the 1/f noise of a superconducting resonator. *Nature Communications* **5**.May (2014).

[127] S. E. De Graaf, A. A. Adamyan, T. Lindström, D. Erts, S. E. Kubatkin, A. Y. Tzalenchuk, and A. V. Danilov. Direct Identification of Dilute Surface Spins on Al2 O3: Origin of Flux Noise in Quantum Circuits. *Physical Review Letters* **118**.5 (2017), 057703.

[128] N. Tubsrinuan. *Probing two-level systems with a surface acoustic wave resonator*. Master's thesis. Chalmers University of Technology, 2020.

[129] C. Weedbrook, S. Pirandola, R. García-Patrón, T. C. Ralph, J. H. Shapiro, and S. Lloyd. Gaussian Quantum Information. *Reviews of Modern Physics* **84**.621 (2012), 621–669.

[130] J. Preskill. Quantum Computing in the NISQ era and beyond. *Quantum* **2** (2018), 79.

[131] A. G. Fowler, M. Mariantoni, J. M. Martinis, and A. N. Cleland. Surface codes: Towards practical large-scale quantum computation. *Physical Review A* **86** (2012), 032324.

[132] E. T. Campbell, B. M. Terhal, and C. Vuillot. Roads towards fault-tolerant universal quantum computation. *Nature* **549**.7671 (2017), 172–179.

[133] R. Raussendorf and H. J. Briegel. A One-Way Quantum Computer. *Physical Review Letters* **86** (2001), 5188–5191.

[134] H. J. Briegel and R. Raussendorf. Persistent Entanglement in Arrays of Interacting Particles. *Physical Review Letters* **86** (2001), 910–913.

[135] N. C. Menicucci, P. Van Loock, M. Gu, C. Weedbrook, T. C. Ralph, and M. A. Nielsen. Universal quantum computation with continuous-variable cluster states. *Physical Review Letters* **97**.11 (2006), 13–16.

[136] S. T. Flammia, N. C. Menicucci, and O. Pfister. The optical frequency comb as a one-way quantum computer. *Journal of Physics B: Atomic, Molecular and Optical Physics* **42**.11 (2009), 114009.

[137] O. Pfister. Continuous-variable quantum computing in the quantum optical frequency comb. *Journal of Physics B: Atomic, Molecular and Optical Physics* **53**.1 (2020), 012001.

[138] J. Yoshikawa, S. Yokoyama, T. Kaji, C. Sornphiphatphong, Y. Shiozawa, K. Makino, and A. Furusawa. Invited Article: Generation of one-million-mode continuous-variable cluster state by unlimited time-domain multiplexing. *APL Photonics* **1**.6 (2016), 060801.

[139] M. V. Larsen, X. Guo, C. R. Breum, J. S. Neergaard-Nielsen, and U. L. Andersen. Deterministic generation of a two-dimensional cluster state. *Science* **366**.6463 (2019), 369–372.

[140] K. G. Fedorov, L. Zhong, S. Pogorzalek, P. Eder, M. Fischer, J. Goetz, E. Xie, F. Wulschner, K. Inomata, T. Yamamoto, Y. Nakamura, R. Di Candia, U. Las Heras, M. Sanz, E. Solano, E. P. Menzel, F. Deppe, A. Marx, and R. Gross. Displacement of Propagating Squeezed Microwave States. *Physical Review Letters* **117** (2016), 020502.

[141] S. Pogorzalek, K. G. Fedorov, M. Xu, A. Parra-Rodriguez, M. Sanz, M. Fischer, E. Xie, K. Inomata, Y. Nakamura, E. Solano, A. Marx, F. Deppe, and R. Gross. Secure quantum remote state preparation of squeezed microwave states. *Nature Communications* **10**.1 (2019), 2604.

[142] C. M. Caves. Quantum-mechanical noise in an interferometer. *Physical Review D* **23** (1981), 1693–1708.

[143] J. Aasi et al. Enhanced sensitivity of the LIGO gravitational wave detector by using squeezed states of light. *Nature Photonics* **7**.8 (2013), 613–619.

[144] C. Eichler, D. Bozyigit, C. Lang, M. Baur, L. Steffen, J. M. Fink, S. Filipp, and A. Wallraff. Observation of two-mode squeezing in the microwave frequency domain. *Physical Review Letters* **107**.11 (2011), 113601.

[145] P. Drummond and Z. Ficek. *Quantum Squeezing*. Springer, 2013.

[146] R. Medeiros De Araújo, J. Roslund, Y. Cai, G. Ferrini, C. Fabre, and N. Treps. Full characterization of a highly multimode entangled state embedded in an optical frequency comb using pulse shaping. *Physical Review A - Atomic, Molecular, and Optical Physics* **89**.5 (2014), 053828.

[147] W. Asavanant, Y. Shiozawa, S. Yokoyama, B. Charoensombutamon, H. Emura, R. N. Alexander, S. Takeda, J. ichi Yoshikawa, N. C. Menicucci, H. Yonezawa, and A. Furusawa. Generation of time-domain-multiplexed two-dimensional cluster state. *Science* **366**.6463 (2019), 373–376.

[148] D. C. McKay, S. Filipp, A. Mezzacapo, E. Magesan, J. M. Chow, and J. M. Gambetta. Universal Gate for Fixed-Frequency Qubits via a Tunable Bus. *Physical Review Applied* **6** (2016), 064007.

[149] L. Yuan, Q. Lin, M. Xiao, and S. Fan. Synthetic dimension in photonics. *Optica* **5**.11 (2018), 1396.

[150] N. R. A. Lee, M. Pechal, E. A. Wollack, P. Arrangoiz-Arriola, Z. Wang, and A. H. Safavi-Naeni. Propagation of microwave photons along a synthetic dimension. *Physical Review A* **101** (2020), 053807.

[151] *Intermodulation Products AB*. https://intermodulation-products.com/. 2020.

[152] A. Mari and J. Eisert. Positive Wigner Functions Render Classical Simulation of Quantum Computation Efficient. *Physical Review Letters* **109**.December (2012), 230503.

[153] Y. S. Ra, A. Dufour, M. Walschaers, C. Jacquard, T. Michel, C. Fabre, and N. Treps. Non-Gaussian quantum states of a multimode light field. *Nature Physics* **16**.2 (2019), 144–147.

[154] M. Hofheinz, H. Wang, M. Ansmann, R. C. Bialczak, E. Lucero, M. Neeley, A. D. O'Connell, D. Sank, J. Wenner, J. M. Martinis, and A. N. Cleland. Synthesizing arbitrary quantum states in a superconducting resonator. *Nature* **459**.7246 (2009), 546–549.

[155] B. Vlastakis, G. Kirchmair, Z. Leghtas, S. E. Nigg, L. Frunzio, S. M. Girvin, M. Mirrahimi, M. H. Devoret, and R. J. Schoelkopf. Deterministically Encoding Quantum Information Using 100-Photon Schrodinger Cat States. *Science* **342**.6158 (2013), 607–610.

Appended papers